ABSTRACT

Title of Dissertation: RATE-INDEPENDENT LINEAR DAMPING IN VIBRATION CONTROL ENGINEERING

Ashkan Keivan Esfahani, Doctor of Philosophy, 2018

Dissertation directed by: Associate Professor, Brian M. Phillips, Department of Civil and Environmental Engineering

The focus of this dissertation is on incorporating rate-independent linear damping (RILD) in low-frequency dynamic systems such as base-isolated structures, inter-story isolated buildings, and vehicle suspension systems. RILD is a promising damping model for low-frequency structures because it provides direct control over displacement. Because the control force generated by RILD is proportional to displacement (advanced in phase by $\pi/2$ radians) and independent of frequency, it performs well under both low-frequency and high-frequency excitations (relative to the structure's fundamental natural frequency). The $\pi/2$ radians phase advance makes RILD non-causal, which has hindered its practical applications. This dissertation proposes causal semi-active controllers and passive mechanical systems to approximate RILD in different areas of vibration control engineering. Numerical simulations, shake table tests, and real-time hybrid simulation (RTHS) tests are

conducted to demonstrate the performance of the proposed causal approaches. The results compare well to non-causal simulations in both the achieved forces and system responses. Through the proposed algorithms and devices, RILD is shown to be an attractive and practical damping alternative for the vibration mitigation of low-frequency structures.

RATE-INDEPENDENT LINEAR DAMPING IN VIBRATION CONTROL ENGINEERING

by

Ashkan Keivan Esfahani

Dissertation submitted to the Faculty of the Graduate School of the
University of Maryland, College Park, in partial fulfillment
of the requirements for the degree of
Doctor of Philosophy
2018

Advisory Committee:
Prof. Brian M. Phillips, Chair
Prof. Amde M. Amde
Prof. Balakumar Balachandran
Prof. Mary L. Bowden
Prof. Chung C. Fu

Dedication

It is my genuine gratefulness and warmest regard that I dedicate this work to my always encouraging, ever faithful parents, and to my supportive, kind-hearted brothers.

Acknowledgements

I would like to express my gratitude to my advisor, Professor Brian M. Phillips for his patience, guidance and encouragement during the course of this study. I learned a lot from him over the past four years and it was my privilege to work under his supervision. Professor Phillips granted me a chance to work on numerous interesting research projects with our brilliant research collaborators in Japan which has been a remarkable, unforgettable international experience for me. My PhD program at University of Maryland at College Park has been as perfect as it can possibly get, and I owe all of that to my supportive, insightful advisor for which I am deeply grateful.

I would also like to sincerely appreciate support and contribution of Professor Kohju Ikago of Tohoku University which inspired this work in rate-independent linear damping. I am very much thankful for the support of both Professor Ikago and Professor Masahiro Ikenaga on the large-scale shake table testing at Tohoku University in Japan. It has been an honor for me to work with all of our research collaborators from Japan. I also gratefully acknowledge the support of Professor Yunfeng Zhang for the experimental studies at the University of Maryland Structural Engineering Laboratory.

I gratefully acknowledge the efforts of my dissertation committee, Professor Amde M. Amde, Professor Balakumar Balachandran, Professor Mary L. Bowden and Professor Chung C. Fu for their contribution in my research studies. All their support and comments are greatly appreciated.

This material is partially based upon a work supported by the National Science Foundation under Grant No. 1444160 and by the Japan Society for the Promotion of Science (JSPS) under Grant-in-Aid for Scientific Research (B) No. 15H04070. I would also like to acknowledge Osaka Prefecture and Dr. Toshihide Kashima of the Building Research Institute of Japan for providing the Sakishima site record of the 2011 Great East Japan Earthquake and Prof. Richard E. Christenson of the University of Connecticut for the use of the 200 kN MR damper.

Furthermore, I want to thank all my dear colleagues and friends in our research group at University of Maryland, Ruiyang Zhang, Jingzhe Wu, Sami Khan, Michael Whiteman, Katie Russell, and Pedro Fernandez. It has been a great experience for me to work with them and their friendship and ever-lasting support is deeply appreciated.

Last but not least, I appreciate all the support, love and encouragement from my parents and my brothers without whom I wouldn't be a person I am today. I am so honored and blessed to have them in my life. Special thanks to my parents for instilling me with a strong passion for learning and for doing everything possible to put me on the path to greatness. Words cannot describe how important you are to me. I love you all!

Table of Contents

List of Tables

List of Figures

List of Abbreviations

RILD: Rate-independent Linear Damping

RTHS: Real-time Hybrid Simulation

CFB: Causal Filter-based (Model)

MCFB: Modal Causal Filter-based (Model)

RMS: Root Mean Square

NSD: Negative Stiffness Device

MW: Maxwell (Element)

VFD: Variable Friction Damper

SDOF: Single Degree of Freedom

MDOF: Multi-Degree of Freedom

Chapter 1: Introduction and Motivation

The 2011 Great East Japan Earthquake produced devastating low-frequency ground motions that led to large displacements in low-frequency structures previously thought to be safe, including base-isolated structures. Base-isolated structures are particularly vulnerable because large displacements at the isolation layer can cause permanent damage to the isolators or the surrounding moat wall. Base isolation is often supplemented with viscous or hysteretic damping devices at the isolation layer (i.e., hybrid isolation, see Fig. 1.1) to reduce these displacements.

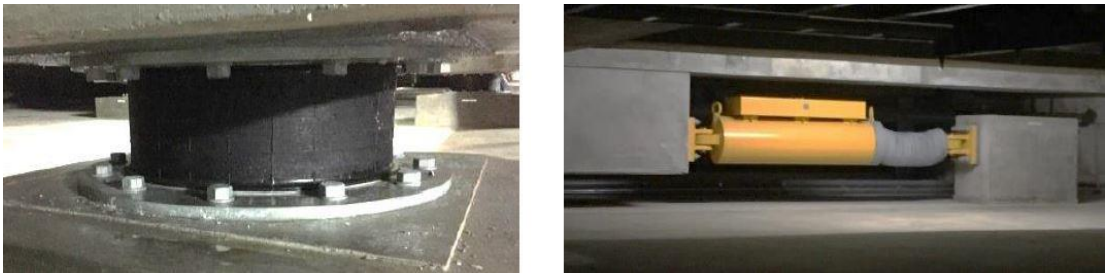

Fig. 1.1. *Hybrid base-isolation system on campus of Tohoku University.*

Traditional supplemental damping has some notable shortcomings when applied to protect low-frequency structures. Nonlinear hysteretic dampers such as steel yielding dampers work well for moderate displacements, however produce low equivalent damping ratios for small and large displacements. Viscous dampers can be tuned to provide the desired energy dissipation for a target frequency range. However, viscous dampers will then provide inadequate damping at lower frequencies and excessive damping (and accelerations) at higher frequencies. A robust hybrid isolation solution must provide seismic protection under a wide range of response

amplitudes and frequency content [1]. Fig. 1.2 provides a qualitative illustration of this behavior. Improvements to hybrid isolation systems for low-frequency ground motions must be tempered with the likelihood that higher-frequency ground motions (relative to the structure's fundamental natural frequency) can still occur.

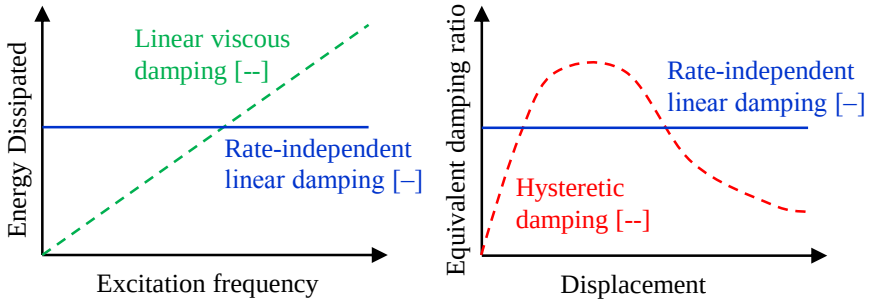

Fig. 1.2. *RILD versus other damping types.*

Rate-independent linear damping (RILD), also known as linear hysteretic damping, complex-value stiffness, structural damping, and solid damping [2-4] provides an attractive control alternative for low-frequency structures through direct control over displacement. Because the force is proportional to displacement (advanced in phase $\pi/2$ radians) and independent of frequency, RILD performs well under both low-frequency ground motions and more common higher frequency ground motions (see Fig. 1.2). If designed to provide a similar level of displacement reduction as other damping types, RILD can do so with a significantly lower restoring force and acceleration response. This benefit is most clearly seen when the excitation has frequency components higher than the fundamental natural frequency of the structure, typical of low-frequency structures under earthquake ground motions [1].

This research is motivated by a need for the displacement reduction of low frequency structures (fundamental natural frequency of approximately 0.1 to 1 Hz)

without compromising acceleration responses or requiring larger restoring forces. This research initially focuses on base-isolated structures. Additional applications are explored for inter-story isolated structures and vehicle suspension systems. Common to all applications, the systems are low-frequency relative to a majority of the expected range of excitation frequencies.

Ideal RILD is noncausal, limiting the practical applications to date. This dissertation investigates causal methods to mimic RILD for practical application. This dissertation proposes numerical approaches to approximate RILD which can later be tracked by semi-active or active control devices. Additionally, this dissertation investigates mechanisms to mimic RILD as a passive control system. This dissertation uses shake table and real-time hybrid simulation for experimental validation of the proposed control approaches.

Chapter 2: Literature Review

This chapter presents a literature review of relevant research across different areas of engineering. At first, the concept and benefits of RILD is discussed followed by brief review of vibration control systems. Then, existing problems in vibration control of various dynamic systems are reviewed, as they are primary motivations of this study. Finally, RILD is presented as a possible solution to improve the vibration performance of the dynamic systems.

2.1 Rate Independent Linear Damping

In RILD, the restoring force is proportional to the displacement advanced in phase by $\pi/2$ radians (90°), leading to its noncausality. Reid [4] first proposed a time-domain representation for causal rate-independent damping to solve the free vibration of a single degree-of-freedom (SDOF) system, though this model was later found to be nonlinear [5]. A linear visco-elastic model for RILD was presented by Biot [6]. This model consists of a linear spring in parallel with an infinite number of Maxwell elements (spring-dashpot links). Crandall [7] first noted that ideal RILD is noncausal. Crandall [8] further investigated the performance of different damping devices using transfer functions in the frequency domain and impulse response functions in the time domain, concluding that a damper with frequency independent energy dissipation violates causality requirements. Makris [9] proposed a causal hysteretic element that generates frequency independent energy dissipation. In this approach, an adjustable

term is added to ideal RILD to satisfy causality. The model was shown to be the limiting case of the linear visco-elastic model proposed by Biot [6]. Both the Biot and Makris models are considered in this study as a comparison to the proposed approach for a causal realization of RILD.

2.2 Vibration Control Systems

Vibration control can be classified in three major categories, passive, active, and semi-active. Passive control is practical and cost effective; however, the performance is fixed and tuned for a particular frequency range or amplitude. Passive systems have inherent limitations in achieving broad performance objectives. On the other hand, active systems can be programmed to perform well under a variety of scenarios, but they are more expensive, require a constant power source, and can potentially destabilize a system. As a result of the noted limitations of both type of systems, semi-active vibration isolation was introduced by Crosby and Karnopp [10, 11]. These systems have the adaptable control performance of active systems coupled with the ruggedness of passive systems.

To achieve semi-active control, various types of controllable dampers can be used. Among those, magnetorheological dampers (MR) are popular devices since the damping force generated by these dampers can be quickly changed with a change in magnetic field. Other examples include electro-rheological dampers (ER), variable orifice dampers, and controllable fluid dampers [12].

2.3 Base Isolation

Isolation, in particular base isolation, is a widely popular passive control strategy for seismic protection. Isolation systems introduce a layer of reduced horizontal stiffness into a structure, largely decoupling higher frequency motion above and below the isolation layer. Base-isolated structures in which the isolation layer is installed at the foundation have been designed and used extensively over the past two decades [13, 14]. Base isolation decreases the fundamental natural frequency of the structure, reducing the acceleration of the superstructure and concentrating most of the inter-story drift in the isolation layer.

The isolation layer may go through large displacements, especially for near-fault ground motions. To suppress these large displacements, the isolation layer is often equipped with passive, active, or semi-active supplemental damping, creating a hybrid isolation system. As discussed in Section 2.1, although common viscous dampers can suppress the deformation of the isolation bearings, they will result in increased responses in the superstructure due to the large damper forces at the isolation layer [15, 16]. Additionally, active systems are not generally accepted by engineers due to their uncertain performance under extreme loads. Semi-active devices, on the other hand, have received considerable attention by the researchers over the past decade to reduce isolation layer deformations without increasing super-structure responses. Nagarajaiah and Sahasrabudhe [17] proposed a semi-active variable stiffness device to be installed in an isolation layer and showed the effectiveness through numerical simulations and experimental tests. Yoshioka, et al. [18] demonstrated the performance of an MR damper in improving seismic

performance of base-isolated structures is shown by. Ozbulut, et al. [19] investigated the effectiveness of two adaptive control strategies to control variable friction dampers (VFDs) for the seismic protection of base-isolated buildings. Hybrid isolation systems remain a vibrant area of research for the protection of base-isolated structures. RILD is an attractive solution through its simple formulation and broad frequency range of favorable performance. The application of RILD to base-isolated structures is a fundamental focus in this dissertation.

2.4 Inter-story Isolation

Although base isolation remains one of the most popular seismic control strategies, many buildings are not suitable for this type of isolation because of foundation requirements, the height of the building, or the need for a seismic gap to prevent collisions of the isolated layer. In particular, it is difficult to install base isolation in the retrofit of existing buildings [20] When base isolation is not possible or practical, inter-story isolation is a viable design alternative. Ogura, et al. [21] discusses the benefits of incorporating inter-story isolation in the reduction of seismic responses of superstructure. Huang, et al. [22] discusses the benefits of inter-story isolation to both the superstructure (above isolation layer) and the substructure (below isolation layer).

Inter-story isolation appears in a number of practical engineering designs worldwide. In Japan, Murakami, et al. [23] describe the design procedure of the Iidabashi First Building (IFB) located in Tokyo, a multi-purpose 14-story building with an isolation layer between the 9^{th} and 10^{th} floor. In this building, offices are located on 2^{nd} to 9^{th} floor and apartments are located on 10^{th} to 14^{th} floor. Additionally, Sueoka, et al. [24] investigated a 25-story mid-story isolated building in

which the isolation layer was installed between the 11th floor and 12th floor. Other examples of mid story isolation can be found in the literature [25, 26]. Many simplified structural models have been proposed to analyze the seismic behavior of inter-story isolated systems [27-29].

Chey, et al. [30] introduced semi-active control algorithm for inter-story isolation systems to mitigate seismic damages and reduce earthquake responses. Yan and Chen [31] studied the effect of strong near-field pulse-like ground motion on inter-story isolated systems. Excessive deformation of the isolation layer due to these types of earthquakes may result in the overturning collapse of the superstructure. Therefore, they presented a protective system to reduce this excessive deformation of the isolation layer by soft pounding and the effectiveness of the protective system was validated. Another alternative to suppress the excessive deformation of the isolation layer is traditional viscous dampers, such as those used in the new Civil Engineering Research Building on the campus of National Taiwan University [32]. However, using viscous dampers in the isolation layer results in larger damping forces and higher acceleration responses of the superstructure. Therefore, additional study on supplemental structural control is needed to address this tradeoff. RILD can be an attractive solution to this problem.

2.5 Vehicle Suspension Systems

Semi-active controllers have been applied to vehicle suspension systems by a number of authors. Choi, et al. [33] used skyhook semi-active control law with an ER damper. The same controller was used by Yao, et al. [34] with an MR damper in the suspension. Different variations of skyhook controller are investigated in detail by

Ivers and Miller [35]. Shen, et al. [36] investigated three semi-active controllers including: the limited relative displacement method, the modified skyhook method, and the modified Rakheja-Sankar approach for use in suspension MR damper systems. Both numerical and experimental tests have been carried out and the performance of three different controllers were compared together. Khiavi, et al. [37] proposed a nonlinear tracking control law to track a desired skyhook damping force for a quarter car model with a MR damper.

Ahmadian and Pare [38] experimentally studied three semi-active controllers including: skyhook, groundhook, and hybrid control policy on a quarter car vehicle model with MR damper. In that study it was shown that increasing the skyhook damping results in better vibration performance of the sprung mass of the car at the expense of the unsprung mass responses. The reverse holds true for groundhook controller; increasing groundhook damping force results in reduction of unsprung mass responses (i.e., displacement or acceleration) and increase in sprung mass responses. Therefore, the authors proposed a hybrid control algorithm which is a linear combination of skyhook and groundhook controllers. It is concluded that hybrid algorithm if adapted can better improve vehicle stability as well as ride comfort and have combined effect of skyhook and groundhook controller. It is worth noting that all variations of skyhook, groundhook, or hybrid control policy require measurements of absolute velocity of the sprung or unsprung mass of the vehicle.

RILD is proposed for vehicle suspension to address the limitations of variations on skyhook and groundhook controllers. These limitations include clear tradeoffs in mitigating the vibration of one mass at the expense of the other and the

need for sensors that can measure (or estimate) absolute velocity. This dissertation will investigate the application of ideal and causal RILD for vehicle suspension systems. Approaches developed for base-isolated and inter-story isolated structures will first be considered, followed by improvements developed specific to vehicle systems.

Chapter 3: Background

In this chapter, single degree-of-freedom (SDOF) and multi-degree-of-freedom (MDOF) representations of RILD are explored in detail. Then numerical analysis procedure used in this dissertation is discussed. Further, Section 3.4 discusses the various experimental testing techniques used for this dissertation. Finally, the historic earthquake ground motions and input road profiles that are used throughout this dissertation are presented.

3.1 RILD SDOF Representation

Rate-independent linear damping will first be explored using a second-order SDOF system subject to a ground acceleration:

$$m\ddot{x}(t) + f_D(t) + kx(t) = -m\ddot{x}_g(t) \tag{3.1}$$

where t denotes time, m is the mass, k is the stiffness, $f_D$is the damping force, $\ddot{x}_g(t)$ is the input ground acceleration, $x(t)$ represents the displacement relative to the ground, and dots represent derivatives with respect to time.

In deriving RILD, it is useful to first examine viscous damping. Viscous damping has been successfully employed in many civil engineering structures in the form of traditional oil dampers. The restoring forces generated by these dampers are nominally proportional to the velocity of the response (i.e., Equation (3.2)), meaning that these dampers only indirectly control displacements. Viscous damping is effective in controlling displacement when the product of the maximum displacement

response and the natural frequency of the structure (i.e., pseudo-velocity) match well with the actual maximum velocity response. When the actual maximum velocity exceeds the pseudo-velocity, viscous damping will produce excessive damping forces and subsequently high accelerations in the structure [1]. The energy dissipated by viscous damping in one cycle of harmonic vibration for steady state response is equal to:

$$f_{D,vis}(t) = c\dot{x}(t) \tag{3.2}$$

$$E_{visc} = 2\pi\xi \frac{\omega}{\omega_n} k u_0^2 \tag{3.3}$$

where u_0 is the amplitude of motion, ξ is the viscous damping ratio equal to $c/(2m\omega_n)$, and ω_n is natural frequency of the system. The energy dissipated is proportional to the square of the amplitude of motion u_0 and proportional to angular frequency of excitation ω.

An expression for RILD is more challenging because it is noncausal. Inaudi and Kelly [39] note that in the time domain, RILD is often incorrectly expressed using the following:

$$f_D(t) = ki\eta x(t) \tag{3.4}$$

$$f_D(t) = \frac{k\eta}{\omega}\dot{x}(t) \tag{3.5}$$

where ω represents angular frequency and η is the ratio between loss and storage modulus (i.e., the loss factor). Both expressions are incorrect: Equation (3.4) because it implies that a complex-valued force results from a real-valued displacement and Equation (3.5) because the frequency ω is not defined in the case of a non-harmonic velocity.

Because RILD is both noncausal and linear, it is best derived in the frequency domain. If the damping in Equation (3.1) is assumed to be proportional to the stiffness divided by the absolute value of the response frequency, the damping force becomes rate-independent and proportional to the preceded displacement (i.e., the displacement with a $\pi/2$ radians phase lead). Equation (3.1) incorporating RILD can be expressed in the frequency domain as:

$$(-m\omega^2 + \eta k\, i\, sign(\omega) + k)X(\omega) = -m\ddot{X}_g(\omega) \tag{3.6}$$

And the frequency domain representation of RILD is:

$$F_{D,RILD}(\omega) = \eta k\, i\, sign(\omega)X(\omega) \tag{3.7}$$

The operation of Equation (3.7) (setting aside the scalar value ηk) is equivalent to the convolution of $-1/\pi t$ and $x(t)$ in the time domain, also known as the Hilbert transform:

$$i\, sign(\omega)X(\omega) = \Im[-1/\pi t]X(\omega) = \hat{X}(\omega) = \Im[\hat{x}(t)] \tag{3.8}$$

where $\Im$ represents Fourier transform and $\hat{x}(t)$ is Hilbert transform of $x(t)$. Thus, in the time domain, Equation (3.7) can be written as:

$$f_{D,RILD}(t) = k\eta\hat{x}(t) \tag{3.9}$$

where Hilbert transform can also be expressed using the Cauchy principal value *p.v.* as represented in Equation (3.10).

$$\hat{x}(t) = \frac{1}{\pi} p.v. \int_{-\infty}^{\infty} \frac{x(t)}{t-\tau} d\tau \tag{3.10}$$

Equation (3.9) provides insight into the behavior of RILD and its relationship with the Hilbert transform, however, it is clear that a causal method is needed to approximate the ideal damping force for practical implementation.

The energy dissipated by RILD (i.e., Equation (3.11)) in one cycle of harmonic vibration for steady state response is equal to:

$$E_{RILD} = \pi \eta k u_0^2 \tag{3.11}$$

It is clear that the energy dissipated is independent of forcing frequency ω. Fig. 1.2 illustrates the energy dissipated versus forcing frequency for both RILD and viscous damping.

3.2 RILD MDOF Representation

The numerical analysis of RILD will now be extended to MDOF systems. Consider a MDOF system with the following equation of motion:

$$\mathbf{M}\ddot{\mathbf{x}} + \mathbf{C}\dot{\mathbf{x}} + \mathbf{K}\mathbf{x} + \mathbf{E}\hat{\mathbf{x}} = -\mathbf{M}\boldsymbol{\Gamma}\ddot{x}_g \tag{3.12}$$

where **M**, **C**, and **K** are mass, viscous damping, and stiffness matrix and **E** is linear rate-independent damping matrix of a MDOF system. $\ddot{x}_g$ is an input ground motion excitation and $\boldsymbol{\Gamma}$ distributes the input excitation to the correct masses. For this study, **E** can be calculated as follows:

$$\mathbf{E} = \begin{bmatrix} 0 & \cdots & 0 & 0 & \cdots & 0 \\ \vdots & \ddots & \vdots & \vdots & & \vdots \\ 0 & \cdots & \eta_i k_i & -\eta_i k_i & \cdots & 0 \\ 0 & \cdots & -\eta_i k_i & \eta_i k_i & \cdots & 0 \\ \vdots & & \vdots & \vdots & \ddots & \vdots \\ 0 & \cdots & 0 & 0 & \cdots & 0 \end{bmatrix}_{N \times N} \tag{3.13}$$

where η_i is the loss ratio and k_i is the stiffness of the i^{th} floor. Equation (3.13) gives the RILD coefficient matrix for an *N DOF* structure with a discrete RILD device installed at an isolation layer between $(i\text{-}1)^{th}$ and i^{th} story. Taking the Laplace transform of both sides of the Equation (3.12) results in:

$$\mathbf{M}s^2\mathbf{X}(s) + \mathbf{C}s\mathbf{X}(s) + \mathbf{K}\mathbf{X}(s) \pm i\mathbf{E}\mathbf{X}(s) = -\mathbf{M}\boldsymbol{\Gamma}\ddot{X}_g(s) \tag{3.14}$$

where the "+" sign is for positive frequencies and "−" sign is used for negative frequencies. Rewriting Equation (3.14) in state space form leads to following equations in frequency domain:

$$\begin{Bmatrix} s\mathbf{X}(s) \\ s^2\mathbf{X}(s) \end{Bmatrix} = \begin{bmatrix} \mathbf{0}_{N\times N} & \mathbf{I}_{N\times N} \\ \mathbf{M}^{-1}(\mathbf{K} \pm i\mathbf{E}) & -\mathbf{M}^{-1}\mathbf{C} \end{bmatrix}_{2N\times 2N} \begin{Bmatrix} \mathbf{X}(s) \\ s\mathbf{X}(s) \end{Bmatrix} + \begin{bmatrix} \mathbf{0}_{N\times 1} \\ \boldsymbol{\Gamma} \end{bmatrix}_{2N\times 1} \ddot{\mathbf{X}}_{\mathbf{g}}(s) \tag{3.15}$$

$$\begin{Bmatrix} \mathbf{X}(s) \\ s\mathbf{X}(s) \\ s^2\mathbf{X}(s) \end{Bmatrix} = \begin{bmatrix} \mathbf{I}_{N\times N} & \mathbf{0}_{N\times N} \\ \mathbf{0}_{N\times N} & \mathbf{I}_{N\times N} \\ \mathbf{M}^{-1}(\mathbf{K} \pm i\mathbf{E}) & -\mathbf{M}^{-1}\mathbf{C} \end{bmatrix}_{3N\times 2N} \begin{Bmatrix} \mathbf{X}(s) \\ s\mathbf{X}(s) \end{Bmatrix} + \begin{bmatrix} \mathbf{0}_{N\times 1} \\ \mathbf{0}_{N\times 1} \\ \mathbf{0}_{N\times 1} \end{bmatrix}_{3N\times 1} \ddot{\mathbf{X}}_{\mathbf{g}}(s) \tag{3.16}$$

In this form, the output $\mathbf{Y}(s)$ has *3N* outputs for the structure which includes relative displacement and velocity and absolute acceleration of all the floors. The response transfer function can be computed from state space matrices from Equations (3.15) and (3.16). Note that the frequency domain response must be calculated separately for positive and negative frequencies to accommodate the "±" sign of Equations (3.14) to (3.16). The responses must then be appended to create the response over the entire frequency range before taking the inverse Laplace transform. The time domain response displacement, velocity, and absolute acceleration can be calculated using the inverse Laplace transform as follows:

$$\mathbf{y}(t) = \begin{Bmatrix} \mathbf{x}(\mathrm{t}) \\ \dot{\mathbf{x}}(\mathrm{t}) \\ \ddot{\mathbf{x}}_{\mathbf{abs}}(\mathrm{t}) \end{Bmatrix} = \mathcal{L}^{-1}\left[\mathbf{H}(s) \quad \ddot{\mathbf{X}}_{\mathbf{g}}(s)\right]_{3N\times 1} \tag{3.17}$$

where $\mathcal{L}^{-1}$ represents the inverse Laplace transform, $\mathbf{H}(s)$ is the input-output transfer function created Equations (3.15) and (3.16), and $\mathbf{y}(t)$ is all the time domain output responses. This state space frequency domain method is used herein to provide the noncausal ideal RILD responses for comparison with proposed causal approaches.

3.3 Numerical Analysis of RILD

Two methods are commonly used for the analysis of RILD: non-causal time domain analysis and frequency domain analysis. Inaudi and Kelly [39] developed a time domain analysis procedure which iterates on a forcing function until convergence of the time domain solution is achieved. The forcing function is determined using the Hilbert transform through convolution in the time domain or through frequency domain techniques. Inaudi and Makris [40] proposed a time domain analysis procedure which splits the non-causal system into stable and unstable poles. The stable poles are integrated forward in time while the unstable poles are integrated backward in time. The solutions are combined to determine the total system response. Spanos and Tsavachidis [41] proposed two-time domain methods to solve the Biot model for RILD [6]; one recursive algorithm to solve the time-dependent integral in the equations of motion and one digital filter approach designed in the frequency domain. Muscolino, et al. [42] also focuses on the time domain solution of the Biot model, applying the Laguerre polynomial approximation method to turn the integro-differential equations of motion into a set of differential equations with parameters that can be determined from closed-form expressions. These time domain techniques

are well-suited for analyzing nonlinear systems, a shortcoming of frequency domain techniques.

For a linear system, frequency domain analysis is the most straightforward method to solve a noncausal system [43]. The following demonstrates the analysis of an SDOF system. Based on Equation (3.6), the displacement, velocity, absolute acceleration, and restoring force transfer functions can be computed as follows:

$$H_{d,RILD}(\omega) = \frac{-m}{-m\omega^2+\eta k\, i\, sign(\omega)+k} \tag{3.18}$$

$$H_{v,RILD}(\omega) = \frac{-mi\omega}{-m\omega^2+\eta k\, i\, sign(\omega)+k} \tag{3.19}$$

$$H_{a,RILD}(\omega) = \frac{m\omega^2}{-m\omega^2+\eta k\, i\, sign(\omega)+k} + 1 \tag{3.20}$$

$$H_{f,RILD}(\omega) = \eta k\, i\, sign(\omega) H_{d,RILD}(\omega) \tag{3.21}$$

The displacement, velocity, absolute acceleration, and restoring force response can be calculated in the time domain using the inverse Fourier transform as follows:

$$x(t) = \Im^{-1}[H_{d,RILD}(\omega)\ddot{X}_g(\omega)] \tag{3.22}$$

$$\dot{x}(t) = \Im^{-1}[H_{v,RILD}(\omega)\ddot{X}_g(\omega)] \tag{3.23}$$

$$\ddot{x}_{abs}(t) = \Im^{-1}[H_{a,RILD}(\omega)\ddot{X}_g(\omega)] \tag{3.24}$$

$$f_{D,RILD}(t) = \Im^{-1}[H_{f,RILD}(\omega)\ddot{X}_g(\omega)] \tag{3.25}$$

Note that the frequency domain response must be calculated separately for positive and negative frequencies to accommodate the *sign* function of Equations (3.18) through (3.24). The responses must then be appended to include the response over

the entire frequency range before taking the inverse Fourier transform. This method is applicable for MDOF structures if the m, k, and η scalars are replaced with corresponding matrices and the ground motion acceleration input is distributed to the appropriate masses.

3.4 Experimental Techniques

In this section various experimental testing techniques used in this dissertation are discussed as follows.

3.4.1 Shake table testing

Shake table testing is an attractive experimental testing technique for seismic studies. In shake table testing the entire structure is modeled and subjected to ground excitations applied by the shake table. Shake table testing captures the entire dynamic performance of the specimen due to a given earthquake.

Due to the cost, size limitations, and payload capacity of the shake table, reduced-scale structural models are often required for shake table testing. For accurate representation of the small-scaled specimen as compared to the target building, similitude laws should be followed. However, many local effects, such as fatigue, local buckling in steel, crack propagation, and welds, may affect the accuracy of the shake table testing. In this research study, shake table testing was used for all experimental tests conducted on the base-isolated specimen as presented in Chapter 6. The scaled building specimen is designed to remain linear, placing focus instead on the nonlinear supplemental control device.

3.4.2 Hybrid Simulation

Hybrid simulation is an alternative type of dynamic testing that combines numerical simulations with experimental testing. In hybrid simulation, the structural components for which the response is well-understood are modeled numerically, while the complex (usually nonlinear) members that are hard to simulate are experimentally tested which enormously reduces the required laboratory space and equipment. A loop of action and reaction connects experimental and numerical components using actuators and sensors. In this way, even small laboratories can conduct accurate experiments of complex structures. However, hybrid simulation cannot be used for experimental testing of rate-dependent components. This is due to the fact that all dynamics are modeled numerically and the experimental specimens are loaded on an extended time-scale (quasi-static).

3.4.3 Real-time Hybrid Simulation

Real-time hybrid simulation (RTHS) is an effective approach to validate the performance structural control devices. The complex (usually nonlinear) structural components that are hard to simulate numerically are physically built and evaluated. The remaining parts of the structural system that are easy to analyze are numerically modeled. In RTHS, the experiment is conducted in real time, enabling the evaluation of rate-dependent specimens such as damping devices [44-46].

Shake tables present an opportunity in the area of RTHS because the equipment is widely available and the creation of substructure boundary conditions is straightforward. The shake table base plate can serve as the interface between numerical and experimental substructures. This configuration is useful when the

lower portion of the structure is numerically modeled, facilitating studies on inter-story isolation. Additionally, if the experimental (upper) structure includes the isolation layer, the specimen will largely respond in the first mode, allowing simplified specimens to represent the dynamics of the superstructure (and isolation layer).

In both RTHS and shake table RTHS, there are time delays and time lags from the command to the response of the actuator or shake table. Additionally, control-structure interaction leads to a dynamic coupling between the actuator or shake table and the specimen. Time delays, time lags, and control-structure interaction must be compensated to ensure an accurate and stable test. Model-based control strategies are used for both RTHS and shake table RTHS in this dissertation [57]. The goal of these strategies are to cancel out the modeled dynamics of the actuator / shake table through feedforward control and provide robustness to changes in specimen dynamics, shake table nonlinearies, and uncertainties through feedback control.

In this dissertation, RTHS was used for the base-isolated structure and inter-story isolated structure in Chapter 9 and shake table RTHS was used for the inter-story isolated structure in Chapter 7.

3.4.4 Shake Table Real-time Hybrid Simulation and Dynamic Substructuring

In this dissertation, shake table RTHS was used to experimentally capture structural responses of inter-story isolated building as presented in Chapter 7 using dynamic substructuring. In dynamic substructuring, the experimental substructure is under-actuated, i.e., there is significant vibrating mass in the specimen. A dynamic substructuring approach based on Shing [47], is applied to this study. Fig. 3.1

illustrates the substructuring used for the inter-story isolated structure. In RTHS, the numerical substructure is excited by a ground acceleration and the numerical and interface DOF responses are determined through numerical integration. The absolute acceleration of the interface DOF is then used as the excitation to the shake table. Hence, a special class of shake table control strategies are required that can track accelerations determined online [48]. The base shear of the experimental substructure is then returned to the numerical substructure as the contribution from superstructure. This loop of action and reaction is carried out in real time until the entire time history response has been evaluated.

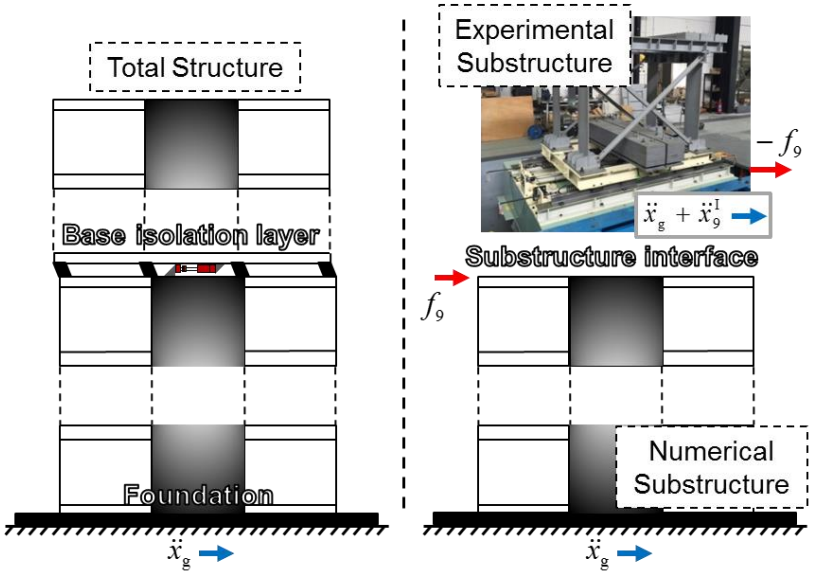

Fig. 3.1. *RTHS configuration using a shake table with dynamic substructuring.*

3.5 Historic Ground Motions

Six well-studied earthquake ground motion records with different magnitudes and frequency content are selected for analysis in this study: (1) Hachinohe: The N-S component recorded at Hachinohe Harbor during the Tokachi-oki earthquake of May 16, 1968; (2) Northridge: the N-S component of the Sylmar County Hospital parking

lot in Sylmar, California during the Northridge earthquake of January 17, 1994; (3) Kobe: the N-S component of the Japanese Meteorological Agency station during the Kobe earthquake of January 17, 1995; (4) Sakishima: the Sakishima site record of the 2011 Great East Japan Earthquake recorded in Sakishima, Osaka during the 2011 Tohoku earthquake, about 500 miles away from the epicenter; (5) $\text{Tohoku}_{\text{NS}}$: the N-S component of the Tsukidate - MYG004 record of the 2011 Great East Japan Earthquake, and (6) $\text{Tohoku}_{\text{EW}}$: the E-W component of the Tsukidate - MYG004 record of the 2011 Great East Japan Earthquake. The Hachinohe, Northridge, and Kobe records are documented in Ohtori, et al. [49] and the Sakishima record is credited in the acknowledgements, and the $\text{Tohoku}_{\text{NS}}$ and $\text{Tohoku}_{\text{EW}}$ records were accessed from the USGS Strong Motion Dataset (USGS, 2018).

Fig. 3.2 shows time history plots of the first four ground motions. It is worthwhile to mention that nature of a ground motion depends on several factors including source mechanism (e.g., epicenter and depth, rupture area and duration, magnitude, focal mechanism), travel path, local soil effects, and soil-structure interaction. For instance, the intensity of the earthquake nominally reduces with increases in distance from the epicenter. Additionally, as the distance increases, the duration of the ground motion is commonly extended while at the same time it will result in lower predominant frequency content. At the same time, soil acts like a dynamic oscillator that filters out high frequency components (in ground motion) and amplifies low frequency components. Softer, deeper, or weaker soil will have lower predominant frequency content. This fact also holds true for Sakishima record from 2011 Great East Japan Earthquake which was recorded hundreds of miles away from

the epic center and therefore is a long duration low frequency content ground motion as shown in Fig. 3.2. In structural engineering, the fundamental natural frequency of a structure can vary from 0.1 Hz (typical of long-span suspension bridges) to 10 Hz (typical of one-story fixed base buildings). The terms low and high frequency as used in this dissertation are relative to the fundamental natural frequency of the structure considered.

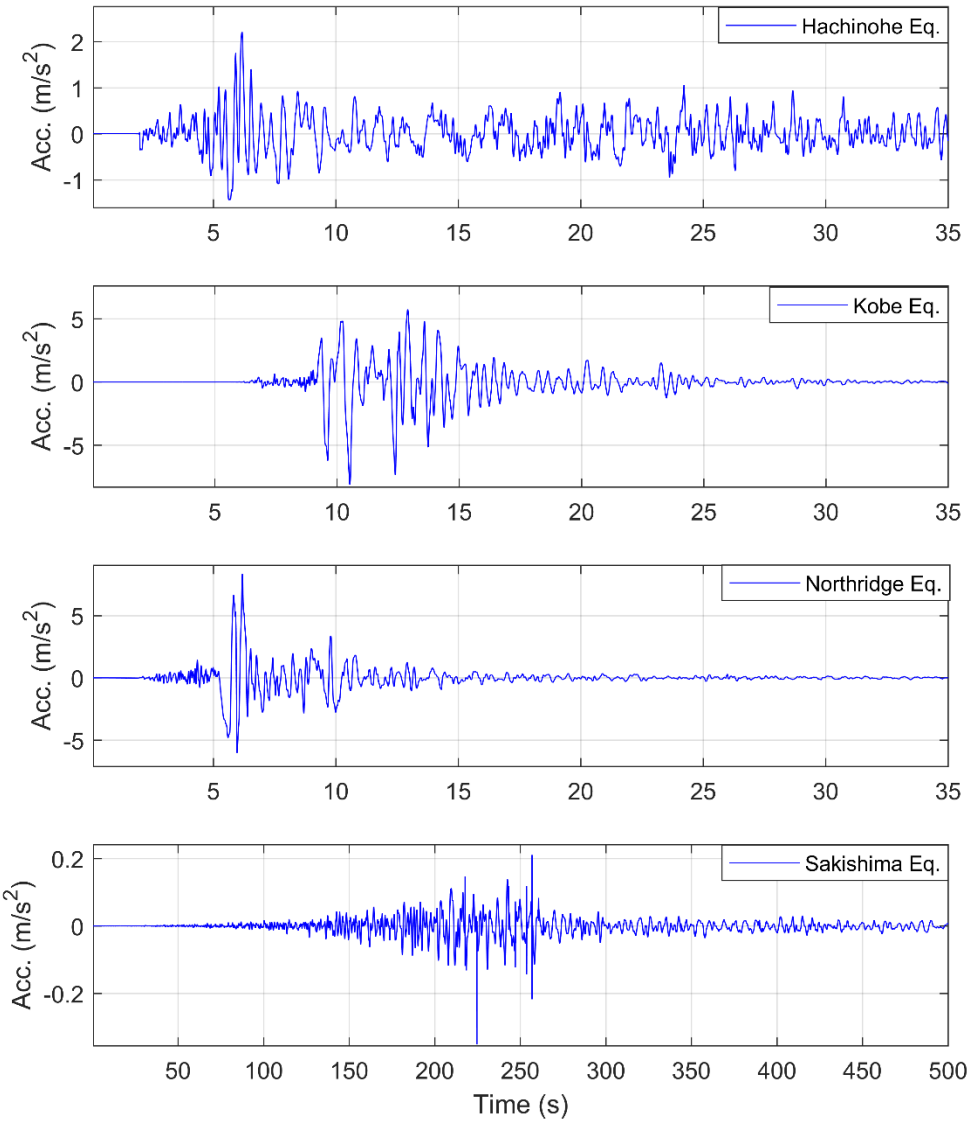

Fig. 3.2. *Time history plots of ground motions used in this study.*

3.6 Input Road Profile

For the application of vehicle suspension systems, two types of road profiles were considered. First type was a band-limited white noise signal with frequency content from 0 to 20 Hz. For this type of input road profile transmissibility plots as well as time history plots are provided. Transmissibility is defined as the ratio of response to the input displacement in frequency domain. Fig. 3.3 shows one sided power spectral density and the time history plot of the band-limited white noise road input with 226 seconds of data.

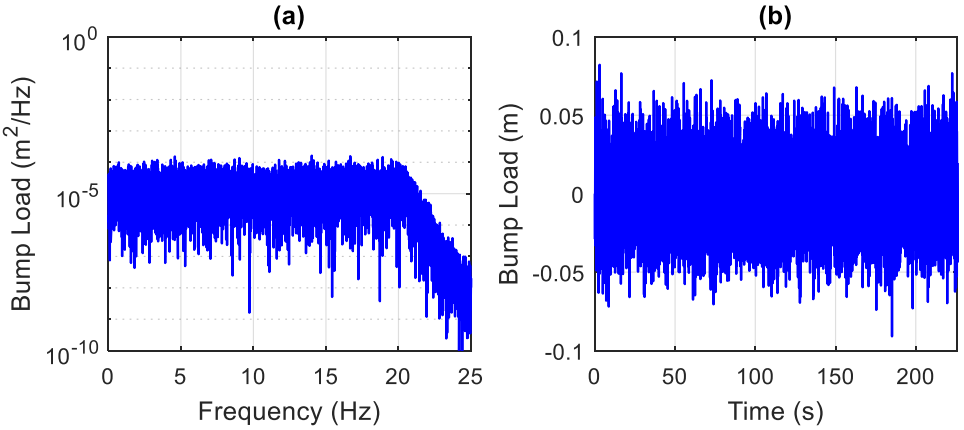

Fig. 3.3. *(a) One-sided power spectral density and (b) time history plot of the white noise road input.*

The second type of road input is a random road profile generated based on ISO 8608 [50] considering different damage levels or road qualities [51]. Based on ISO 8608 random road profile is calculated as a function of distance traveled by the vehicle. A travel distance of 250 meters is considered for this study. That function is then divided by the vehicle velocity to obtain a random function of time to be used in numerical simulations. Different velocities of 140, 120, 100, 80 and 50 *km/hr* are considered. Fig. 3.4 shows the random road profile generated for road quality of A-B

based on ISO 8608. For a fairer comparison across velocities, the same generated profile is used for all velocities.

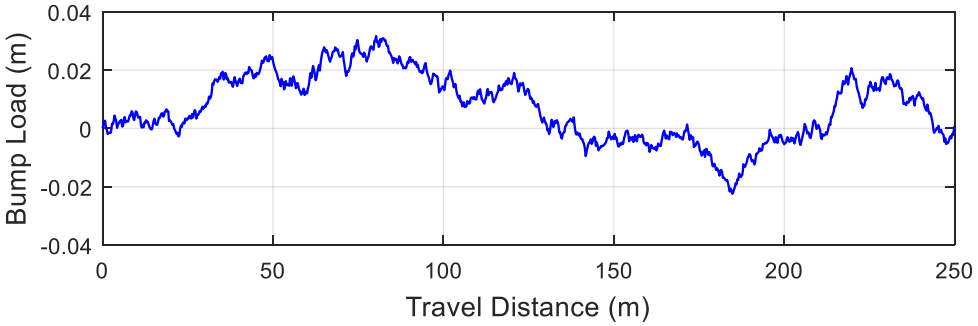

Fig. 3.4. *Random road profile for the road quality of A-B.*

Chapter 4: RILD Performance

In this Chapter, RILD is compared to other well-known damping devices. In Section 4.1 various damping models are compared together where they all have similar harmonic displacement input with no structures involved. Section 4.2 compares seismic performance of these damping devices implemented in a base-isolated structure. Finally, Section 4.3 illustrates both time and frequency domain comparison of RILD and viscous damping elements subjected to both low and high-frequency ground motions.

4.1 Comparison of Damping Types

Three supplemental damping types will be investigated herein, including viscous damping, Coulomb damping, and RILD. Alternatives will be explored using a second-order SDOF system subject to a ground acceleration:

$$m\ddot{x}(t) + f_d(t) + kx(t) = -m\ddot{x}_g(t) \tag{4.1}$$

where:

$$\text{Viscous:} \quad f_d(t) = c\dot{x}(t) \tag{4.2}$$

$$\text{Coulomb:} \quad f_d(t) = \mu N sign(\dot{x}) \tag{4.3}$$

$$\text{RILD:} \quad f_d(t) = \eta k\hat{x}(t) \tag{4.4}$$

As discussed earlier, generated force of viscous damping is proportional to the velocity of response and is most effective in displacement control when pseudo-

velocity matches well with the actual maximum velocity response. However, if the actual maximum velocity exceeds the pseudo-velocity, viscous damping will produce excessive damping forces and subsequently high accelerations in the structure [1].

Coulomb damping is commonly used to represent sliding friction. As with viscous damping, the restoring force is in phase with velocity. In traditional Coulomb damping the magnitude of the force is constant, equal to the product of the coefficient of friction μ and a constant contact normal force N. Due to a constant slip force, Coulomb damping only dissipates energy when the response is large enough to induce slippage between the surfaces.

Fig. 4.1 shows magnitude and phase of a transfer function with input displacement and output force for RILD and viscous damping. For reference, the transfer function of a stiffness element is also shown. Coulomb damping is nonlinear and will be studied in the time domain instead. The viscous damper has a damping coefficient of c = 3134 Ns/m, the RILD damping element has a value of ηk = 4910 N/m, and the spring has a stiffness k = 4910 N/m. As illustrated in Fig. 4.1, the spring and RILD elements have the same constant magnitude response, but a 90° difference in phase. On the other hand, RILD and the viscous element have identical phase response but a different magnitude response. The viscous damping coefficient was calibrated to have an identical magnitude response as RILD element at natural frequency of the structure (vertical dotted line).

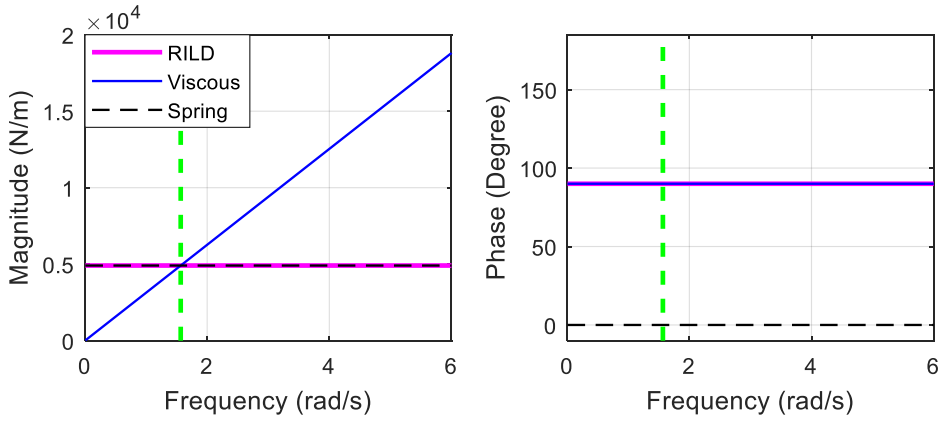

Fig. 4.1. *Magnitude and phase of force transfer function for RILD, viscous, and spring elements.*

To compare the three damping types of Equations (4.2) to (4.4) in the time domain, a set of harmonic excitations are input to the damping models. The damping parameters for RILD and viscous damping are consistent with those used to develop Fig. 4.1; Coulomb damping constant force was selected as μN = 981 N. These parameters achieve identical energy dissipation per cycle under a 0.25 m 0.25 Hz sine wave displacement input as shown in the hysteresis plots of Fig. 4.2. The hysteresis response under sine waves of increasing frequency and amplitude are also shown.

As illustrated in Fig. 4.2, as the frequency of the vibration increases, viscous damping generates significantly larger damping forces which if applied to a structure results in larger base shears and accelerations. On the other hand, Coulomb friction damping generates constant damping force regardless of input frequency and amplitude, leading to poor energy dissipation higher amplitude excitations. RILD is frequency independent and more effective than Coulomb friction in dissipating energy under varying amplitude inputs. For a harmonic signal of amplitude u_0 and circular frequency ω, the energy dissipated per cycle for viscous damping, and RILD

is given in Equations (3.3) and (3.10), respectively; and for Coulomb damping is presented as follows:

$$E_{D,Coul.} = 4\mu N u_0 \tag{4.5}$$

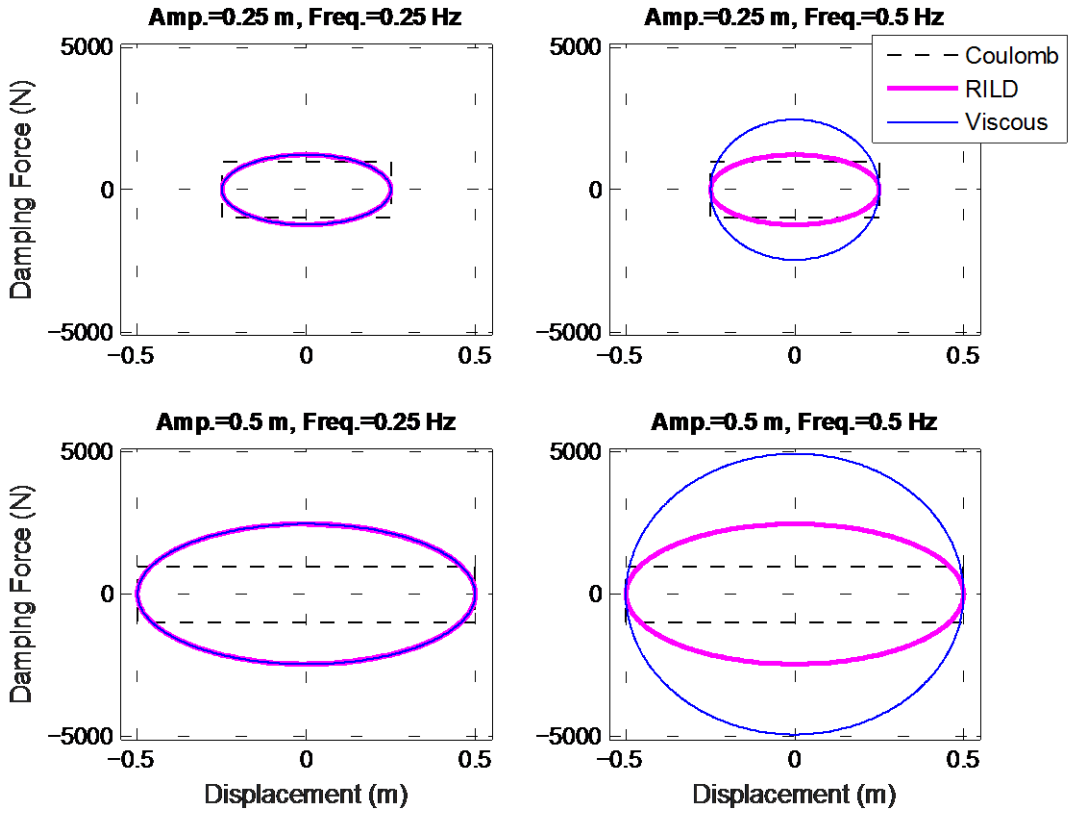

Fig. 4.2. *Steady state hysteresis plots of Coulomb friction, RILD and viscous damping elements.*

4.2 Comparison of Damping Types in an SDOF structure

In this section, the performance of different damping types will be investigated for an SDOF system. Coulomb damping will be replaced with a modulated Coulomb damping model. To improve upon traditional Coulomb damping, semi-active control algorithms have been introduced to vary N(t) with time. Inaudi [52] proposed a Modulated Homogeneous Friction (MHF) algorithm where the force is proportional

to the previous local peak of the displacement, updated after each velocity zero-crossing. The MHF system is rate-independent and works well for semi-active friction type dampers.

Fig. 4.3 compares three SDOF systems: one with viscous damping, one with MHF (semi-active Coulomb damping), and one with RILD. The natural frequency of all structures is chosen as 0.25 Hz (1.6 rad/s), typical of a base-isolated structure. The viscous damping coefficient c is chosen to achieve a 20% damping ratio, the MHF coefficient is adjusted to get a similar level of displacement performance, and the RILD loss factor is chosen as $\eta = 0.4$.

A time-domain analysis was performed on the three structures subject to the 1995 Kobe Earthquake, with results shown in Fig. 4.3. Displacements and velocities match well (this was the basis for parameter selection across models). Viscous damping generates significantly larger damping forces due to the high-frequency components of the earthquake excitation, resulting in larger base shears and accelerations. Both MHF and RILD show reduced acceleration and restoring forces compared to viscous damping. MHF works well for friction type dampers; however, the updates on the controllable damping are based on previous displacement peaks and the square-shaped hysteresis can make it impossible to reduce acceleration below a certain level. Additionally, because viscous damping and RILD are linear, the design can be predictably adjusted. If the design criteria were instead to limit the acceleration or force, RILD would be able to do so at a much lower displacement than viscous damping. For MHF, it was not possible to noticeably reduce the acceleration beyond the levels in Fig. 4.3, regardless of changes to the parameters. That is to say,

increasing MHF damping will increase the severity of the force jump, making it challenging to effectively mitigate acceleration responses.

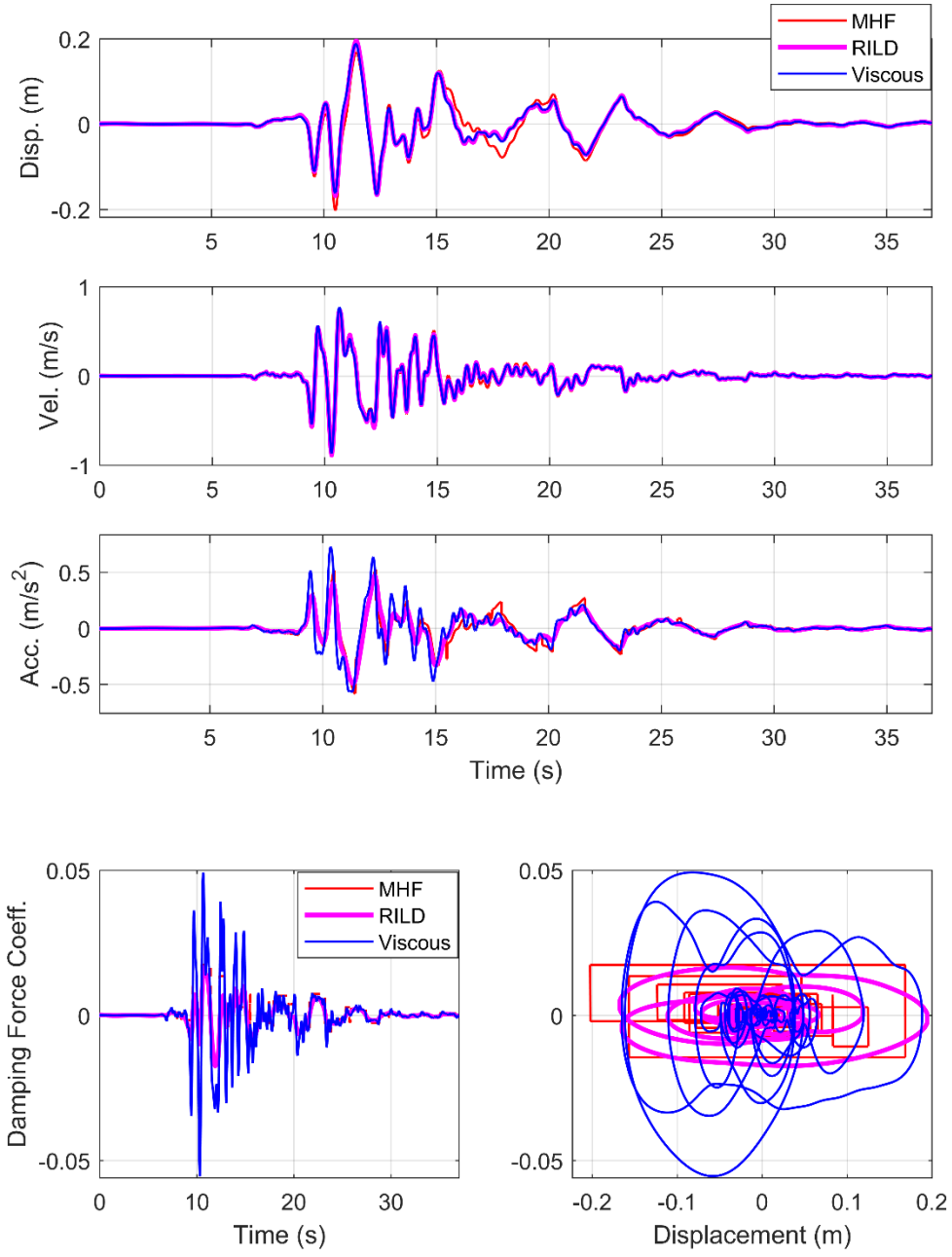

Fig. 4.3. *Time-domain response for three damping types with parameters scaled to achieve a similar maximum displacement.*

4.3 Detailed RILD and Viscous Comparison in an SDOF structure

This section illustrates effectiveness of RILD compared to viscous damping for low-frequency structures subjected to both low- and high-frequency ground motions relative to the fundamental natural frequency of the structure. Fig. 4.4 and Fig. 4.5 compare displacement, velocity, absolute acceleration, and the damping force coefficient transfer functions for two SDOF systems with a mass of 5 metric tons, natural frequency of 0.25 Hz, and subject to an input ground motion. The damping force coefficient is defined as the damping force divided by the weight of the SDOF system, resulting in a dimensionless parameter. The RILD system has a loss factor η of 0.4 and the viscous damping system has a critical damping ratio ξ of 0.2. These designs achieve identical displacement response at the structure's natural frequency. The vertical dashed line in Fig. 4.4 and Fig. 4.5 identifies the natural frequency of the SDOF system.

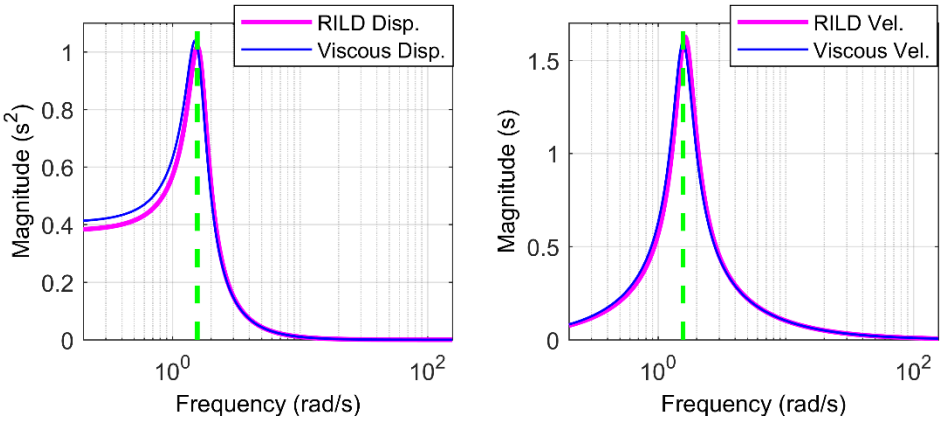

Fig. 4.4. *Displacement and velocity transfer function magnitude for RILD and viscous damping.*

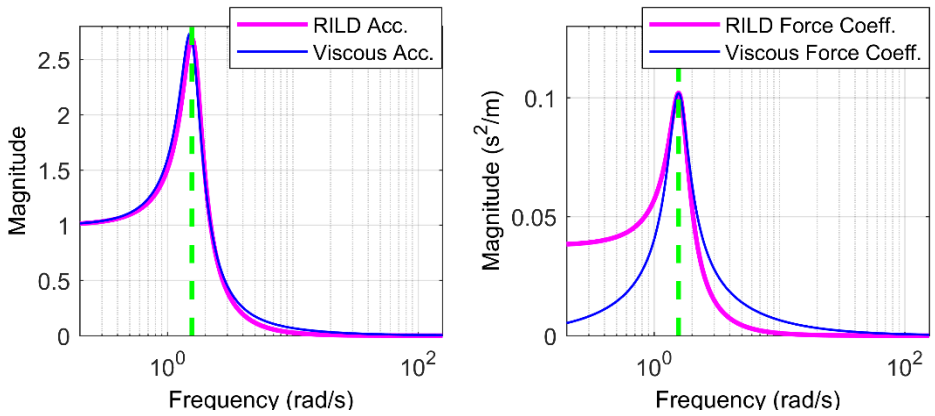

Fig. 4.5. *Absolute acceleration and damping force coefficient transfer function magnitude for RILD and viscous damping.*

As shown in Fig. 4.4 and Fig. 4.5, displacement and velocity transfer functions for both systems are almost identical for any frequency. This is the result of the selection of the loss factor and critical damping ratio of the respective systems to match maximum displacements in the time domain. However, for damping force transfer function in frequency range larger than the natural frequency of the structure, the viscous damping force is larger than RILD force. This is also true for absolute acceleration transfer function. To maintain a similar displacement reduction as RILD, viscous damping generates a higher damping force at frequencies larger than the structure's natural frequency, which may result in higher acceleration response of the system [1]. RILD can provide a similar level of displacement reduction using smaller forces.

To better illustrate this behavior, the same SDOF system was evaluated through numerical simulation subject to the JMA Kobe 1995 NS record. Fig. 4.6 and Fig. 4.7 show time history responses and hysteresis plot for both systems. As it is shown, both systems have almost identical displacement and velocity. However, viscous damping force is substantially higher than rate independent linear damping

force as expected. Hence, higher acceleration response is observed for the system with viscous damping. For this application, where a low-frequency structure is subjected to a ground motion dominated by high-frequency component, the effectiveness of RILD over viscous damping is clearly shown.

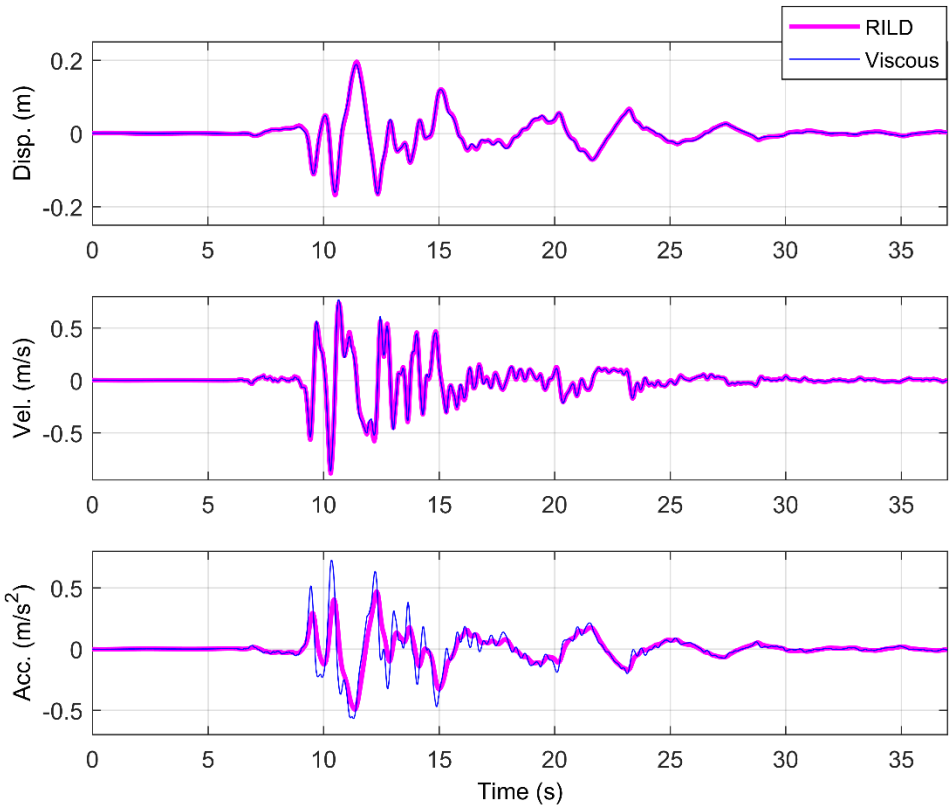

Fig. 4.6. *Time history responses for RILD and viscous damping for the JMA Kobe 1995 NS record.*

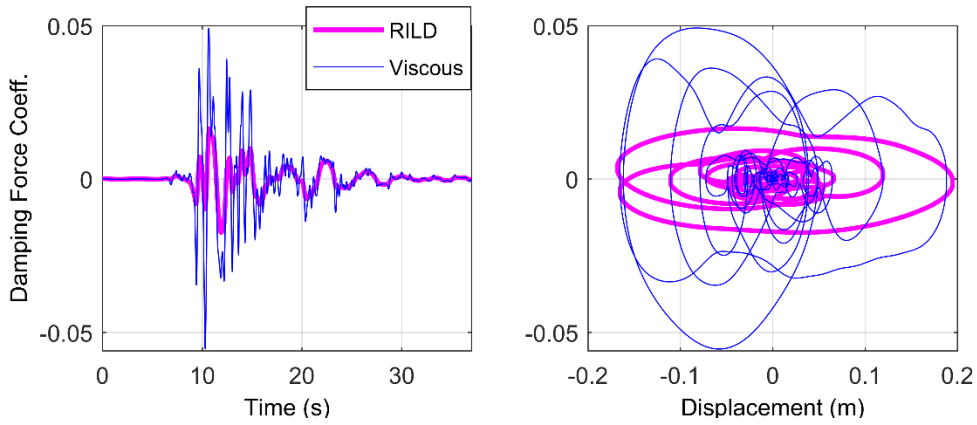

Fig. 4.7. *Damping force coefficient plots for RILD and viscous damping for the JMA Kobe 1995 NS record.*

To further investigate the performance of RILD over a broad range of ground motions, a predominantly low-frequency ground motion was applied to the same SDOF system. The ground motion was recorded in Sakishima, Osaka in Japan during the 2011 Tohoku earthquake, about 500 miles away from the epicenter. Fig. 4.8 shows pseudo velocity response spectrum of this record which has a peak of 41.8 cm/s at a period of 6.6 s (0.15 Hz). The spectrum shows the dominant low frequency content of the earthquake record. Fig. 4.9 and Fig. 4.10 show the time history responses and hysteresis plots for this earthquake, respectively.

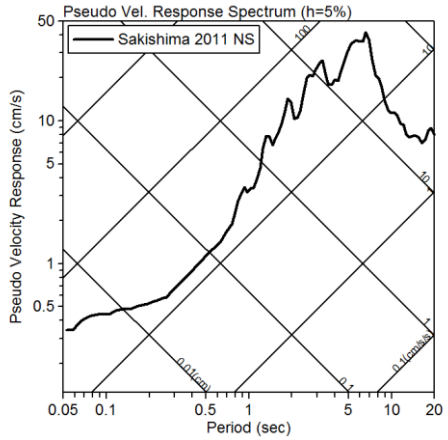

Fig. 4.8. *Pseudo-velocity response spectrum of Sakishima site record of 2011 Great East Japan Earthquake.*

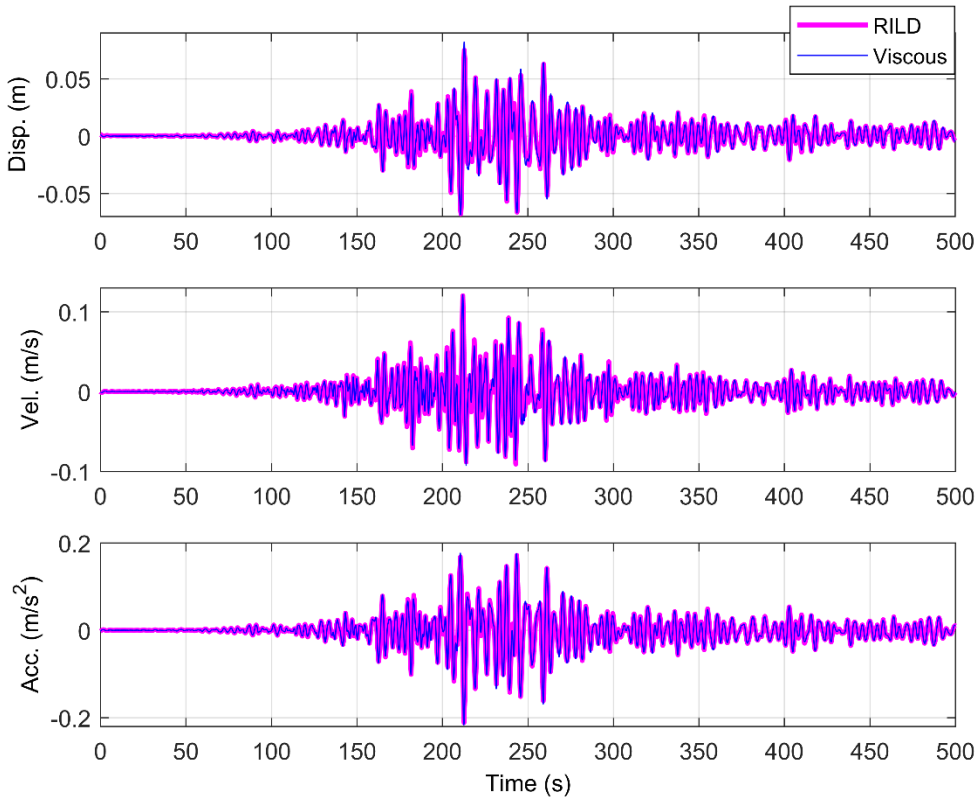

Fig. 4.9. *Time history responses for RILD and viscous damping for the Sakishima 2011 record.*

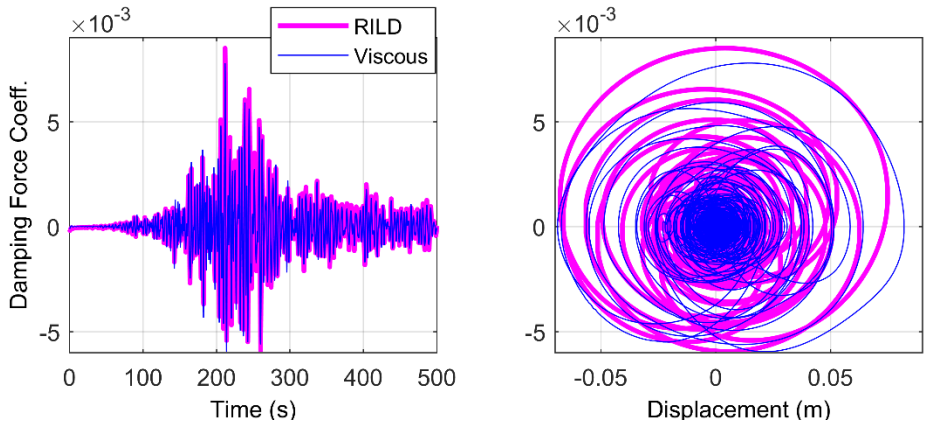

Fig. 4.10. *Damping force coefficient plots for RILD and viscous damping for the Sakishima 2011 record.*

As Fig. 4.9 and Fig. 4.10 show, for this case of low frequency earthquake

RILD has slightly larger peaks of damping force and slightly lower displacement

response. However, the difference is very small, consistent with Fig. 4.4 and Fig. 4.5 for frequencies below the natural frequency of the structure.

In summary, when RILD and viscous damping are designed to restrict displacement at the natural frequency of the structure, both damping types perform nearly identically for predominantly low-frequency earthquakes. For high-frequency earthquakes, RILD is superior in reducing acceleration and restoring force.

Chapter 5: Causal Approximation of RILD

This chapter focuses on causal numerical approximations of RILD. A simple filter-based approach is proposed to approximate the ideal RILD force in real time. This approach is compared to other available causal methods in both time and frequency domains.

5.1 Causal Approximations

The first successful model representing causal RILD was proposed by Biot [6]. This model is essentially a spring with the stiffness *k* in parallel with a large number of Maxwell elements (spring-dashpot links) with stiffness and viscous damping values of k_i and c_i. Assuming there are an infinite number of spring-dashpot links, the resulting damping force is calculated as:

$$r_{\mathrm{D,B}}(t) = kx + \frac{2k\eta}{\pi}\int_{\varepsilon}^{\infty}\frac{1}{(k_i/c_i)}\int_{t_0}^{t} e^{-(k_i/c_i)(t-\tau)}\,\frac{dx}{d\tau}\,d\tau dr \tag{5.1}$$

where ε is a small positive constant. Note that $r_{\mathrm{D}}(t)$ indicates the sum of stiffness force and modeled RILD force, while the previously presented $f_{\mathrm{D}}(t)$ only contains the RILD force. The Biot model restoring force is shown in the frequency domain in Equation (5.2), which includes the complex stiffness term shown in Equation (5.3). Equations (5.4) and (5.5) separate the complex stiffness term into the storage modulus and loss modulus, respectively.

$$R_{\mathrm{D,B}}(\omega) = K_{\mathrm{B}}(\omega) X(\omega) \tag{5.2}$$

$$K_{\mathrm{B}}(\omega) = k\left\{1 + \frac{2}{\pi}\eta \ln\sqrt{1+\left(\frac{\omega}{\varepsilon}\right)^2} + i\frac{2}{\pi}\eta a\tan\frac{\omega}{\varepsilon}\right\} \tag{5.3}$$

$$G_{\mathrm{s,B}}(\omega) = k\left\{1 + \frac{2}{\pi}\eta \ln\sqrt{1+\left(\frac{\omega}{\varepsilon}\right)^2}\right\} \tag{5.4}$$

$$G_{\mathrm{l,B}}(\omega) = \frac{2}{\pi} k\eta a\tan\frac{\omega}{\varepsilon} \tag{5.5}$$

For a system without viscous damping (only mass, stiffness, and Biot's representation of RILD) and with input earthquake ground motion, the displacement transfer function is computed from Equation (5.6). Velocity, absolute acceleration, and restoring force transfer functions can be derived from Equation (5.6).

$$H_{\mathrm{d,B}}(\omega) = \frac{-1}{\left\{-\omega^2 + \omega_n^2\left[1 + \frac{2}{\pi}\eta \ln\sqrt{1+\left(\frac{\omega}{\varepsilon}\right)^2} + i\frac{2}{\pi}\eta \operatorname{atan}\frac{\omega}{\varepsilon}\right]\right\}} \tag{5.6}$$

Makris [9] proposed a causal hysteretic element directly derived from the dynamic stiffness of the noncausal complex stiffness element (including both linear stiffness and RILD):

$$K_{\mathrm{RILD}}(\omega) = k[1 + i\eta sign(\omega)] \tag{5.7}$$

This noncausal complex stiffness is supplemented with the term $\frac{2}{\pi}\eta ln\left|\frac{\omega}{\varepsilon}\right|$ to satisfy causality. By adding this frequency-dependent real part to satisfy causality, the

imaginary part (loss-modulus) remains frequency independent. The causal stiffness element is given by:

$$K_{\mathrm{M}}(\omega) = k\left\{1 + \frac{2}{\pi}\eta \ln\left|\frac{\omega}{\varepsilon}\right| + i\eta sign\left(\frac{\omega}{\varepsilon}\right)\right\} \tag{5.8}$$

The arbitrary constant ε does not depend on the physics of the problem and can be set as small as desired so that the real part of $K(\omega)$ matches a realistic stiffness value measured at any finite frequency. Also, the term introduced in Equation (5.8) produces a singularity as $\omega \to 0$, therefore the model is not defined at the static limit. The storage and loss modulus are given by:

$$G_{\mathrm{s,M}}(\omega) = k\left\{1 + \frac{2}{\pi}\eta \ln\left|\frac{\omega}{\varepsilon}\right|\right\} \tag{5.9}$$

$$G_{\mathrm{l,M}}(\omega) = k\eta sign\left(\frac{\omega}{\varepsilon}\right) \tag{5.10}$$

For an input ground motion, the displacement transfer function can be computed as follows:

$$H_{\mathrm{d,M}}(\omega) = \frac{-1}{\left\{-\omega^2 + \omega_n^2\left[1 + \frac{2}{\pi}\eta \ln\left|\frac{\omega}{\varepsilon}\right| + i\eta sign(\omega)\right]\right\}} \tag{5.11}$$

Velocity, absolute acceleration, and restoring force transfer functions can be derived from Equation (5.11). The results of these two causal models will be compared to the proposed causal model.

5.2 Proposed Causal Model

Equation (3.7) correctly represents the RILD force in the frequency domain. The force can be broken into two components, the constant $k\eta$ and the transfer function:

$$H_{\mathrm{TF}}(\omega) = i\,sign(\omega) \tag{5.12}$$

Passing the response displacement for a particular device through the transfer function of Equation (5.12) and then multiplying by $k\eta$ will produce the ideal RILD force. Thus, Equation (5.12) is taken as the target filter for causal realization. The target filter has unity magnitude and phase advance of $\pi/2$ rad over all positive frequencies. The target filter is not implementable; however it can be approximated over a specified frequency range using a first-order all-pass filter [53]. Most structures will predominately respond at their fundamental natural frequency. Therefore, the all-pass filter should best match the target filter at the fundamental natural frequency of the structure. The all-pass filter will take the form:

$$H_{\mathrm{AP}}(\omega) = \frac{i\omega - \omega_n}{i\omega + \omega_n} \tag{5.13}$$

where ω_n is the fundamental natural frequency of the structure in rad/s. In general, ω_n can be replaced with the dominant frequency of vibration, as will be explored in Chapter 9.

Fig. 5.1 compares the magnitude and phase of the target filter with the first-order all-pass filter. At and around the fundamental natural frequency of the structure, the proposed filter design matches the phase of the target filter. At all frequencies, the proposed filter design matches the magnitude of the target filter.

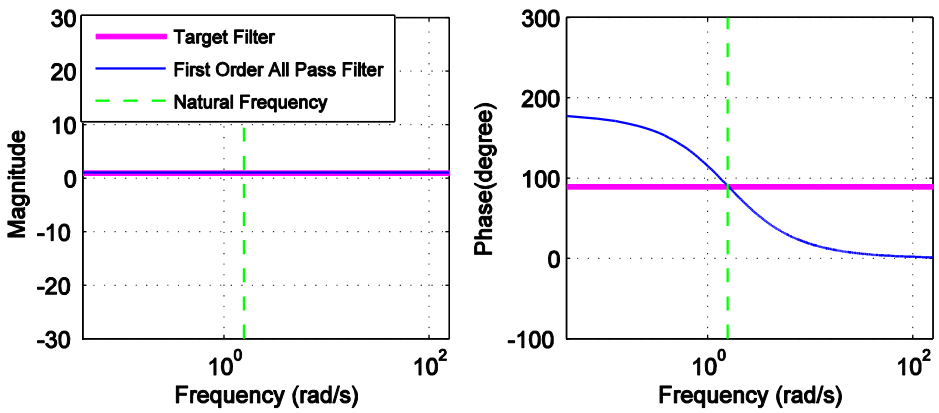

Fig. 5.1. *Magnitude and phase of target and all-pass filters.*

Passing a displacement through the target filter is equivalent to taking its Hilbert transform, a necessary step in the time domain realization of RILD. Since this filter cannot be implemented, an all-pass filter is proposed to accurately approximate the Hilbert transform at the natural frequency of the structure. Hence the filter creates $\pi/2$ phase lead at the natural frequency of the structure. This approach is applicable to SDOF systems as well as MDOF systems where the filter can be tuned to the first natural frequency of the structure. Base-isolated systems are heavily dominated by first mode response, making this approach particularly attractive.

The proposed filter is used to determine the preceded displacement in a causal manner. The preceded displacement is then multiplied by $k\eta$ to determine the corresponding RILD force. The only measurement needed to implement this method is the displacement of the device. For example, the displacement of the base-isolation layer can be used to determine the corresponding RILD force in a hybrid isolation system. The force can then be tracked by an active or semi-active control device. This simplicity is a great benefit for practical implementation. The RILD force is approximated by Equation (5.14) without the linear stiffness term or Equations (5.15)

and (5.16) with the linear stiffness term. The all-pass filter of Equation (5.13) can be solved in the time domain using standard discretization and numerical integration techniques.

$$F_{\mathrm{D,AP}}(\omega) = k\eta H_{\mathrm{AP}}(\omega) X(\omega) \tag{5.14}$$

$$R_{\mathrm{D,AP}}(\omega) = K_{\mathrm{AP}}(\omega) X(\omega) \tag{5.15}$$

$$K_{\mathrm{AP}}(\omega) = k(1 + \eta H_{\mathrm{AP}}(\omega)) \tag{5.16}$$

The displacement transfer function is shown in Equation (5.17). Velocity, absolute acceleration, and restoring force transfer function can be derived from Equation (5.14).

$$H_{\mathrm{d,AP}}(\omega) = \frac{-m}{\left\{-\omega^2 m + k + k\eta H_{\mathrm{AP}}(\omega)\right\}} \tag{5.17}$$

When the structure vibrates at its natural frequency, the force calculated from Equation (5.14) will match well with ideal RILD. At frequencies lower than the natural frequency, the restoring force hysteresis loop will have a negative skew. The increased phase lead produces negative stiffness which will reduce accelerations while increasing displacements. At frequencies higher than the natural frequency, the restoring force hysteresis loop will have a positive skew. Here, a decrease in phase lead produces positive stiffness which increases accelerations while decreasing displacement. However, as it is shown in this study, the proposed approach works well even for the slight drifts in response frequency away from the natural frequency of the structure. The Biot model and Makris model also have tunable parameters that

affects their performance across different frequencies, a feature that will be explored in the next section.

Fig. 5.2 shows preceded displacement calculated using the proposed all-pass filter compared to the actual Hilbert transform computed from a noncausal analysis. Errors in the approximation of the Hilbert transform as shown in Fig. 5.2 will manifest as slightly reduced effectiveness from of ideal RILD. The plot corresponds to an SDOF system with mass of 5 metric tons, natural frequency of 0.25 Hz, loss factor η of 0.6, and no viscous damping subjected to 50% Hachinohe 1968 NS record. Both analyses are performed in the frequency domain.

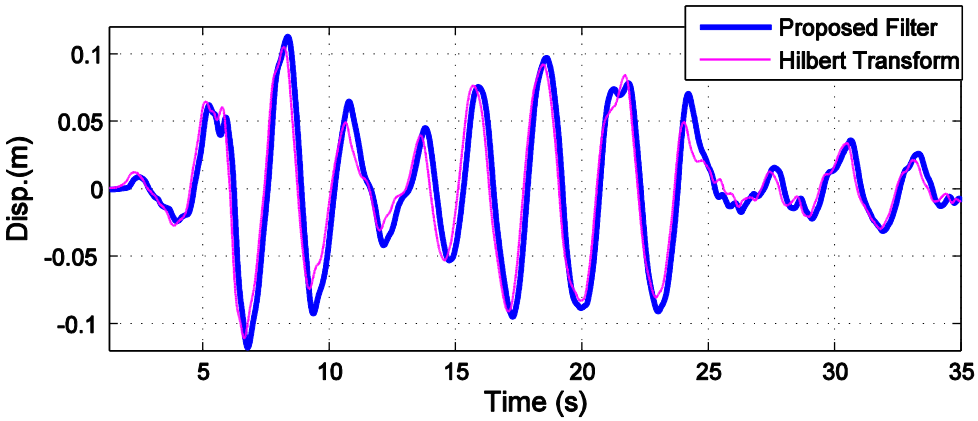

Fig. 5.2. *Hilbert transform of displacement and preceded displacement obtained by proposed causal filter.*

5.3 Comparison of Causal Approximations

In this section, the proposed filter-based causal method is compared to two Biot model designs and one Makris model design by looking at transfer functions and time-history analyses. All causal approaches explored have a tunable parameter which affects the frequency range of favorable performance. This paper provides insight into the selection of the proposed, Biot, and Makris model parameters as applied to the problem of low-frequency structures.

For the first Biot model, designated Biot 1, ε is chosen as 0.611 rad/sec. This selection produces the same magnitude damping force as the ideal noncausal case at the natural frequency of the structure (see Fig. 5.4). For the second Biot model, designated Biot 2, ε is chosen as 1.6 rad/sec. This selection comes from ad-hoc tuning to improve the forced vibration response of the model. Unlike the other models, the Biot model showed significant tradeoff in design performance during free and forced vibrations. Biot 1 achieves good performance under free vibration and Biot 2 is tuned to achieve good performance under forced vibration (for the input ground motion explored). For the Makris model, Makris [9] suggests that the arbitrary constant ε can be chosen such that the storage modulus matches a realistic stiffness value at any finite frequency. Here, ε is chosen as 1.57 rad/sec (i.e., ω_n). This selection produces the same storage modulus and loss modulus (Fig. 5.3) and the same magnitude and phase (Fig. 5.4) as the ideal noncausal case at the natural frequency of the structure. The design of the Makris model also results in the closest time domain performance match to the noncausal case considering both forced and free vibration. An SDOF system is considered with mass of 5 metric tons, natural frequency of 0.25 Hz (1.57 rad/sec), loss factor η of 0.4, and no inherent damping. Five realizations of RILD are considered: (1) ideal noncausal, (2) Biot 1, (3) Biot 2, (4) Makris model, and (5) the proposed model.

Fig. 5.3 shows storage modulus and loss modulus for all the models. Note that the storage modulus and loss modulus include both the linear stiffness term and the model for RILD. For the storage modulus, the Makris model and the proposed model achieves the same value as the noncausal approach at the natural frequency of the

structure. The storage modulus of the proposed model is always positive and defined, while in the Makris model it becomes negative for $\omega < exp(1.57/\eta)\varepsilon$ and is undefined as $\omega \to 0$. Both Biot models diverge from the noncausal storage modulus beyond $\omega = 0$. For the loss modulus, the Makris model exhibits the exact same response as the noncausal method since both have the same imaginary component in the stiffness element. Both Biot models converges to noncausal response at higher frequencies. Both the proposed model and the Makris model have the same value as the noncausal case at the natural frequency of the structure.

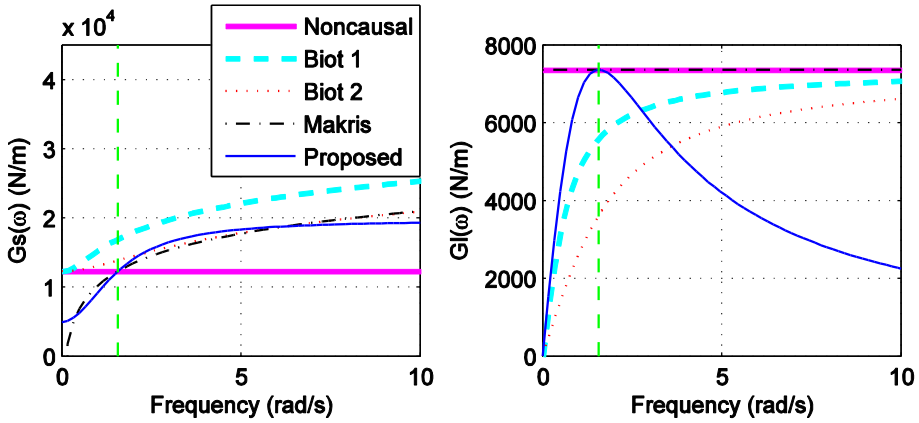

Fig. 5.3. *Storage and loss modulus transfer function for causal and non-causal models.*

5.3.1 Frequency Domain Comparison

In this section, different response transfer functions are compared for the three causal models and the noncausal model. Fig. 5.4 presents magnitude and phase of damping force transfer function from input displacement to output damping force. These plots only show the RILD term and do not include the linear spring force for any of the models.

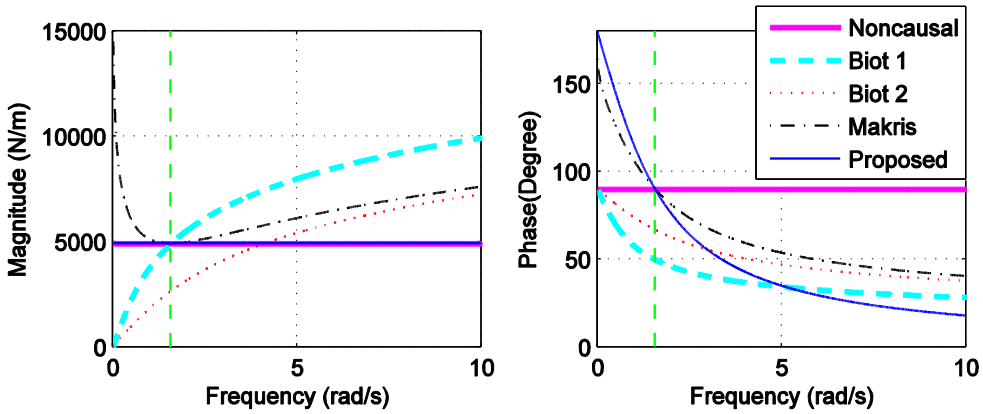

Fig. 5.4. *RILD model transfer functions (damping only, no stiffness term).*

As mentioned earlier, the Biot 1 model and the Makris model were tuned so that they have the same restoring force as the noncausal method at the natural frequency of the structure. The magnitude of the restoring force for these models diverges at lower and higher frequencies. The proposed model exhibits the exact restoring force as the noncausal model (in magnitude) over all range of frequencies. Phase plot of the stiffness element depicts that both the Makris and proposed model have 90° phase shift at the natural frequency of the structure, matching the noncausal model. The Makris model has a more accurate phase response than the proposed model considering a broad range of frequencies. Both Biot models give superior phase performance in the low frequency range.

In summary, each model has its own benefits. The Biot model gives the best phase property in the low frequency range, the Makris model gives better phase property than that of proposed causal filter in the overall frequency range but at the expense of distorted magnitude, and the proposed causal filter gives a perfect match with the ideal noncausal filter in the magnitude but at the expense of distorted phase.

Fig. 5.5, Fig. 5.6, and Fig. 5.7 present the transfer functions of the SDOF system from input ground motion to outputs of displacement, absolute acceleration, and damping force, respectively. Dashed line in all the figures shows natural frequency of the SDOF system. The Makris and the proposed model show similar behavior, matching well with the noncausal case in all transfer function plots. As per design, all causal models (except for Biot 2) match the noncausal model well at the natural frequency of the structure in both magnitude and phase. The two Biot models exhibit higher peaks when compared to other two causal approaches. Overall, the Makris model and the proposed model demonstrate the closest match with noncausal (ideal) model over a broad frequency range.

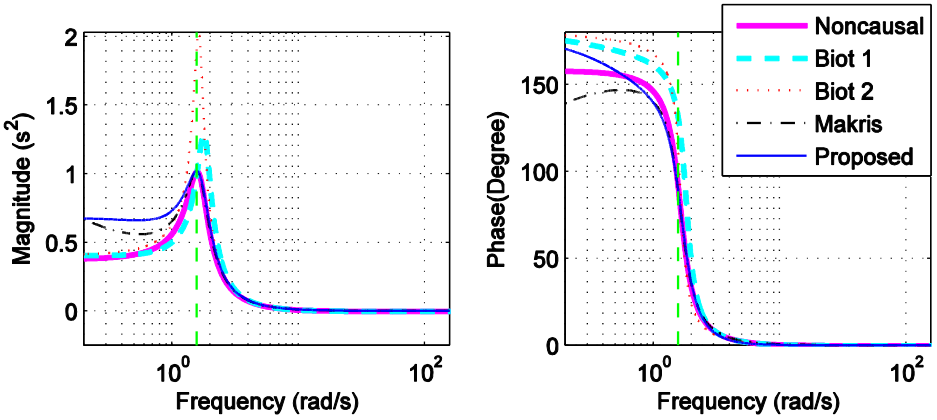

Fig. 5.5. *Displacement response transfer function for causal and noncausal models.*

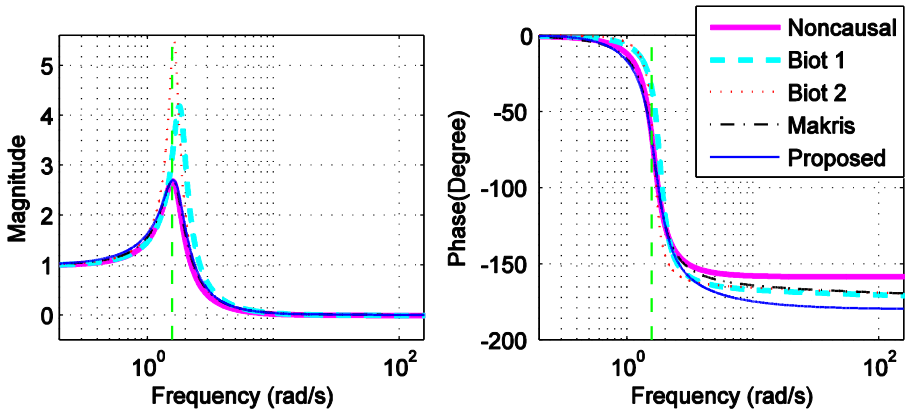

Fig. 5.6. *Absolute acceleration response transfer function for causal and noncausal models.*

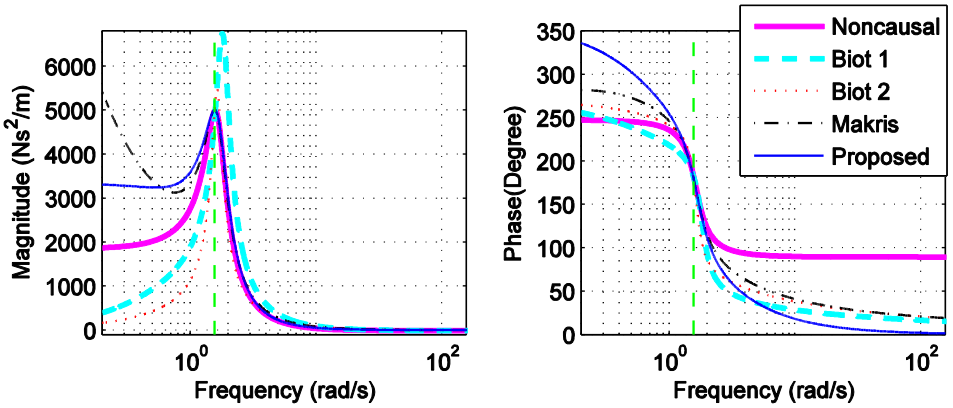

Fig. 5.7. *Damping force response transfer function for causal and noncausal models.*

5.3.2 Time History Responses Comparison

In this section, time history responses of all models are calculated in the frequency domain and compared. Fig. 5.8 and Fig. 5.9 compare the results of the causal and noncausal models when the structure is subject to the full-scale Hachinohe record. Fig. 5.8 shows displacement and absolute acceleration response time histories on the left and a zoomed-in view of the same plot on the right. Fig. 5.9 shows the time history of damping force and damping force hysteresis. As it is expected from transfer function plots, both the Makris and proposed causal approaches show similar seismic

response and can better track the noncausal responses when compared to the Biot models. The Makris and the proposed models have the exact 90° phase shift at the natural frequency of the structure and therefore able to better track the noncausal responses for this structure and ground motion. The Biot models clearly have a large peak magnitude in Fig. 5.5, Fig. 5.6, and Fig. 5.7 which can detract from the performance. The Hachinohe record has significant frequency content larger than the natural frequency of the structure, leading to poor performance for the Biot 1 model when compared to the Biot 2 model. Because of ad-hoc tuning to this earthquake record, the Biot 2 model shows a better transfer function match with the noncausal model at higher frequencies than the natural frequency of the structure.

The greatest difference between the proposed method and noncausal method can be seen in the absolute acceleration and damping force time histories, both showing slightly larger peaks for the causal model. This is also true for the Makris model. A major benefit of RILD is that the acceleration and damping force in a low-frequency structure are reduced. Deviations from ideal noncausal RILD to satisfy causality will hinder the reduction in acceleration and damping force.

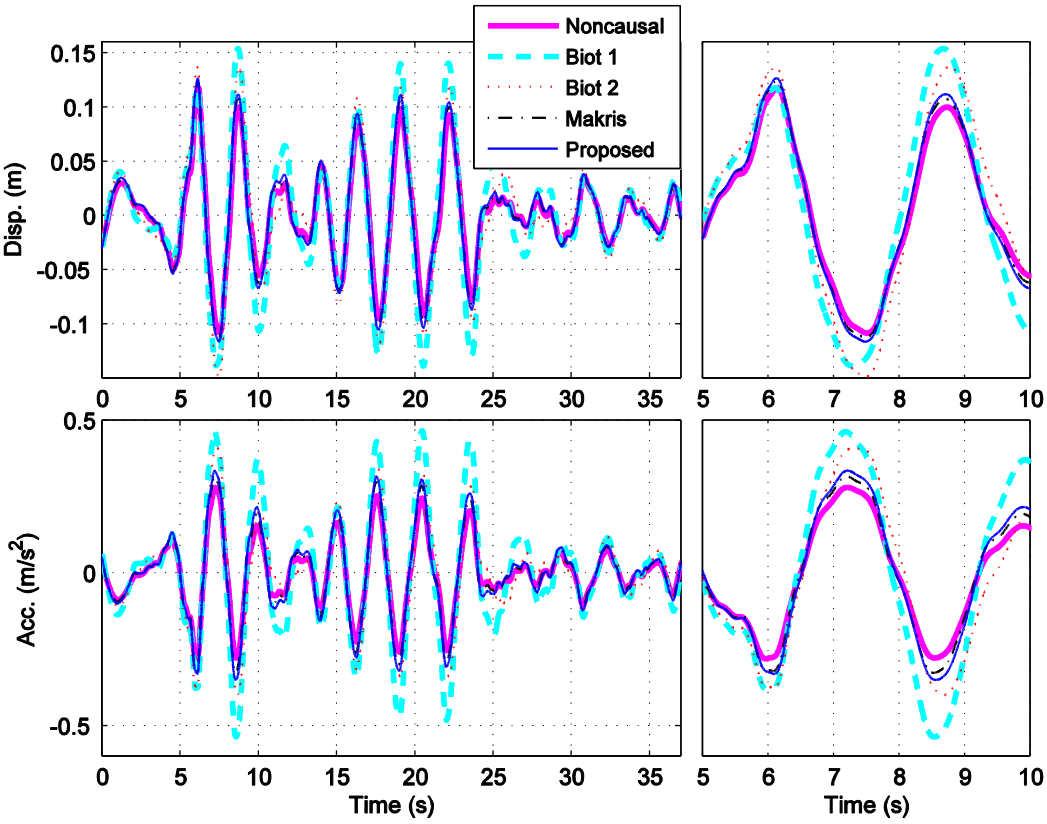

Fig. 5.8. *Causal and noncausal displacement and absolute acceleration for the Hachinohe record.*

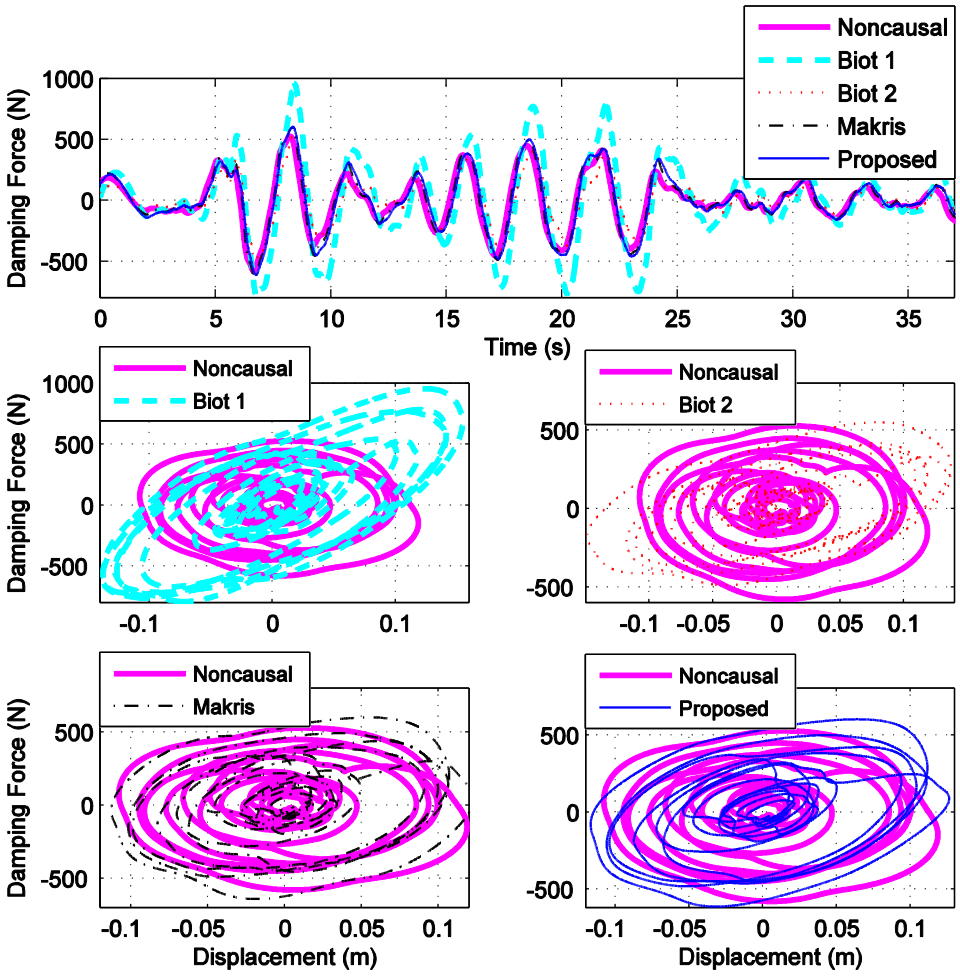

Fig. 5.9. *Causal and noncausal damping force for the Hachinohe record.*

As noted earlier, each model has its own benefits. Overall, the proposed model and the Makris model perform the best when compared to the noncausal responses. The advantage of the proposed model over the other two causal methods is its simplicity leading toward practical applications. The model itself can be implemented using an analog all-pass filter or as a digital all-pass filter using standard discretization in time and standard numerical integration techniques. The only measurement needed to implement this method is the displacement of the device and can easily be measured by an LVDT sensor. The filter parameter is based on the

fundamental natural frequency of the structure and can be adjusted in real-time using adaptive control. Additionally, the proposed model has a positive storage modulus over all frequencies and is defined for $\omega = 0$.

5.4 Behavior of CFB Model

For the proposed CFB model for RILD, if the response frequency exceeds the filter frequency, the hysteresis will exhibit a positive skew; if the response frequency is less than the filter frequency, the hysteresis will exhibit a negative skew. This can be clearly seen in Fig. 5.10. The noncausal RILD element is shown along with the CFB element where the filter frequency is set as 0.25 Hz (1.57 rad/s). As depicted in Fig. 5.10, if the input frequency of a displacement sine wave exactly matches the frequency of the CFB element (0.25 Hz), then the CFB element will exactly match the noncausal RILD element. However, an input frequency of 0.4 Hz leads to a positively skewed hysteresis and an input frequency of 0.1 Hz leads to a negatively skewed hysteresis. Fig. 5.10, clearly shows a need for an adaptive CFB algorithm in which the filter frequency can be adjusted in real time based on the actual response frequency of the structure.

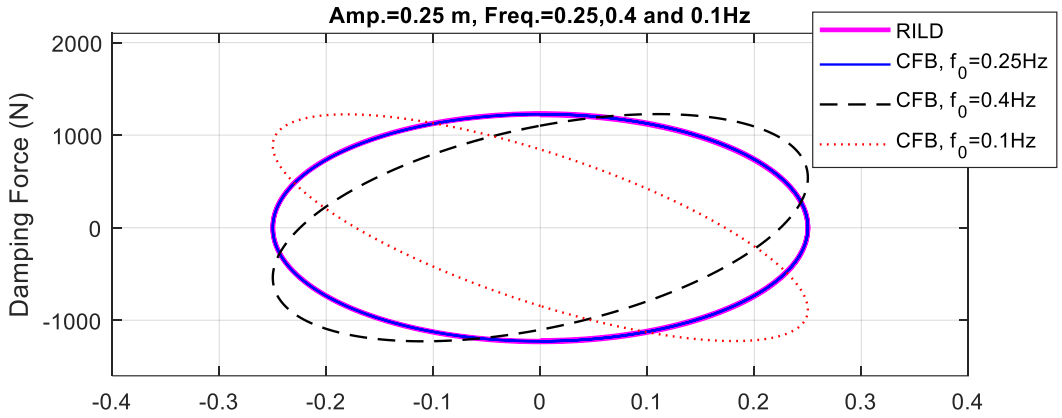

Fig. 5.10. *Steady states hysteresis plots of RILD and CFB damping elements with variable harmonic frequencies.*

5.5 Semi-active and Passive Control to Achieve RILD

To realize RILD in a practical system, the force calculated using the proposed CFB approach can then tracked by a control device, such as a magnetorheological (MR) damper as used in this dissertation. The use of visco-plastic dampers (such as MR dampers) to protect base-isolated structures has been explored in the literature [54, 55]. Considering the natural phase match between RILD and the restoring force of damping devices, semi-active dampers are simpler and more suitable for mimicking RILD than active devices. Both numerical simulations and shake table tests are conducted to demonstrate the performance of the proposed causal approach applied to semi-active devices in Chapters 6 and 7.

Furthermore, passive implementation of RILD is investigated in Chapter 10 where a combination of passive mechanisms is proposed to approximate ideal RILD performance in base-isolated structures.

Chapter 6: Base Isolation

This chapter presents the application of causal RILD to a base-isolated structure. Results for a SDOF base-isolated specimen incorporating proposed causal RILD is compared to that of noncausal numerical analysis for a same structure.

6.1 Experimental Setup

Experimental studies are needed to ensure that the desired forces can be physically and practically realized and furthermore match the ideal noncausal RILD case. Shake table testing offers a simple means to experimentally evaluate the performance of a structure subject to a ground motion. Tohoku University has a 3m × 3m bi-directional shake table and a steel frame specimen that is well-suited for this study. The structure of interest is a base-isolated specimen with supplemental damping at the isolation layer. Through the proposed algorithm, the supplemental damper will behave as a RILD device.

6.1.1 Base-isolated Specimen

The specimen is a single-story structure mounted on an isolation system. The isolation system consists of four linear bearing blocks that can slide on two linear guide rails with very low friction and four steel coil springs to provide restoring forces. The stiffness of the isolated specimen is 12.3 kN/m. Steel weights are mounted on the top and the base of the specimen. The roof mass including the mass of the steel frame members is 2.08 metric tons, and the base mass including the mass

of the steel base frame is 2.92 metric tons. When the braces of the specimen are locked, the specimen acts as an SDOF system with a mass of 5 tons and natural frequency of 0.25 Hz. Fig. 6.1 shows an image of the base isolated specimen with braces locked.

Fig. 6.1. *Base-isolated specimen with braces locked.*

6.1.2 MR Damper Specimen

Semi-active devices provide a straightforward means to physically deliver RILD. MR dampers are well-studied semi-active devices and an excellent alternative for this application. The response of the damper is naturally in phase with the velocity of response and the magnitude of the response can be adjusted online through a control algorithm. The controllable properties of MR dampers are derived from the internal MR fluid. In the presence of a magnetic field, the fluid changes from a linear viscous fluid to a semi-solid with controllable yield strength [56]. The source of the magnetic field is an electromagnet, excited by an external current which can vary as required by a control algorithm.

To explore causal RILD, a long stroke MR damper is placed at the isolation level. A schematic of the long stroke damper is shown in Fig. 6.2. The length of the damper in neutral position is 2,305 mm and the stroke is ± 400 mm.

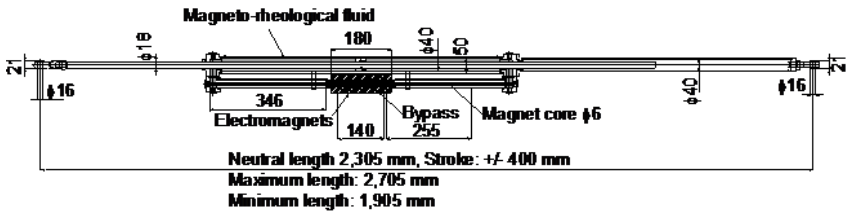

Fig. 6.2. *Long-stroke MR damper.*

Many semi-active control algorithms are available to track a desired force for the control of an MR damper. In this case, the proposed all-pass filter will produce a desired force within the range of forces achievable by the MR damper. The MR damper of this study responds very quickly to changes in current. Using a traditional bang-bang type controller to track this desired force was found to produce severe oscillations in the measured force. Hence, a feedforward-only control algorithm was used to track the desired force without oscillation.

To derive the MR damper control algorithm, a simple Bingham model is employed to represent the mechanical properties of the damper. The total restoring force of the MR damper f_{MR} is obtained from the sum of a viscous force generated by a dashpot element and a controllable resistance force generated by a friction slider element. Both the dashpot element and friction element parameters are assumed to vary with input voltage V to the electromagnets coils in the damper. Based on sine wave characterization tests for a set of displacements, velocities, and voltages, a simplified and approximate relationship was developed between the total damping force and input voltage:

$$f_{MR} = 0.0001\,V^2 + 0.0072\,V + 0.0489 \tag{6.1}$$

where f_{MR} is the damping force in kN and V is the input voltage in Volts. Equation (6.1) shows that the restoring force nominally depends only on the input voltage. For the MR damper studied, the restoring force was found to be nominally independent of the displacement and velocity of the damper. Force-displacement and force-velocity hysteresis loops for multiple input voltage levels confirm that the behavior is most heavily dominated by the controllable input voltage.

Solving Equation (6.1) for the input voltage V required to achieve a desired force, the equation can be rewritten as:

$$V = 5\sqrt{400\,|f_{MR}| + 32.28} - 36 \tag{6.2}$$

Equation (6.2) determines the command voltage for the MR damper based on the desired damping force. In this controller, if the measured and desired force have the same sign, the input voltage to the MR damper is computed using Equation (6.2); however, if they have opposite signs, the input voltage to the MR damper is set to zero. Furthermore, a saturation block also considered in the controller to keep the applied voltage to the damper in a range of 0 to 50 Volts. Fig. 6.3 illustrates an experimental example of the tracking of the desired force by the measured force using this algorithm. The results correspond to an SDOF system with mass of 5 metric tons, natural frequency of 0.25 Hz, loss factor η of 0.6, and no viscous damping subjected to 50% Hachinohe earthquake ground motion. The desired force is determined using the proposed all-pass filter. It is worth mentioning that the passive-off (constant 0 V)

limitation of the damper is about 0.1 kN; therefore, the damper force cannot generally decrease beyond this limit except under very small velocities.

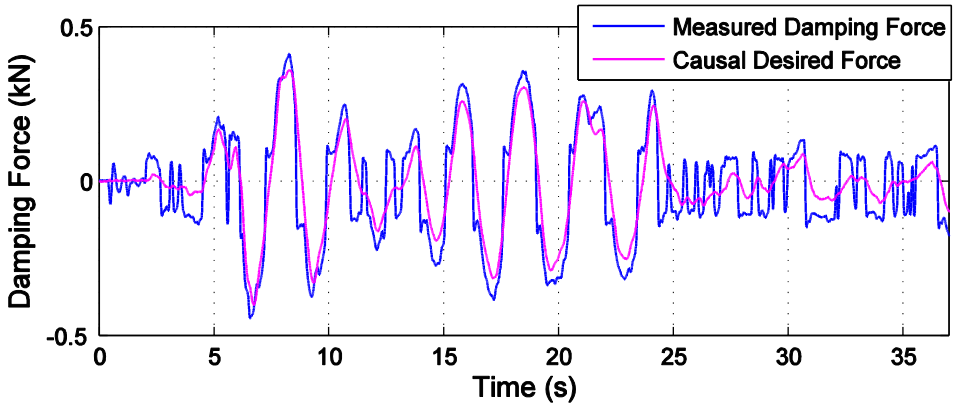

Fig. 6.3. *Desired and measured damping force using force tracking control algorithm.*

6.2 Experimental Results and Discussion

A series of shake table tests were conducted at Tohoku University to examine the performance of the proposed causal realization of RILD. Load cells, accelerometers, and displacement transducers were used to capture damping force, acceleration, and displacement of the system respectively. In the experiments, the specimen is taken as the base-isolated specimen with MR damper installed in the isolation layer. The loss factor η may be freely selected, influencing the magnitude of the causal RILD force to be tracked by the MR damper. Unless otherwise noted, η is selected as 0.6. The noncausal analyses are performed in the frequency domain using identified structural parameters and an ideal RILD device in place of the MR damper.

To avoid significant shake table drift, the reference earthquakes are passed through a 2-pole Butterworth high-pass filter with a cutoff frequency of 0.25 Hz. Because the earthquakes used in the experimental tests have a majority of their

frequency content above the filter cutoff frequency, the effect of pre-filtering on the earthquake frequency content is minimal.

6.2.1 Comparison of Causal and Non-causal Approaches

In this section, the ability of the proposed causal approach to achieve RILD is evaluated. Results are compared to ideal RILD determined through a frequency domain analysis. Fig. 6.4 illustrates displacement, acceleration and damping force time histories in both experiment (causal) and frequency domain (noncausal) when the structure is subject to the Hachinohe earthquake with 50% intensity. Fig. 6.4 also includes the MR damper hysteresis in comparison to noncausal hysteresis from frequency domain analysis.

As it is shown in Fig. 6.4, the experimental causal displacement has a very good match with noncausal displacement from frequency domain analysis. However, the experimental acceleration has larger peaks than those of the frequency domain analysis. This observation is consistent with numerical simulation results presented previously and is due to an inability to exactly reproduce the greatly reduced accelerations of true RILD. Fig. 6.4 also depicts the experimental causal damping force recorded during the test as compared to the analytical noncausal damping force. There is a very good agreement in both time history and hysteresis, illustrating that both the calculation of the desired causal force and tracking of the desired causal force using the MR damper perform very well.

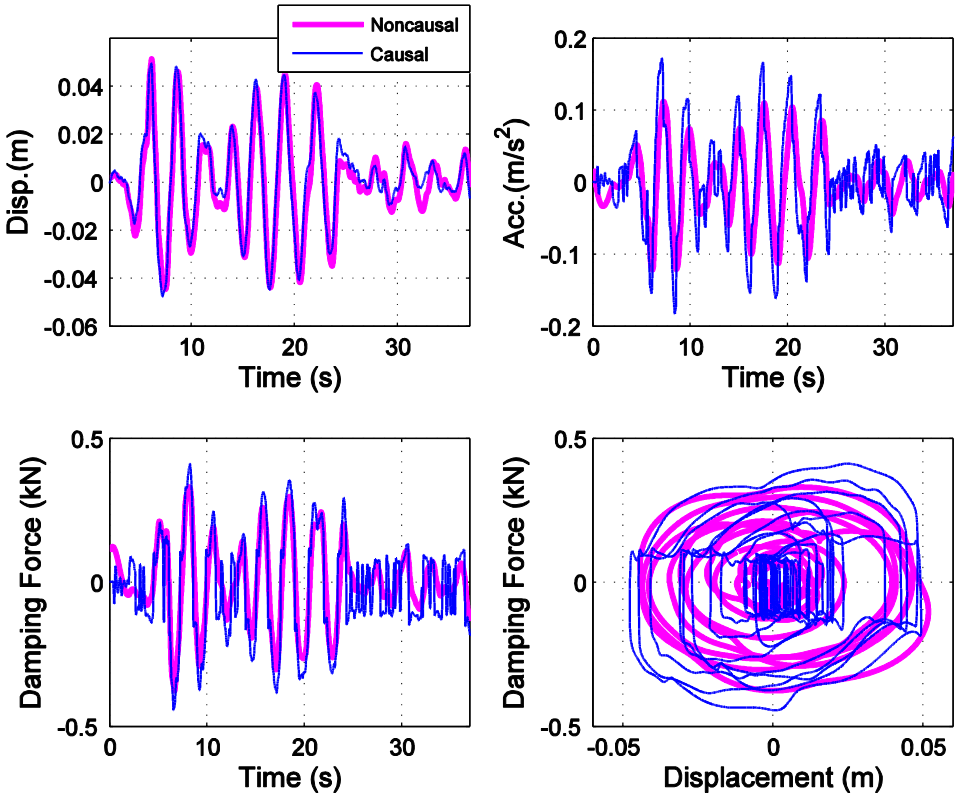

Fig. 6.4. *Causal and noncausal displacement, velocity, absolute acceleration, and hysteresis for the Hachinohe record at 50% amplitude scaling.*

To illustrate the proposed control approach under an earthquake with different frequency content, 30% intensity of the Kobe earthquake was applied to the structure in both experiment and numerical analysis. Fig. 6.5 illustrates displacement, absolute acceleration, damping force, and hysteresis of the experimental tests versus the same quantities from non-causal analysis.

For the case of Kobe earthquake, again there is a close resemblance between numerical simulation and experimental test for displacement time history as well as damping force time history as it is depicted in Fig. 6.5. Larger peaks of experimental acceleration are seen for this case, similar to the Hachinohe earthquake. The peaks are more pronounced for the Kobe earthquake, due to larger forced vibration away from

the natural frequency of the structure. Fig. 6.5 also shows experimental and analytical hysteresis loops. For the case of Kobe earthquake, the experimental hysteresis does not match the analytical hysteresis as well as for the Hachinohe earthquake. The Kobe earthquake caused the structure to respond at both its natural frequency and with a forced vibration of about twice its natural frequency. Using the proposed filter-based method, response at a frequency larger than the natural frequency of the structure will introduce a phase lag to the desired force. This produces a positively skewed force hysteresis and larger acceleration response. Aside from a slightly degraded performance, the proposed approach works well even when the response drifts away from the natural frequency of the structure.

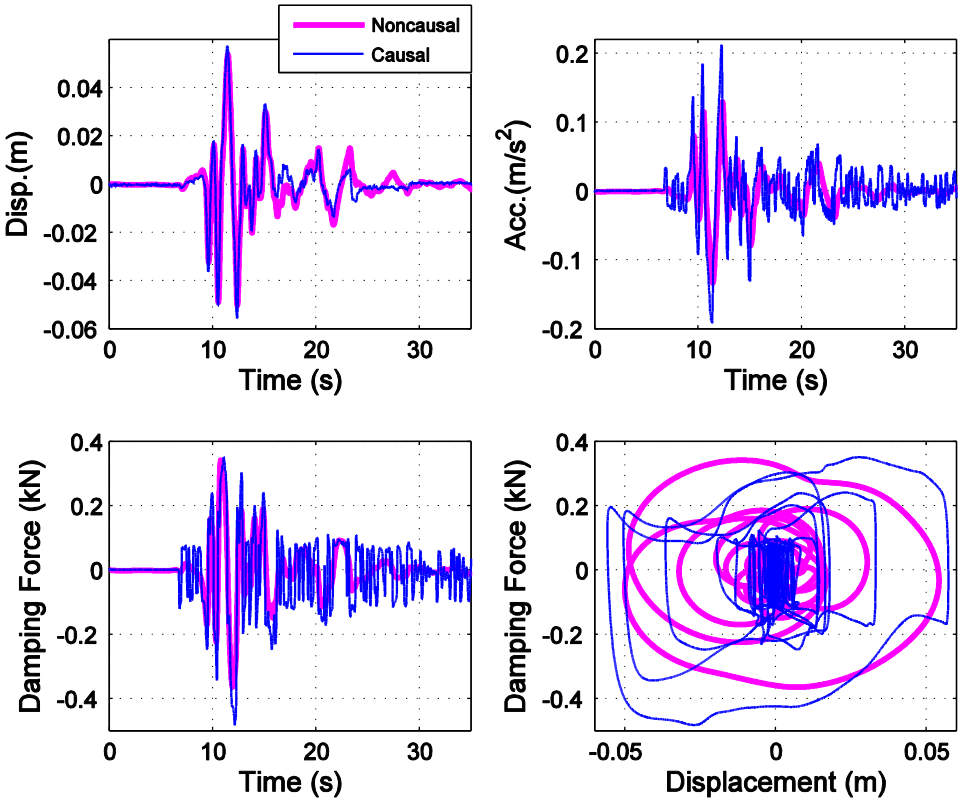

Fig. 6.5. *Causal and noncausal displacement, velocity, absolute acceleration, and hysteresis for the Kobe record at 30% amplitude scaling.*

6.2.2 Control Device Limitation to Consider

To further investigate the proposed causal RILD method, different η values were evaluated for the Hachinohe earthquake ground motion. Fig. 6.6 illustrates experimental hysteresis for the structure with applied 50% Hachinohe earthquake for η values of 0.4, 0.6, together with passive-off (constant 0 V) and passive-on (constant 30 V) cases applied to the MR Damper.

As it is clear from Fig. 6.6, causal hysteresis for η values of 0.4 and 0.6 fall between the lower limit of passive-off case and upper limit of passive-on case. Thus, by selecting η in this range, the desired force throughout the time history is nominally achievable by the MR damper. A very large η value may lead to saturation of the MR damper force at the passive-on performance and likewise a very low for η value may lead to a force that cannot decrease beyond the passive-off performance. Furthermore, during very low velocity excitations, the passive-off limit may lead to a nominal level minimum force for any value of η. This phenomenon is a limitation of the MR damper, meaning that the MR damper must be designed with a controllable range of forces that overlap with the desired range of RILD force. This is not a strict requirement, since large displacements or large values of η that may produce an unachievable RILD force would cause the MR damper to function in the passive-on state, which still dissipates a large amount of energy and is in phase with the velocity.

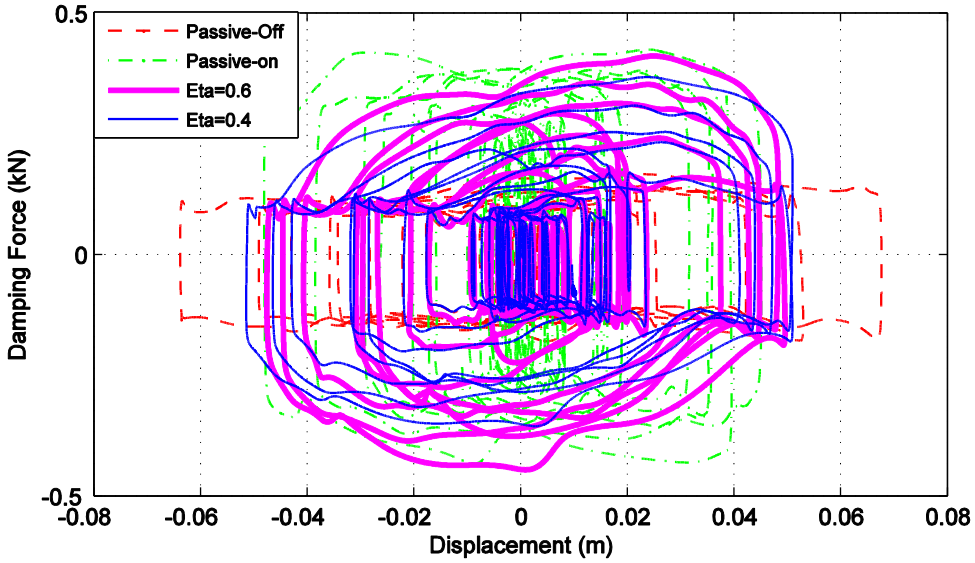

Fig. 6.6. *Experimental hysteresis for different η values, passive-off, and passive-on cases for the Hachinohe record at 50% amplitude scaling.*

Chapter 7: Inter-Story Isolation

This chapter explores the application of RILD to inter-story isolation. The goal is to reduce isolation layer displacements without compromising the benefits of isolation including low isolation layer forces and low accelerations of the superstructure. Substructure RTHS is used to evaluate the inter-story isolated structure. Here, the superstructure is experimentally represented by a base-isolated specimen while the substructure is numerically represented through a numerical model. The experimental and numerical substructures are linked in a loop of action and reaction to capture the dynamic response of the total structure. Results for a MDOF inter-isolation structure incorporating proposed causal RILD is compared to that of noncausal numerical analysis for a same structure. Additional performance comparisons are made to the MR damper in both passive-on and passive-off control modes and a numerical simulation of linear viscous damping in the isolation layer.

For an inter-story isolation system, there are two obvious choices for ω_n in Equation (5.13) based on the dynamics of the structure. Stories above the isolation layer will freely vibrate at their own natural frequency, making the fundamental natural frequency of the superstructure a good choice. Also, the stories below the isolation layer will act as a filter to the ground motion, effectively causing forced vibration to the superstructure at the fundamental natural frequency of the substructure. Considering forced vibration, the fundamental natural frequency of the

substructure is also a good choice. Both options for ω_n are evaluated and results are discussed in this research.

7.1 Structural Model

In this study, a real 14-story high rise building (IFB) where the isolation layer is installed between 9th and 10th story is used for investigations. This structure is idealized as a 15-DOF lumped mass model which is shown in Fig. 7.1.

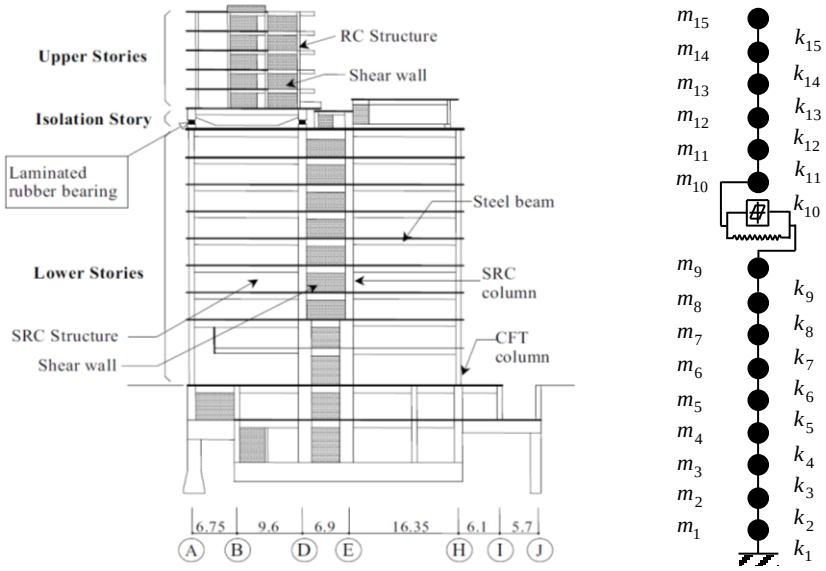

Fig. 7.1. *Structural system of the IFB and related shear model.*

The structure is divided into two parts. The first 9 stories below the isolation layer are classified as the substructure and 6 stories above the isolation layer as the superstructure. In this study, the RILD is proposed as supplemental damping in the isolation layer. The superstructure will be idealized as a SDOF system such that a base-isolated SDOF experimental specimen can represent their dynamics. The substructure will be simulated numerically. The dynamic response of the total structure will be evaluated through shake table RTHS. With the SDOF assumption for

the superstructure, a 10-DOF model is created with matching dominant natural frequencies and mode shapes as the full model shown in Fig. 7.1.

7.1.1 Experimental Specimen and MR damper Specimen

The isolation layer causes the superstructure to response mainly in its first mode of vibration. A base isolated specimen will be used to represent the isolation layer and superstructure. The same 3m × 3m bi-directional shake table specimen and MR damper from Tohoku University that has been used for SDOF testing, was also used here. The IFB building contains supplemental dampers in the isolation layer. To replicate the supplemental dampers, the same physical MR damper is added to the isolation layer of the test specimen. Similarly, same feedforward-based control algorithm was found to provide adequate tracking of the desired MR damper force.

7.1.2 Prototype Structure Properties

Prototype structural properties (10-DOF model) are selected to match the scale of the experimental specimen while maintaining similar natural frequencies and mode shapes as the original structure (15-DOF model). The original model mass is scaled by 1/2940, resulting in a match between the original superstructure mass and the SDOF experimental specimen. The stiffness of the isolation layer in the prototype structure is selected to create a superstructure with identical natural frequency as the experimental specimen, 0.25 Hz. Likewise, stiffness values of floors 1 through 9 are uniformly scaled such that the prototype structure has similar dominant natural frequencies and mode shapes as that of the original model of the IFB. Mass and stiffness values are reported in Table 7.1. The natural frequencies of the prototype

structure are 0.24 Hz, 0.83 Hz, 2.32 Hz, 3.88 Hz, 5.49 Hz, which compare well to the natural frequencies of the original model as 0.29 Hz, 1.04 Hz, 2.93 Hz, 4.89 Hz, and 6.89 Hz. Fig. 7.2 represents the first three mode shapes of both of these models. Note that the prototype structure's 10th floor displacement is repeated for all superstructure floors for comparison with the original structure. The prototype structure can well represent the dynamics of the simplified original model of IFB.

The base isolated specimen has 2.4% damping without considering supplemental damping and hence the damping coefficient of the 10th story in the prototype structure is chosen as 0.376 kN·s/m to be compatible with the experimental specimen. For the substructure, damping coefficients are chosen as 20.0 kN·s/m for each floor which results in damping ratios of the total structure to be 2.23%, 2.80%, 7.74%, 12.9%, and 18.1% in the first five modes.

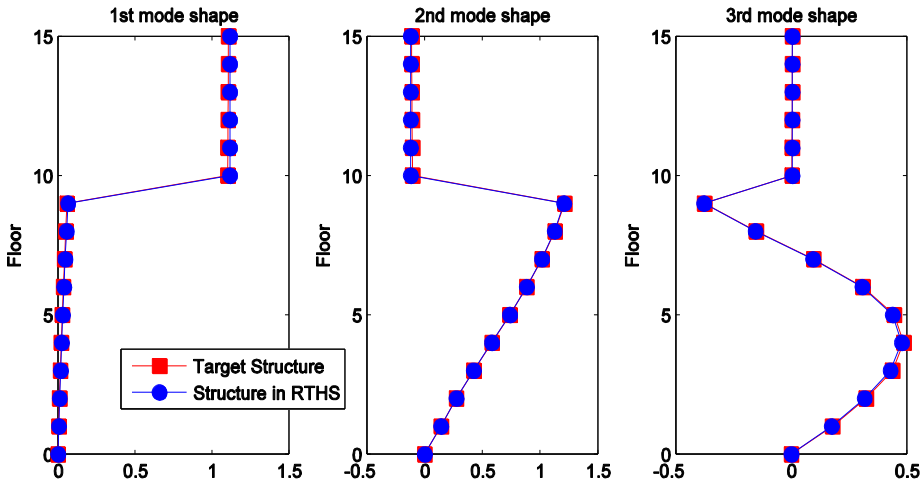

Fig. 7.2. *First three mode shapes of the prototype structure and target structure.*

Table 7.1. Parameters of the 10-story prototype structure.

Floor/Story	Floor Mass (kg)	Story Stiffness (kN/m)	Story Damping (kN·s/m)
1	1,847	2,642	20.0
2	1,880	2,752	20.0
3	1,770	2,354	20.0
4	1,763	2,109	20.0
5	1,760	1,959	20.0
6	1,730	1,836	20.0
7	1,670	1,710	20.0
8	1,670	1,602	20.0
9	4,317	1,539	20.0
10	5,000	12.30	0.376

7.2 Preliminary numerical study of RILD for inter-story isolation

In this section, the seismic performance of the scaled 10-DOF IFB building model is evaluated under six ground motion records with different dominant frequency content. Three models are considered for the supplemental damping in the isolation layer: discrete RILD and discrete viscous damping elements. In this section, the intensities of the ground motions are scaled so that the isolation layer drift of the structure with the RILD element is 0.3 m for an η value of 0.4. Same η value of 0.4 is used for CFB controller and the viscous damping coefficient then is selected to achieve an average of 0.3 m drift in the isolation layer for all records except Sakishima. In this way, both damping models restrict the isolation layer drift to similar levels and damping coefficients are consistent across all records. It is worthwhile to mention that due to low frequency content of the Sakishima record, a very high value of damping coefficient is needed for viscous damping to achieve 0.3

m drift at the isolation layer. Therefore; to have a fair comparison, viscous damping coefficient is calibrated only based on the remaining five earthquake records to reach an average 0.3 m drift at the isolation layer. Fig. 7.3 shows numerical simulation peak responses for the scaled model with both damping types. The ground motion records are ordered in Fig. 7.3 from left to right based on relative low to high frequency content.

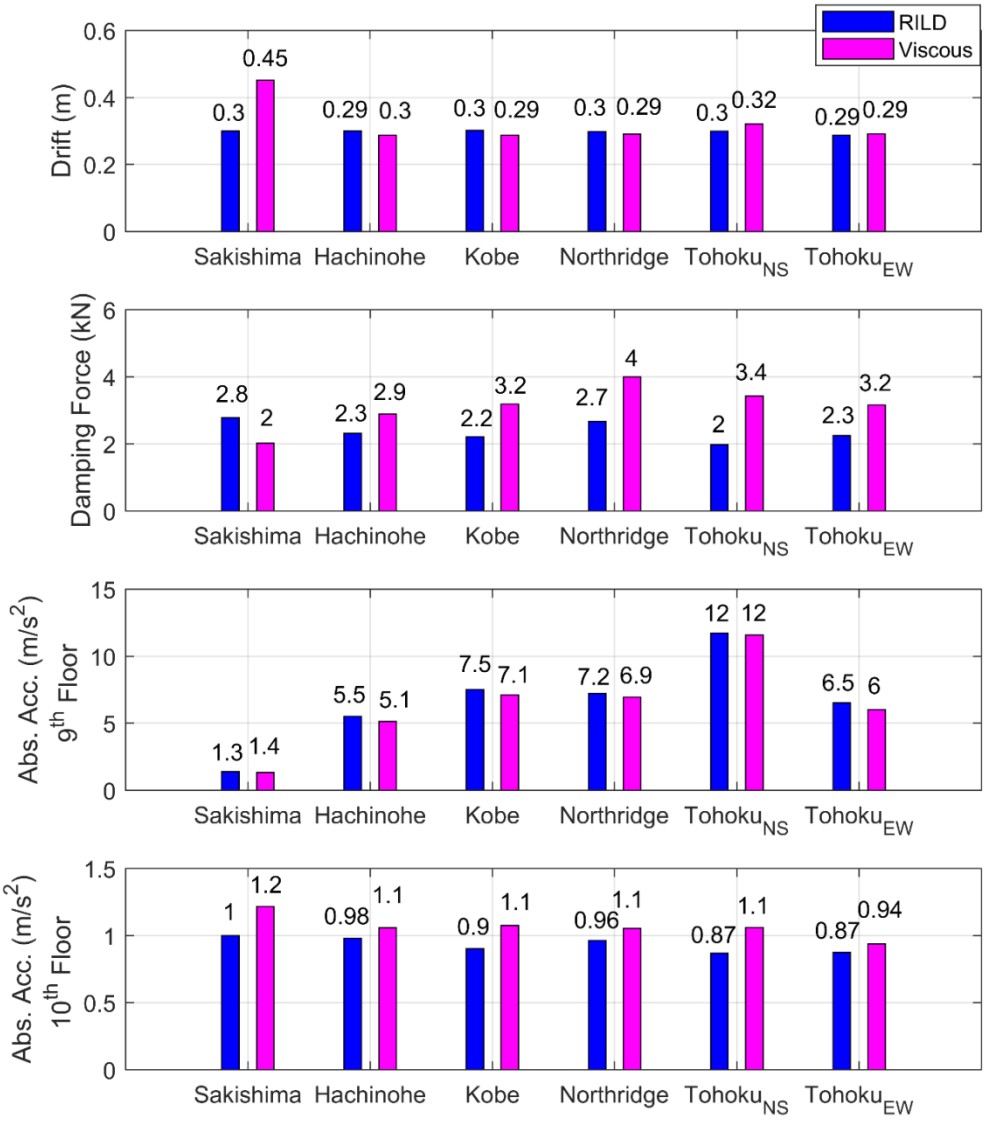

Fig. 7.3. *Peak response comparison of RILD and viscous damping.*

As it is shown in Fig. 7.3, while RILD and viscous are set to have similar isolation layer drifts for Hachinohe, Kobe, Northridge, $\text{Tohoku}_{\text{NS}}$, and $\text{Tohoku}_{\text{EW}}$ records, viscous damping results in much higher damping forces leading to higher superstructure absolute accelerations. These five earthquakes have medium to high frequency content excitations relative to the IFB's superstructure fundamental natural frequency, resulting in larger generated damping forces for the discrete viscous damper as compared to RILD. On the other hand, for Sakishima ground motion, larger isolation layer drift and superstructure absolute acceleration (10^{th} DOF absolute acceleration) is observed for the structure equipped with discrete viscous damper as compared to RILD. As discussed earlier, this is because of the low frequency content of this record, leading to smaller viscous damping forces as compared to RILD element. However, for the rest of the records vibrations at higher frequencies than the natural frequency of the substructure will result in similar isolation layer drift as ideal RILD while at the same time leading to lower superstructure absolute accelerations. Moreover, both damping models result in similar 9^{th} DOF absolute acceleration across all ground motions. In conclusion, the results shown in Fig. 7.3 highlight the advantages of RILD controller over viscous damping for inter-story isolated structures. The advantages stem from the frequency-independent RILD force, leading to good performance for both low frequency and more common high frequency content earthquakes.

7.3 Experimental Analysis through RTHS

7.3.1 Shake Table RTHS

In this research, shake table RTHS was used to evaluate structural responses of the inter-story isolated structure. A dynamic substructure approach based on Shing [47], is applied to inter-story isolation. The 10-DOF prototype structure is partitioned into experimental and numerical substructures. In this study, the isolation layer and superstructure form the experimental substructure (specimen) and the substructure forms the numerical substructure (see Fig. 3.1). Details of this approach are discussed in Section 3.4.3.

7.4 RTHS Experimental Results and Discussion

A series of shake table RTHS tests were conducted at Tohoku University to examine the performance of the proposed causal realization of RILD incorporated into inter-story isolated structures. The setup consists of a large-scale shake table, a base-isolated single-story specimen as the experimental substructure, and a dSPACE DS1103 control and data acquisition system. A load cell, accelerometer, and displacement transducer were used to capture damper force, structural acceleration, and isolation layer relative displacement, respectively. Numerical integration of the numerical substructure and interface with sensors and actuators was performed by the dSPACE digital signal processing board.

The isolation layer displacement, as measured by the displacement transducer, was used as input to the causal RILD model given in Equation (5.14). The causal RILD force is taken as the desired force to be tracked by the MR damper using

Equation (6.2). In all experiments, the loss ratio η is taken as 0.6. Initially, the fundamental natural frequency of the substructure (i.e., numerical substructure) is used for ω_n in Equation (5.13). This is later contrasted with selecting the fundamental natural frequency of the superstructure (i.e., experimental substructure) for ω_n.

7.4.1 Causal versus Non-causal RILD

First, the ability to mimic ideal RILD in a practical design will be assessed. Ideal RILD is evaluated using a fully numerical model of the prototype structure with ideal RILD (instead of MR damper) in the isolation layer. This numerical model is noncausal and therefore evaluated in the frequency domain. The causal realization of RILD is evaluated through shake table RTHS of the prototype structure using an MR damper to track the causal RILD force. Herein, ω_n is chosen as the natural frequency of the substructure (numerical substructure).

Fig. 7.4 compares structural responses of the 10th floor (isolation layer) for the noncausal analysis and the RTHS with an applied 20% amplitude Kobe earthquake. Fig. 7.5 illustrates same responses for an applied 10% amplitude Northridge earthquake. RTHS test results have a very good match with noncausal responses achieved from state space frequency domain analysis. The earthquake records considered have different frequency content; however, a good physical replication of ideal RILD is achieved in both cases. This good match is achieved through the selection of ω_n as the fundamental natural frequency of the substructure. The stories below the isolation layer filter the input ground motion before it reaches the isolation layer. The isolation layer is then excited by a narrow-banded input close to the fundamental natural frequency of the substructure. Forced vibration at this frequency

(around 1 Hz) can be seen to dominant the inter-story isolation displacement responses in Fig. 7.4 and Fig. 7.5. For all input ground motions considered, the causal realization RILD works well because the input ground motion is filtered by the substructure before reaching the isolation layer. Robust performance under a wide range of input ground motion types is important for practical applications where future inputs are unknown.

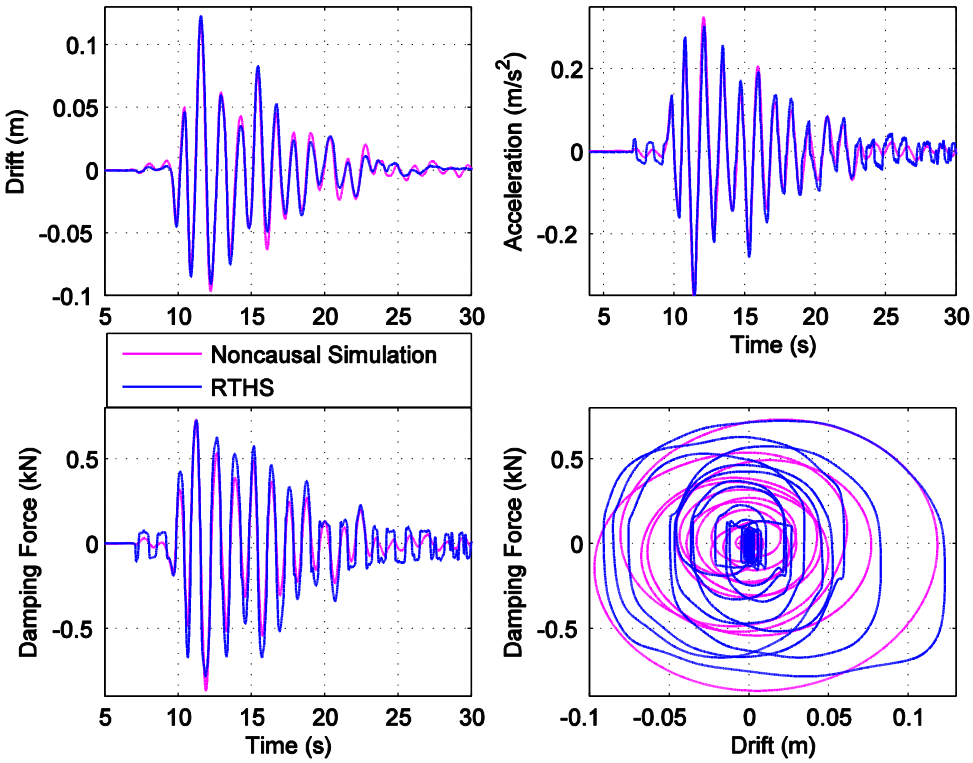

Fig. 7.4. *Noncausal RILD vs RTHS responses for 10th floor with applied 20% Kobe earthquake.*

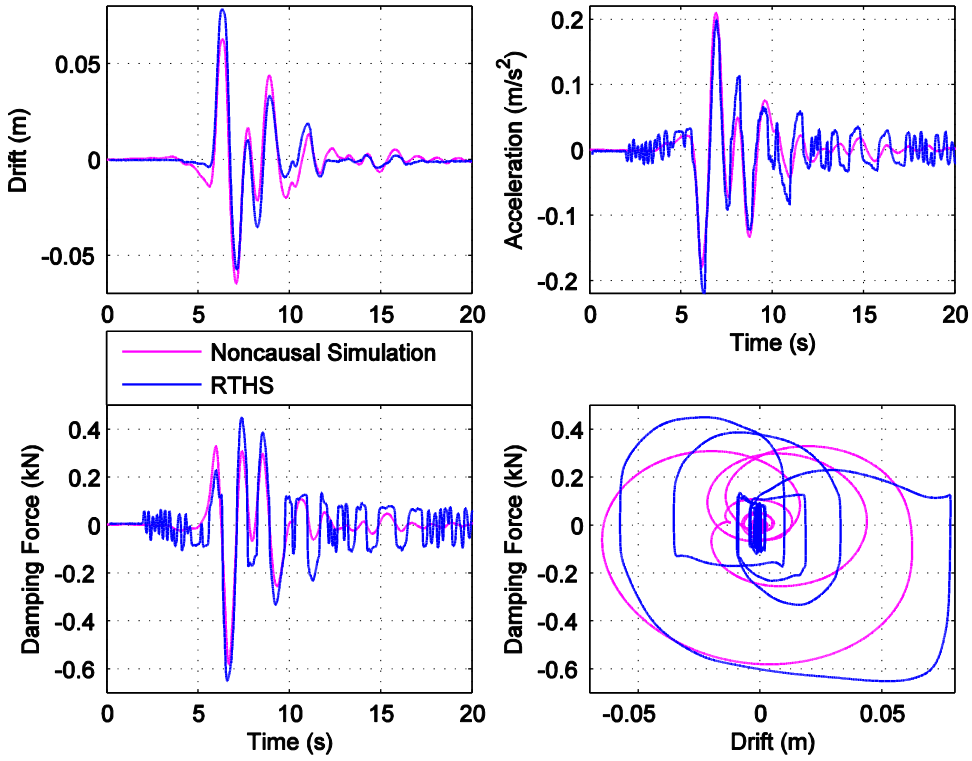

Fig. 7.5. *Non-causal RILD vs RTHS responses for 10th floor with applied 10% Northridge earthquake.*

7.4.2 Influence of CFB Model Design on Seismic Performance

To further examine the performance of the casual approximation of RILD, the fundamental natural frequency of the superstructure (experimental substructure) was used for ω_n and the prototype structures was excited with 20% amplitude of the Kobe earthquake in RTHS. The results are compared with noncausal responses computed numerically in frequency domain. Fig. 7.6 depicts RTHS and noncausal results for 10^{th} floor of the structure. As can be seen from Fig. 7.6, the hysteresis plot for the causal approximation is more skewed when compared to causal hysteresis plot in Fig. 7.4. The skewed shape of Fig. 7.6 is due to the use of the fundamental natural frequency of the superstructure for ω_n. The frequency of the forced vibration from

the substructure dominates the response of the isolation layer. Because this frequency is larger than ω_n, a positively skewed hysteresis is created by the model of Equation (5.13). Although the phase of the restoring force in Fig. 7.6 does not match the non-causal simulation, overall the displacement suppression is similar. The causal approach to achieve RILD is robust to cases where the dominant response frequency and ω_n do not exactly match.

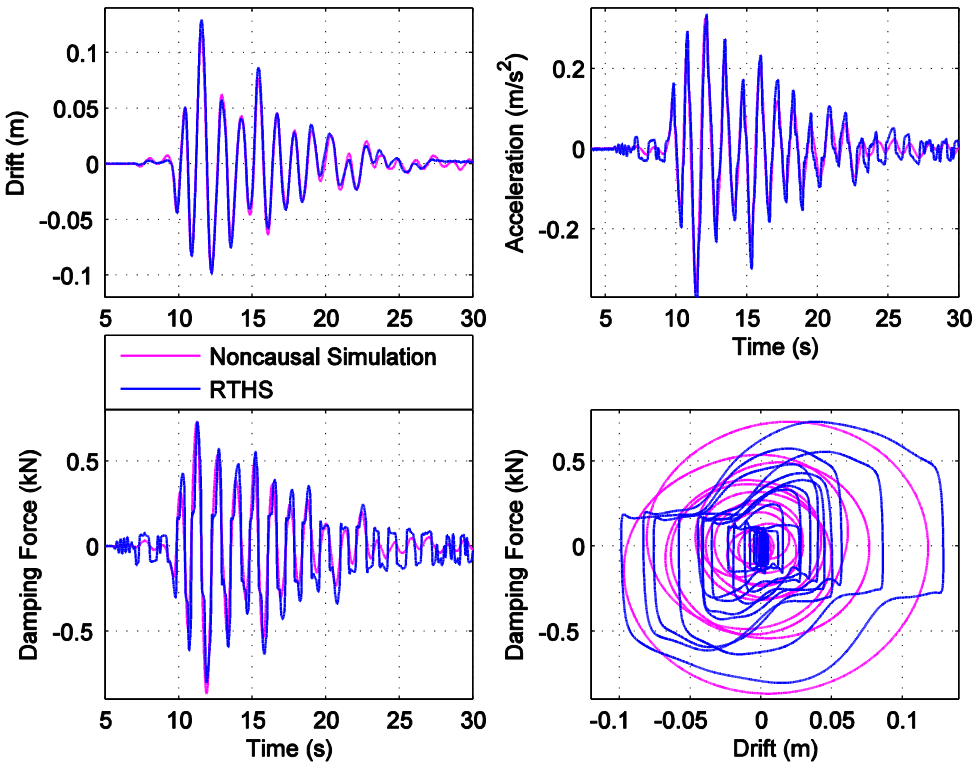

Fig. 7.6. *Non-causal RILD vs RTHS responses for 10th floor with applied 20% Kobe earthquake and natural frequency of the superstructure as an input for the all-pass filter.*

7.4.3 Comparison to Passive-on and off Controllers

This section explores the advantages of causal RILD versus other control algorithms when incorporated into inter-story isolated structures using a semi-active damper. Passive-on (constant 30 V) and passive-off (constant 0 V) cases are chosen as control alternatives for the MR damper. RTHS tests were conducted for the same prototype structure with MR damper controlled using passive-on and passive-off algorithms. The results are compared to that of causal RILD tests. Fig. 7.7 through Fig. 7.8 show seismic responses of 10th story for all three different control algorithms with applied 20% amplitude Kobe record and 10% Northridge amplitude record, respectively.

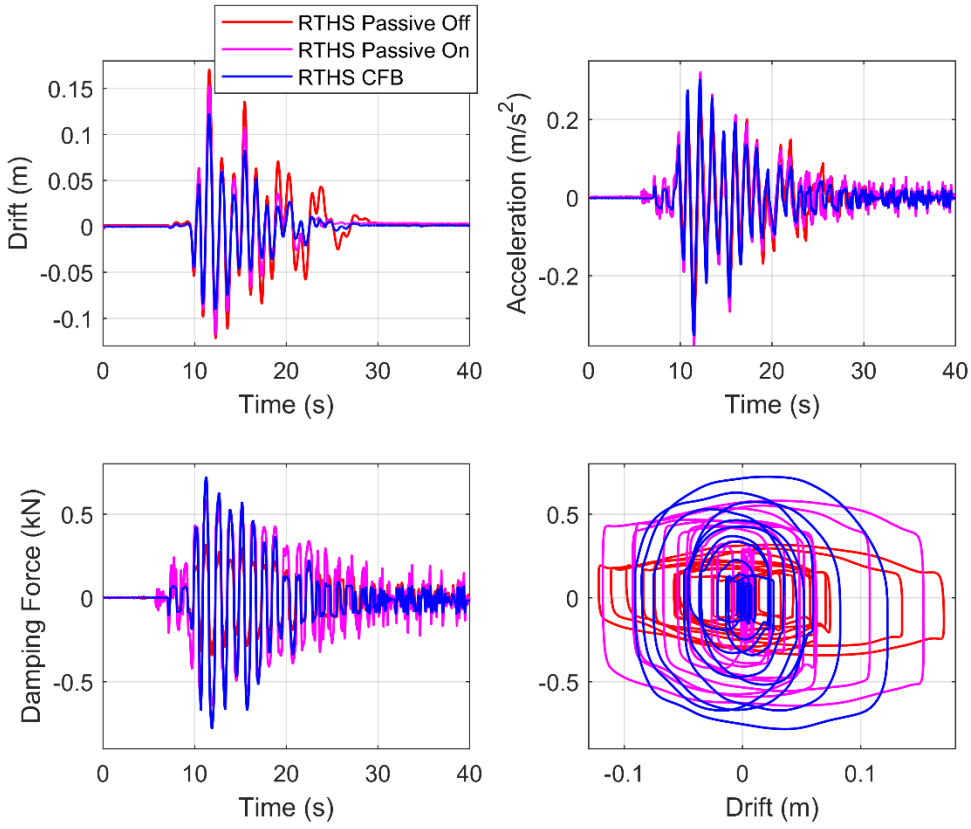

Fig. 7.7. *CFB responses vs passive-on and passive-off for 10th floor with applied 20% Kobe earthquake.*

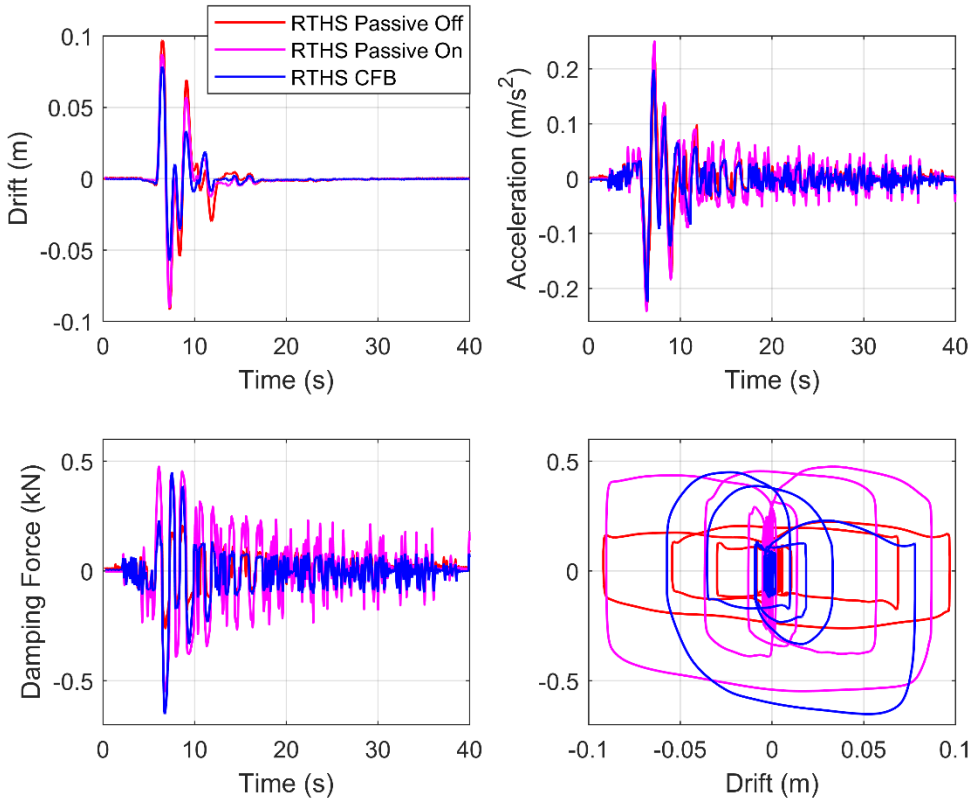

Fig. 7.8. *CFB responses vs passive-on and passive-off for 10th floor with applied 10% Northridge earthquake.*

As shown in damping force time histories of the two earthquakes, causal RILD force has slightly larger peaks than passive-on case in strong ground motion part of the earthquake. This is because voltage saturation limit for semi-active controller was set to be larger than passive-on constant 30 V. However, passive-on controller generates larger damping forces in remaining cycles. Comparing displacement and acceleration responses we can make the following conclusions: Causal RILD suppresses the displacement more effectively than both passive-on and off controller. Despite having identical or slightly larger damping force peaks, causal RILD also generates lower acceleration responses in comparison to passive-on controller for all earthquakes. This demonstrates that using a semi-active control

algorithm to track a causal realization of RILD can produce better seismic performance for inter-story isolated structures in comparison to both passive-on and off controllers.

7.4.4 Comparison to Viscous Damping

Results from RTHS tests with CFB are compared to the numerically simulated prototype structure with a discrete viscous damper installed in the isolation layer as a supplemental damping device. The viscous damping coefficient is chosen so that both of the systems have the same maximum 10^{th} story drift. This comparison is illustrated in Fig. 7.9 and Fig. 7.10 for 10^{th} floor using the two previously studied earthquake records.

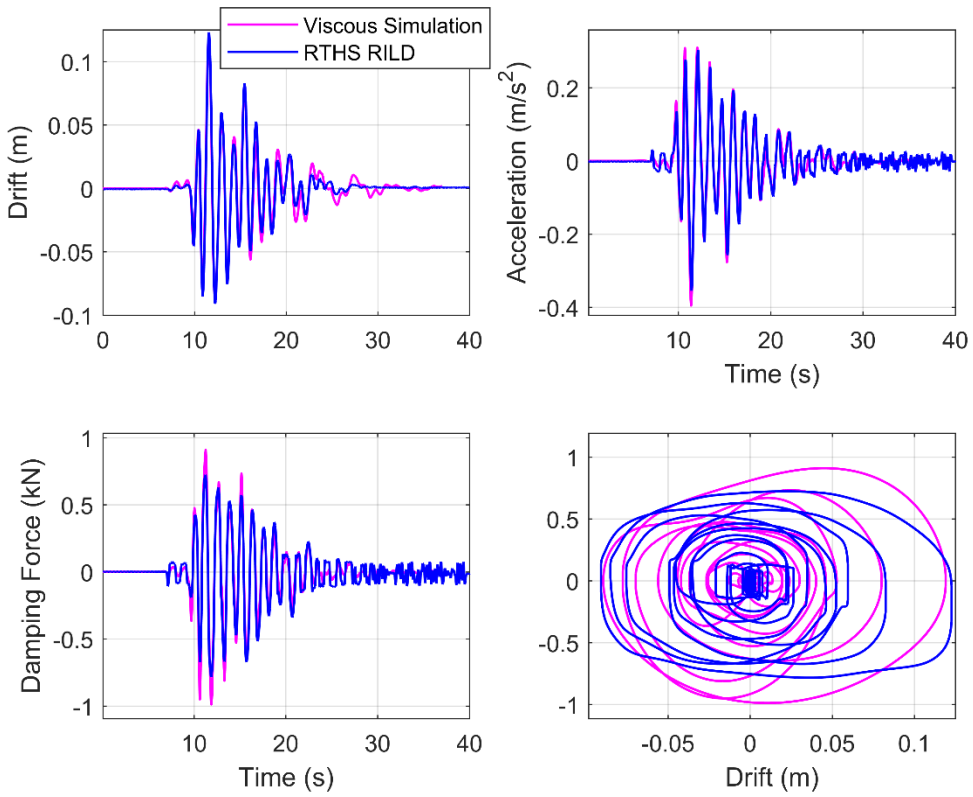

Fig. 7.9. *CFB vs viscous damping responses for 10th floor with applied 20% Kobe earthquak.*

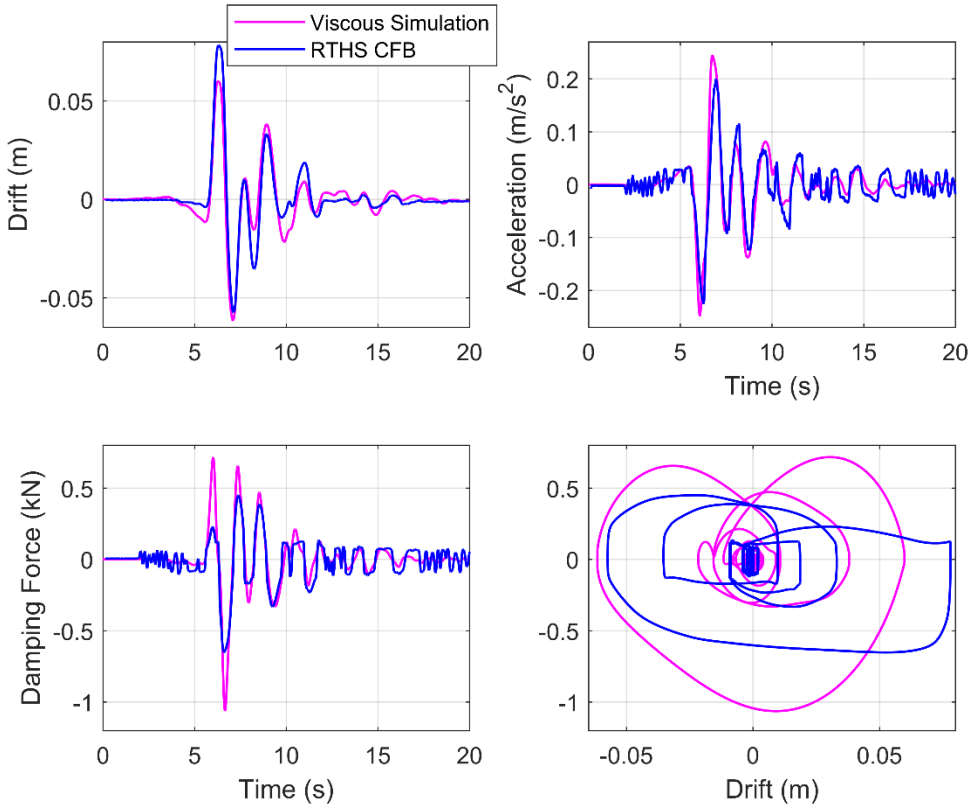

Fig. 7.10. *CFB vs viscous damping responses for 10th floor with applied 10% Northridge earthquake.*

For all the cases with the same maximum isolation layer drift, viscous damper generates higher damping forces which leads to also higher acceleration responses. In other words, CFB incorporated into inter-story isolated structure can suppress the displacement response as much as ordinary viscous dampers but with induced lower damping force which also results in lower acceleration response of the superstructure. This shows that using this semi-active controller clearly improves dynamic behavior of inter-story isolated structures when compares to traditionally discrete viscous dampers such as oil dampers that are currently being used in existing structures. These plots are also in agreement with a previous noncausal numerical study conducted by Ikago and Inoue [1].

Chapter 8: Vehicle Suspension Systems

In this chapter, a modal filter-based RILD control law is proposed for a quarter car model. This is a new type of damping that is proposed to have promising vibrational performances in vehicles that has not been used and studied before. The proposed causal filter-based approach is modified and improved by using modal coordinates for a quarter car model. The performance of the proposed control policy is then compared to skyhook and groundhook control algorithms. Results indicate that the modal causal filter-based approach (MCFB) can improve both sprung and unsprung mass responses at the same time and therefore there is no compromise for this approach unlike skyhook or groundhook controllers.

8.1 Quarter Car Semi-active Suspension System

In this section, the equations of motion of a quarter car model are presented. Then skyhook and groundhook controllers are described and damping force equations for each control law is presented.

8.1.1 Quarter Car Model

Fig. 8.1 shows a quarter car model of a vehicle. The sprung mass and unsprung mass are defined here as m_s and m_u, respectively. Suspension inherent damping is denoted as c_s and suspension spring as k_s and tire stiffness as k_t. Road profile is defined as z_r and sprung and unsprung mass displacements are defined as z_s and z_u, respectively. All displacements are absolute (relative to a ground not shown). Dots represent

derivatives with respect to time. F_d is the damping force from a semi-active device such as a MR damper.

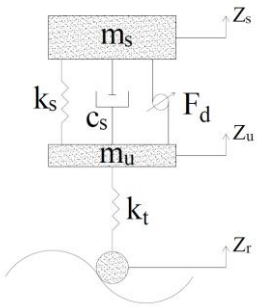

Fig. 8.1. *Quarter car model with desired semi-active force F_d.*

The equations of motion for sprung and unsprung mass of the quarter car model represented in Fig. 8.1 are as follows, respectively:

$$m_s\ddot{z}_s(t) + c_s[\dot{z}_s(t) - \dot{z}_u(t)] + k_s[z_s(t) - z_u(t)] + F_d(t) = 0 \quad (8.1)$$

$$m_u\ddot{z}_u(t) + c_s[\dot{z}_u(t) - \dot{z}_s(t)] + k_s[z_u(t) - z_s(t)] + k_t[z_u(t) - z_r(t)] = F_d(t) \quad (8.2)$$

As mentioned earlier $F_d(t)$ is a force achieved from a semi-active control algorithm. These equations are used in this study to form the state space matrices required for numerical simulations in later sections.

Table 8.1 show properties of the quarter car model used in this chapter for all the numerical simulations.

Table 8.1. Parameters of the 2-DOF Quarter Car Model.

Quarter Car Model Properties	
m_s	373.5 *kg*
m_u	40 *kg*
c_s	570 *Ns/m*
k_s	27358 *N/m*
k_t	211625 *N/m*

It is worthwhile to mention that reducing sprung mass responses will result in better ride quality of the vehicle while reducing unsprung mass responses leads to a better road holding ability [38].

8.1.2 Skyhook Control

In ideal skyhook control, the sprung mass of the quarter car model is linked to some fictional fixed point in sky via a damper as shown in Fig. 8.2. The goal of skyhook controller is to isolate vibrations of the sprung mass. The equations describing a common implementation of skyhook control for semi-active dampers (e.g., Fig. 8.1) are as follows:

$$\begin{cases} F_{D,sky} = c_{sky}\dot{z}_s & \dot{z}_s(\dot{z}_s - \dot{z}_u) \geq 0 \\ F_{D,sky} = 0 & \dot{z}_s(\dot{z}_s - \dot{z}_u) < 0 \end{cases} \tag{8.3}$$

where $(\dot{z}_s - \dot{z}_u)$ is the relative velocity of the sprung mass with respect to the unsprung mass. As discussed earlier, according to Equation (8.3), skyhook control law is designed to mitigate sprung mass responses at the expense of increase in unsprung mass responses.

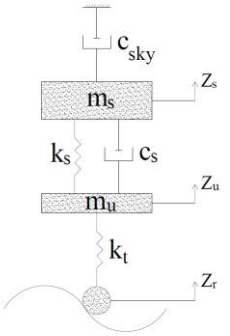

Fig. 8.2. *Ideal Skyhook control.*

8.1.3 Groundhook Control

In a common implementation of groundhook control for semi-active dampers (e.g., Fig. 8.1), the desired damping force is defined as:

$$\begin{cases} F_{D,gnd} = c_{gnd}\dot{z}_u & -\dot{z}_u(\dot{z}_s - \dot{z}_u) \geq 0 \\ F_{D,gnd} = 0 & -\dot{z}_u(\dot{z}_s - \dot{z}_u) < 0 \end{cases} \tag{8.4}$$

Equation (8.4) is based on ideal groundhook controller in which a the damper is linked to the unsprung mass at one end and connected to ground at the other end which results in a reduction in unsprung mass responses at the expense of sprung mass responses. Fig. 8.3 represents ideal groundhook control in quarter car model.

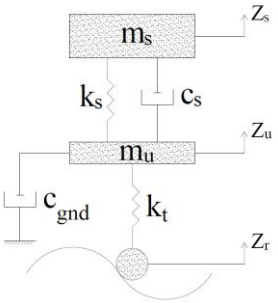

Fig. 8.3. *Ideal Groundhook control.*

8.2 Proposed Modal Causal Filter-based Approach (MCFB)

In MCFB method, first mode shapes and corresponding modal frequencies of a vehicle are computed through eigenvalue analysis. Using achieved mode shapes, modal coordinates of the corresponding vehicle are obtained as following:

$$\begin{Bmatrix} p_1(t) \\ p_2(t) \end{Bmatrix} = [\Phi]^T_{2\times 2} \begin{Bmatrix} z_s(t)-z_r(t) \\ z_u(t)-z_r(t) \end{Bmatrix} \tag{8.5}$$

where $p_1(t)$ and $p_2(t)$ are modal coordinates for first and second modes. In practice, both sprung and unsprung relative displacement can be estimated accurately using a Kalman filter algorithm. The only measurement required is the sprung mass absolute acceleration which can be measured using an accelerometer and therefore is a great benefit for practical applications. Similar applications of Kalman filters in vehicle suspension system can be found in [57, 58]. Matrix $[\Phi]_{2\times 2}$ is the eigenvector matrix whose first column is the first mode shape and second column is the second mode shape. After obtaining $P_1(\omega)$ and $P_2(\omega)$ using Fourier transform, the next step is to calculate modal causal RILD force in frequency domain as follows:

$$F_{D,1}(\omega) = k_s\eta(\varphi_{11} - \varphi_{21})P_1(\omega)\frac{i\omega-\omega_1}{i\omega+\omega_1} \tag{8.6}$$

$$F_{D,2}(\omega) = k_s\eta(\varphi_{12} - \varphi_{22})P_2(\omega)\frac{i\omega-\omega_2}{i\omega+\omega_2} \tag{8.7}$$

in which $F_{D,1}(\omega)$ and $F_{D,2}(\omega)$ are modal causal RILD force for first and second modes, respectively. ω_1 and ω_2 are first and second modal frequencies and φ_{ij} is the i^{th} DOF of the j^{th} mode of the mode shape vector. The total MCFB damping force is the summation of the modal forces shown here as [59]:

$$F_{D,MCFB}(\omega) = \alpha F_{D,1}(\omega) + \beta F_{D,2}(\omega) \tag{8.8}$$

where α and β are the weight factors for first and second modes, respectively. If mode shapes are mass normalized, then $\alpha = m_s$ and $\beta = m_u$. The procedure from Equation (8.5) through Equation (8.8) is conducted in real time in a feedback loop with the sprung and unsprung response displacement as the input measurements and MCFB damping force as the output desired force. Then an active or semi-active control device such as MR damper can be used to track that desired force. Please note, although whole process is conducted in time domain in a numerical simulation, Equation (8.6) through Equation (8.8) are presented here in frequency domain for better understanding of the control force.

8.3 Numerical Comparison of MCFB, CFB, and RILD models

In this section, the two causal approximations of RILD (CFB and MCFB) are compared to RILD for a quarter car model. The purpose of this section is to demonstrate the ability to match (non-causal) RILD with causal algorithms. A comparison to other control methods will follow in the next section. The properties of the model are presented in Table 8.1 [60].

Non-causal numerical analysis can be conducted in both time and frequency domains [39, 40]. For linear MDOF systems frequency domain analysis is the most straightforward approach to solve for noncausal responses [43]. Hence, in this dissertation, RILD responses are calculated through frequency domain method. Both CFB and MCFB algorithms were analyzed in the time domain using MATLAB's SIMULINK environment.

8.3.1 Band-limited White Noise Road Profile

Fig. 8.4 shows time history responses of the quarter car model to the input white noise. To clearly show the different performances of CFB and MCFB approaches in comparison to (non-causal) RILD responses, zoomed view of the time history results are presented, since the comparative performance of the three models is the same for different time periods. The abscissa for sprung displacement is scaled differently than the other plots in this figure due to the lower frequency nature of this signal as compared to other time history plots. As a result, a portion of one second is chosen in z_s plot (by vertical dashed line), where other time history responses are plotted for that range as shown in Fig. 8.4. The η value is chosen to be 0.6 for all models.

Moreover, please note that sprung and unsprung accelerations ($\ddot{z}_s \; and \; \ddot{z}_u$), are shown as A_s and A_u in all the time history plots throughout the paper. As also noted earlier, all sprung and unsprung displacements are absolute values relative to the ground.

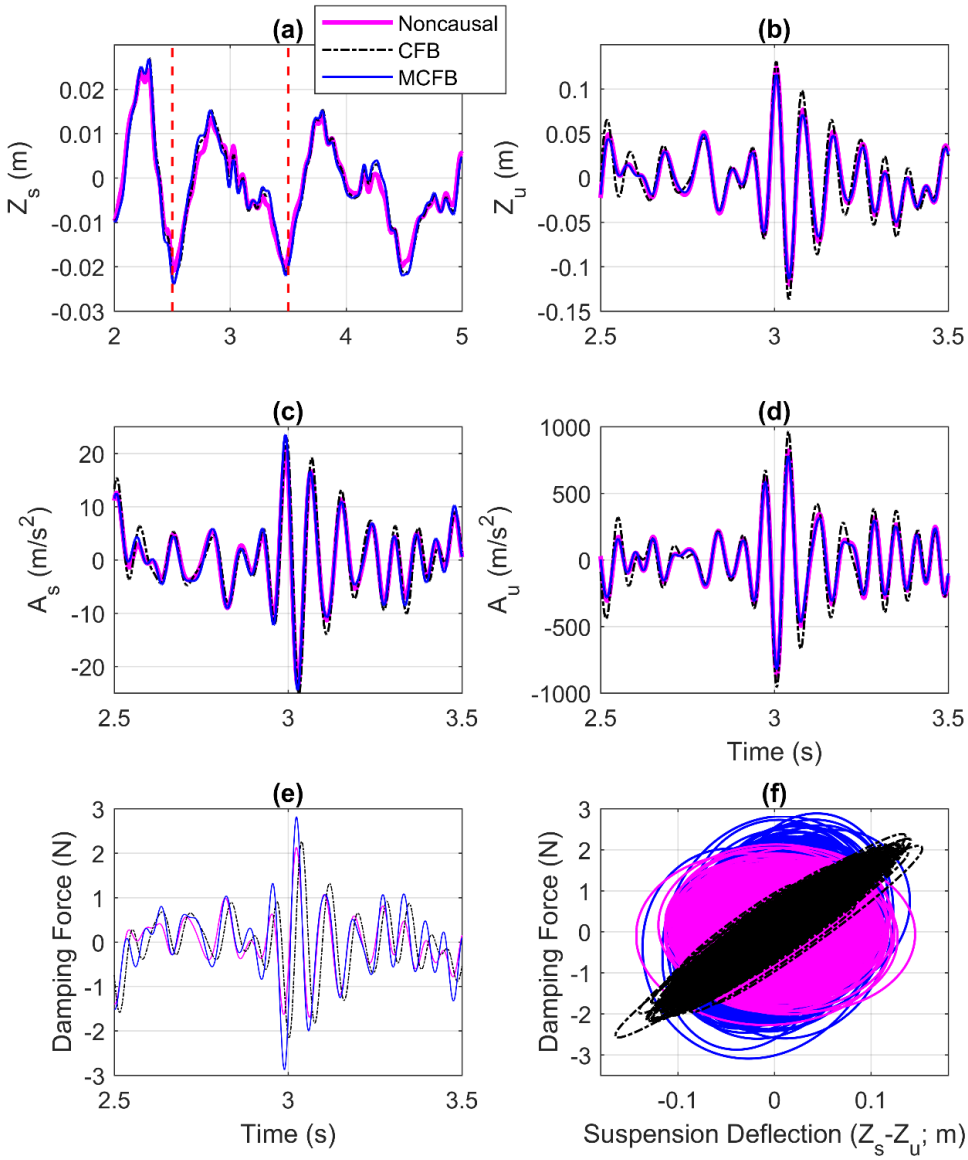

Fig. 8.4. *Time history comparison of noncausal (RILD), CFB, and MCFB models with white noise input: (a) z_s, (b) z_u, (c) A_s, (d) A_u, (e) Damping Force, and (f) Hysteresis.*

As shown in Fig. 8.4, MCFB method can clearly better track the noncausal responses when compared to CFB approach. From the time history plot of sprung mass displacement, z_s, it can be drawn that the two methods are almost overlapping and have a same behavior. However, when it comes to the other responses of

unsprung displacement (z_u), sprung and unsprung accelerations (A_s and A_u), it is evident that MCFB control does a better job than CFB algorithm in matching the RILD responses. Moreover, considering the time history and hysteresis plots of damping force, it is perfectly shown that MCFB approach is almost completely in phase with RILD, whereas, the CFB control is clearly out of phase, resulting in a positively skewed hysteresis.

It is worthwhile to mention that unsprung mass displacement of the vehicle suspension system for all the models is relatively large while applying a white noise input as shown in Fig. 8.4. This is due to the fact that, white noise input excites both modes of the suspension system equally and leads to resonance at the second mode which will results in an amplified unsprung mass displacement for all the models as compared to the white noise input. This is also clearly shown in transmissibility plots of the suspension system later in section 8.4.1. Responses are more realistic for the ISO random road profile investigated next.

8.3.2 ISO Road Profile

To further investigate the effectiveness of the MCFB control law, the quarter car model is subjected to a random road profile as discussed in section 3.6. Fig. 8.5 represents simulation results comparing RILD, CFB and MCFB models for the random road profile shown in Fig. 8.5 for the vehicle speed of 120 *km/hr*. Similar to white noise responses, both acceleration responses and damping force time history signal are plotted here in zoomed view due to their high frequency vibrations. So that the reader can clearly see the different vibration performance of all the models. Similarly, a small portion is chosen in Z_s and Z_u plots (by vertical dashed line),

where other time history responses are plotted for that range as shown in Fig. 8.5. The zoomed view represents general performance of the three models in all time ranges.

As shown in Fig. 8.5, both causal approaches have almost identical performances in tracking RILD model for sprung and unsprung mass displacements (Z_s and Z_u), and sprung acceleration, A_s. However, CFB method resulted in higher unsprung acceleration than both MCFB approach and RILD model. Furthermore, damping force time history signal and also hysteresis plot clearly show the advantage of MCFB model over CFB control in matching RILD. It is drawn from the hysteresis plot that the MCFB control algorithm is very much in phase with RILD in that both have the oval shape hysteresis with little skew, whereas the CFB model generates a positively skewed hysteresis.

Fig. 8.6 illustrates the hysteresis plots for four different random road profiles with the vehicle speed of 50, 80, 100, and 140 *km/hr*. Similarly, same conclusions can be made as in Fig. 8.5 for both low and high vehicle speeds. CFB algorithm creates a positively skewed hysteresis which results in higher unsprung mass acceleration as compared to RILD model and MCFB controller.. To summarize, it can be concluded that MCFB control law can better track RILD responses and is very much in phase with RILD model than the CFB approach.

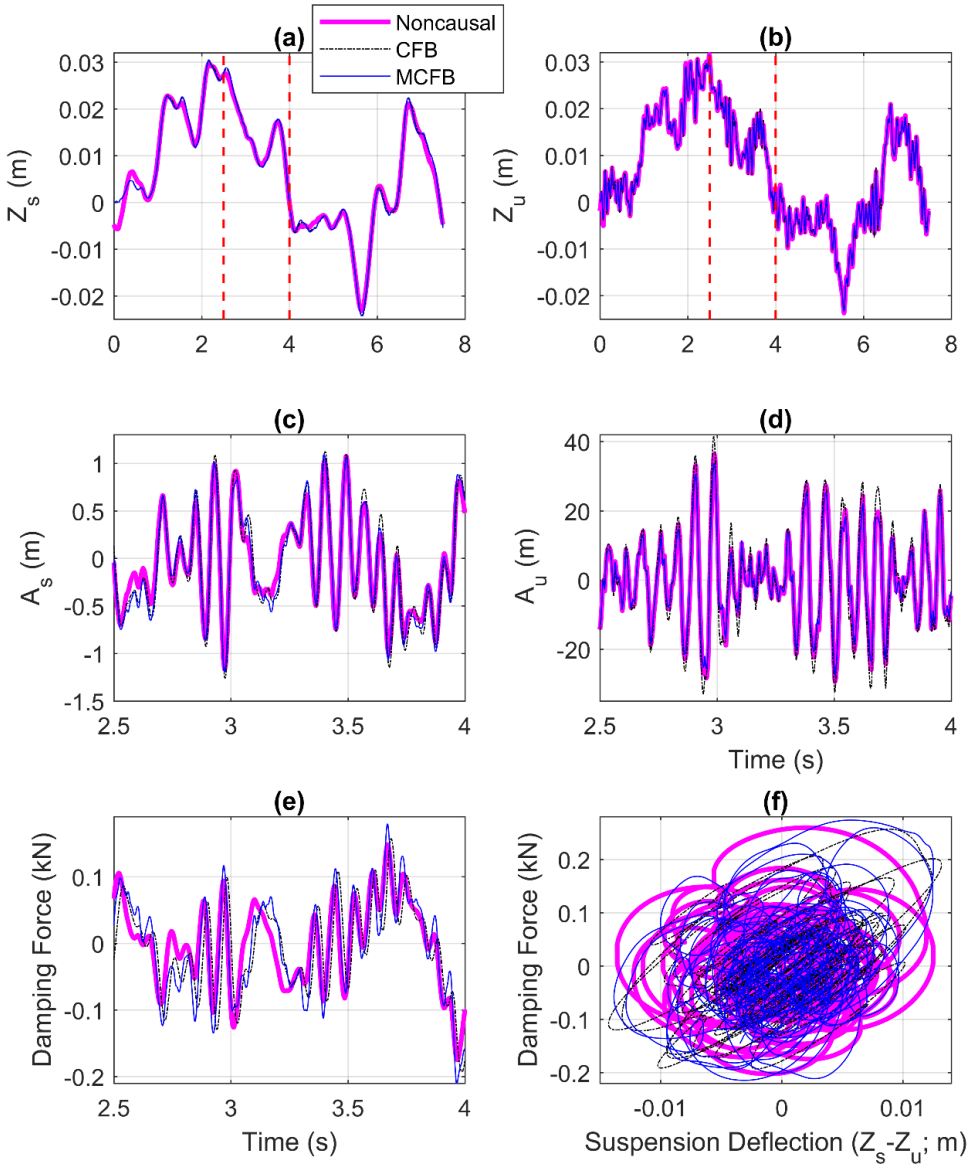

Fig. 8.5. *Time history comparison of noncausal, CFB and MCFB models with random road profile input.*

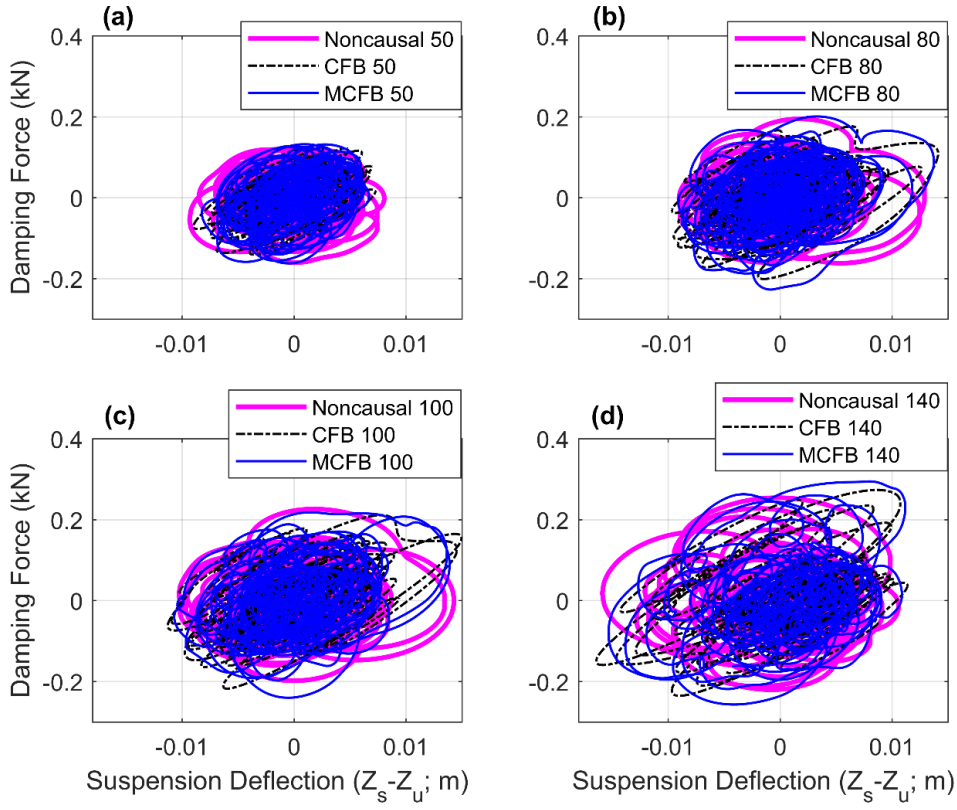

Fig. 8.6. *Hysteresis plots for the vehicle speed of 50, 80, 100 and 140 km/hr.*

8.4 Numerical Comparison of MCFB, Skyhook, and Groundhook models

In this section, the merits of using MCFB control in comparison to skyhook and groundhook controllers are discussed. Similar to section 8.3, both white noise and random road profile are considered here as an input to the quarter car model. For MCFB controller η value is chosen to be 0.6 for all simulations. For this comparison, it is worth noting that force-velocity relationship of the MCFB algorithm (Equation (8.8)) was not restricted to the first and third quadrants in Cartesian coordinates. This restriction was imposed on the skyhook and groundhook controllers as per their classical definitions (Equation (8.3) and (8.4)). For the MCFB controller, this

restriction had a negligible influence on the results, i.e., results were nearly identical with or without it.

8.4.1 Band-limited White Noise Road Profile

As noted earlier, skyhook control policy is to mitigate sprung mass responses while groundhook control policy is designed to decrease unsprung mass responses. Therefore, skyhook and groundhook damping coefficients (i.e. c_{sky} and c_{gnd}) are computed so that both MCFB and skyhook models have the same maximum sprung mass displacement, z_s and MCFB and groundhook controllers have the same maximum unsprung mass displacement, z_u, respectively. The controller designs are η = 0.6, c_{sky} = 1650 Ns/m, and c_{gnd} = 300 Ns/m for the MCFB, skyhook, and groundhook controllers, respectively.

As discussed in Section 3.6, transmissibility is defined as the ratio of the sprung or unsprung mass responses to input road profile. Fig. 8.7 compares transmissibility plots of a quarter car model with the three different controllers as well as to an uncontrolled system.

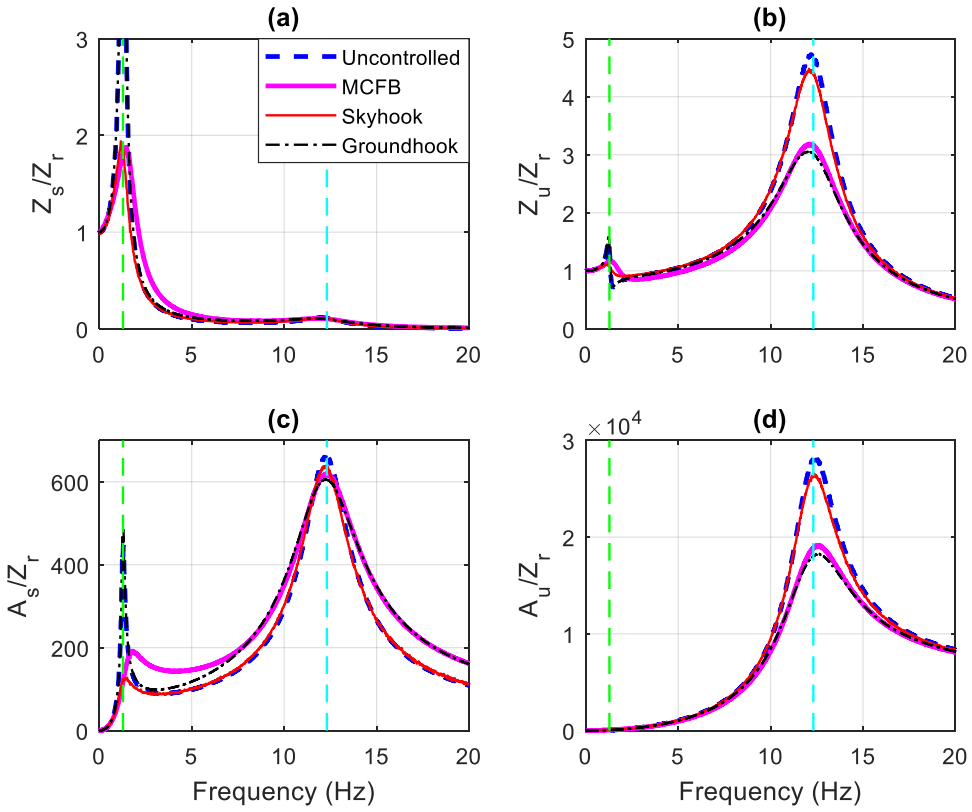

Fig. 8.7. *Transmissibility plots of uncontrolled, MCFB, skyhook and groundhook controllers for: (a) z_s, (b) z_u, (c) A_s, and (d) A_u.*

The vertical dashed lines in Fig. 8.7 represents first and second modal frequencies of the vehicle. As it is shown in Fig. 8.7, while MCFB and skyhook models are set to have identical maximum sprung mass displacement, skyhook controller has higher peak in unsprung mass displacement transmissibility. Furthermore, skyhook control has slightly smaller first mode sprung acceleration transmissibility than MCFB algorithm while both have almost a same second mode peak. Finally, MCFB has lower unsprung mass acceleration transmissibility peak than skyhook algorithm. To summarize, the MCFB controller attenuates unsprung mass transmissibility curves much better than skyhook controller, while at the same time it

can improve vibrational responses of the sprung mass almost as good as skyhook controller.

On the other hand, groundhook algorithm has much higher sprung mass displacement and acceleration transmissibility peaks than MCFB model and slightly smaller unsprung mass acceleration and displacement peaks. Again, this shows that MCFB control is able to mitigate sprung mass responses much better than groundhook control law, while delivering almost identical unsprung mass responses as groundhook controller. Fig. 8.7 also shows transmissibility plots of an uncontrolled quarter car model. It is clearly shown that the MCFB controller improve performance of the system for both sprung and unsprung masses, while the skyhook and groundhook controllers can only improve performance of sprung and unsprung mass, respectively. It is worthwhile to mention that the fluctuation in unsprung mass displacement for groundhook controller is due to the presence of a complex-conjugate pair of zeros in the groundhook transfer function, close to fundamental natural frequency of the system.

In conclusion, while skyhook and groundhook controllers are designed to attenuate sprung and unsprung mass responses at the expense of increase in responses of the other mass, MCFB control algorithm can nearly improve vibrational performances of both masses at the same time. Hence, unlike skyhook and ground hook controllers there is no compromise for this approach.

Fig. 8.8 depicts bar plots of maximum and Root Mean Square (RMS) values of the time history responses for the quarter car model subjected to a white noise road

profile.

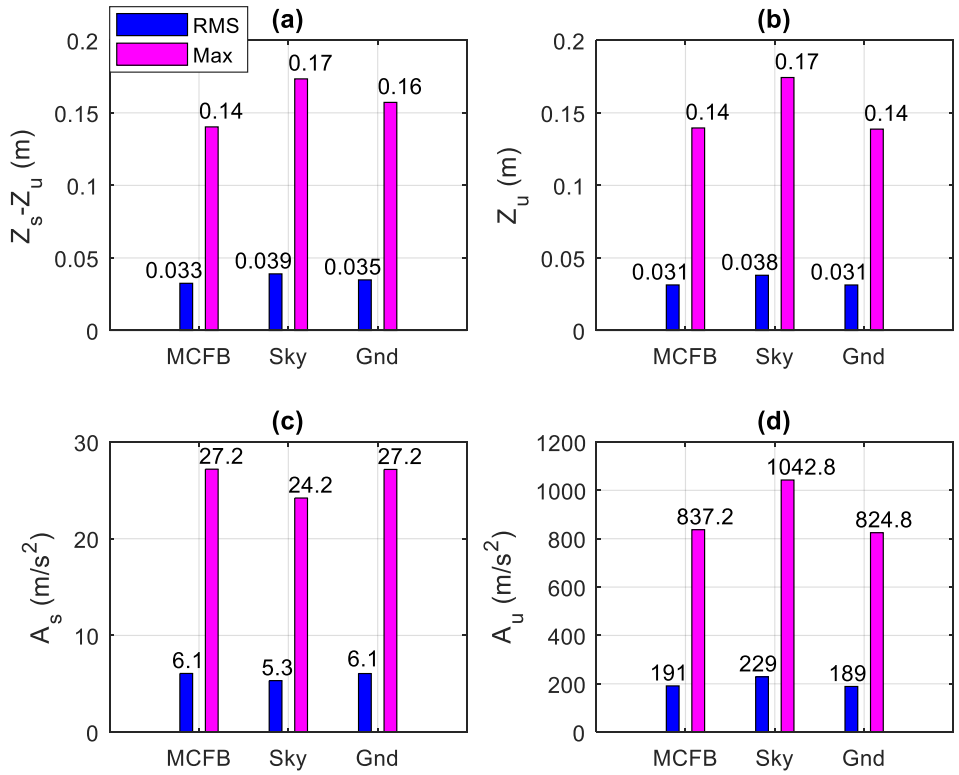

Fig. 8.8. *Maximum and RMS comparison of MCFB, skyhook and groundhook controllers for white noise input: (a) $z_s - z_u$, (b) z_u, (c) A_s, and (d) A_u.*

Fig. 8.8 confirms the conclusions made earlier in this section. As noted earlier, MCFB and skyhook control are set to have identical maximum sprung displacement and MCFB and groundhook to have identical maximum unsprung displacement. However, MCFB approach has the lowest peak suspension deflection, $(z_s - z_u)$ (i.e. the sprung mass displacement relative to the unsprung mass). This will contribute to better road ride quality. Skyhook model results in the lowest sprung acceleration as expected; while, MCFB and groundhook lead to similar maximum and RMS sprung acceleration. Groundhook control causes lowest unsprung mass acceleration and

MCFB algorithm also mitigate unsprung mass acceleration almost as much as groundhook controller which is in agreement with the transmissibility curve data.

8.4.2 ISO Road Profile

Same criteria is used here to calculate damping coefficients of skyhook and groundhook controllers as in section 8.4.1. Fig. 8.9 shows time history responses of quarter car model with applied random road profile and vehicle speed of 120 *km/hr* (See Fig. 3.4). Similar scaling procedure is done to clearly demonstrate high frequency vibrations of accelerations and damping force time history plots.

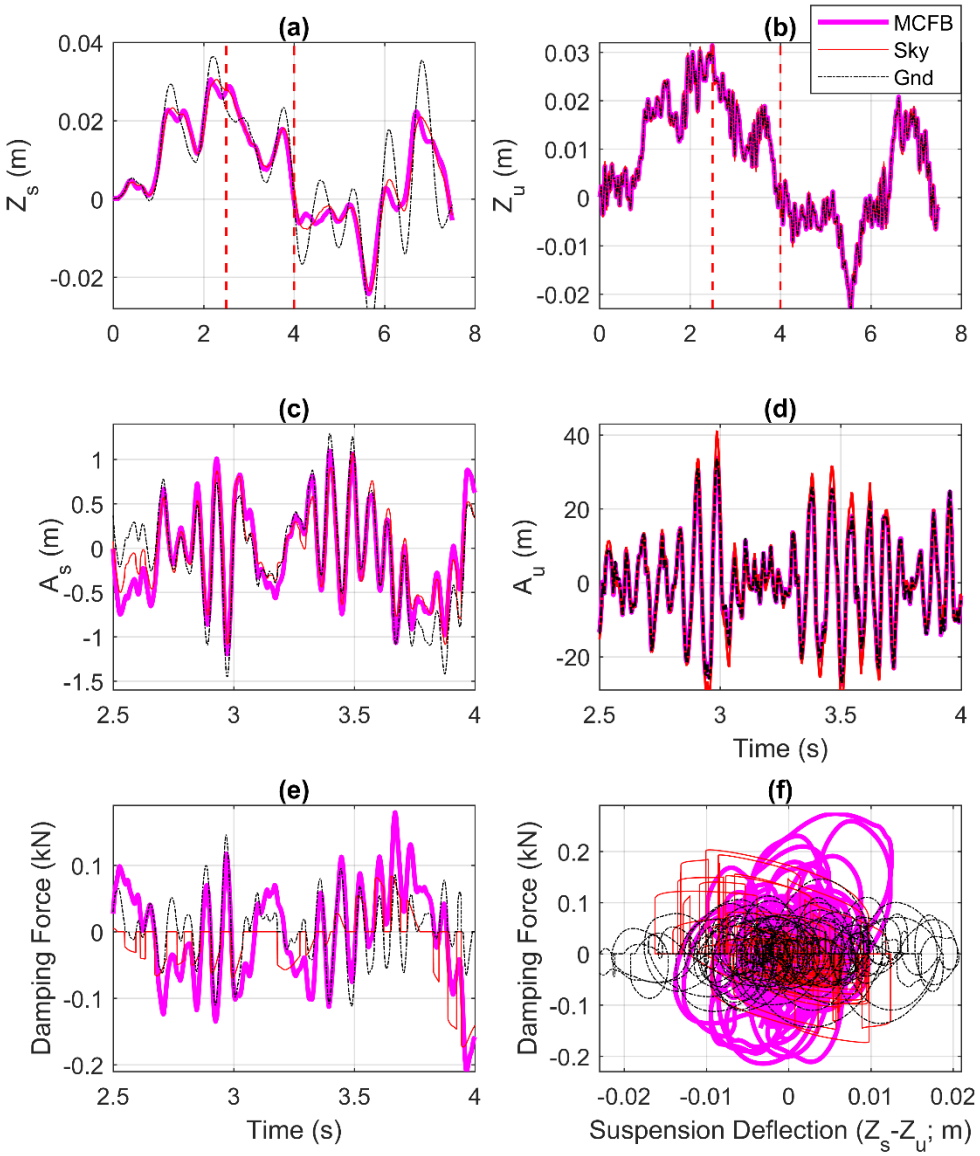

Fig. 8.9. *Time history comparison of MCFB, skyhook and groundhook controllers for random road profile input: (a) z_s, (b) z_u, (c) A_s, (d) A_u, (e) Damping Force, and (f) Hysteresis.*

As illustrated in Fig. 8.9, skyhook and MCFB control law results in almost identical sprung displacement, which is lower than groundhook algorithm. For this road profile, all controllers have similar unsprung mass displacement. Moreover, as expected, skyhook and groundhook controllers cause highest peak in unsprung and

sprung mass accelerations, respectively. Similar to white noise responses, MCFB method attenuates both sprung and unsprung mass accelerations nearly as much as skyhook and groundhook algorithm, respectively.

Maximum and RMS values of the time history responses for the quarter car model subjected to a random road profile presented in Fig. 3.4 is shown in Fig. 8.10 for the vehicle speed of 50 *km/hr*.

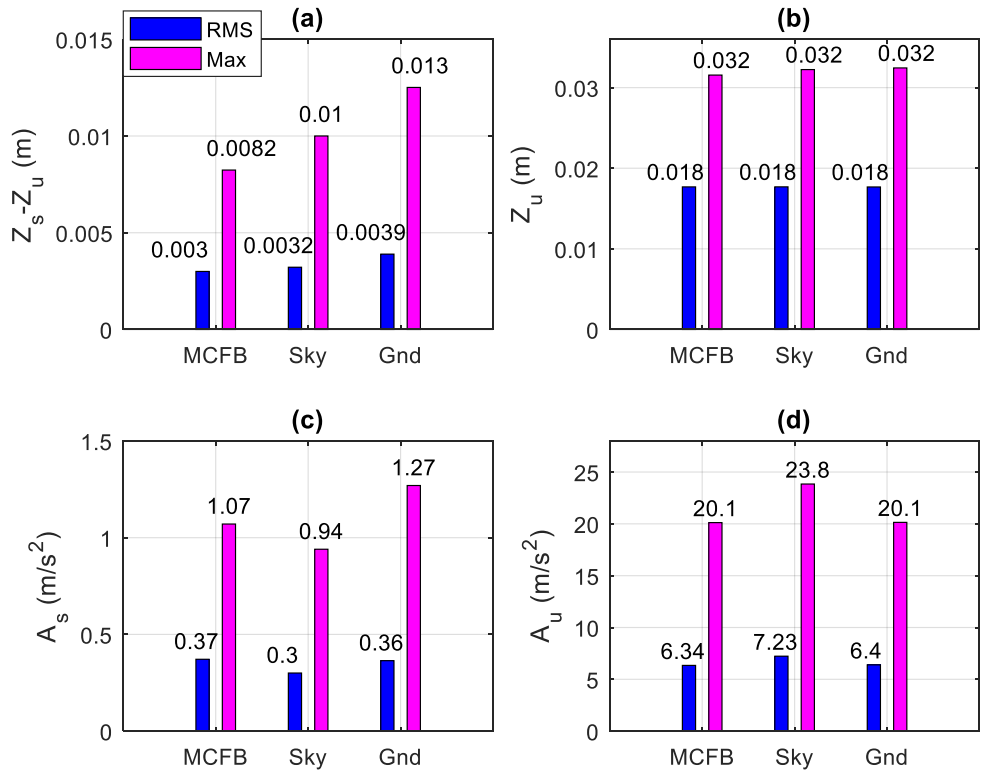

Fig. 8.10. *Maximum and RMS comparison of MCFB, skyhook and groundhook controllers for random road profile input with speed of 50 km/hr: (a) $z_s - z_u$, (b) z_u, (c) A_s, and (d) A_u.*

Likewise, same conclusions can be made here as from Fig. 8.8. MCFB has the lowest suspension deflection, $(z_s - z_u)$. While skyhook and groundhook algorithm can only mitigate responses of one of the masses at the expense of the other mass,

MCFB approach is able to improve vibrational performance of both sprung and unsprung masses at the same time.

Fig. 8.11 shows Maximum and RMS values of the quarter car model subjected to a random road profile presented in Fig. 3.4 for the vehicle speed of 120 *km/hr*.

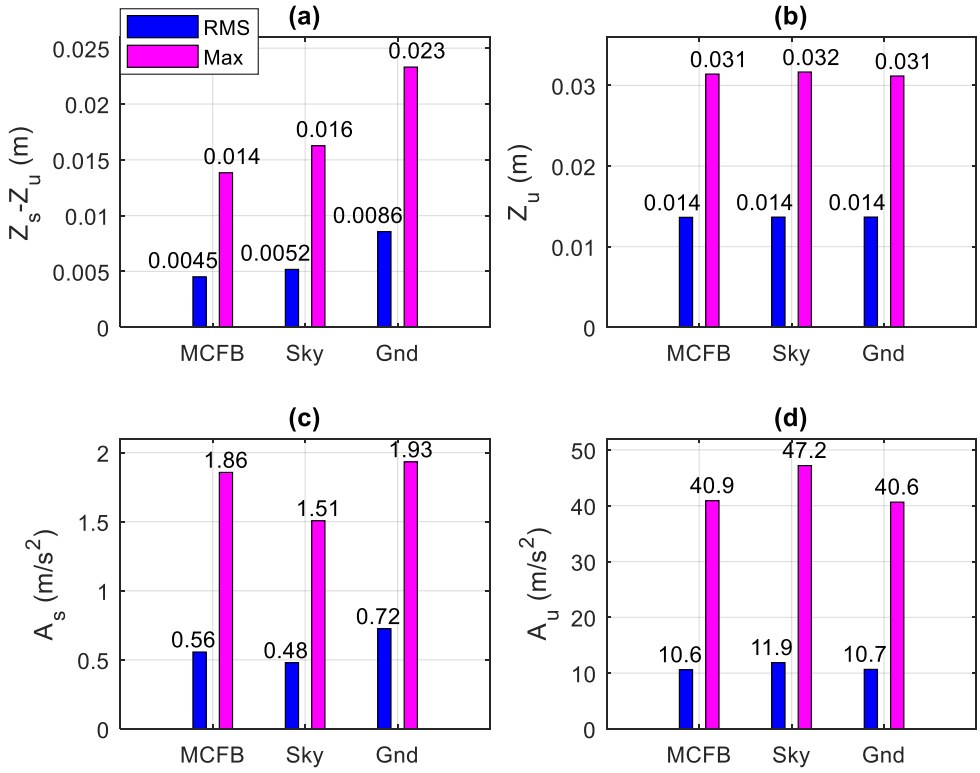

Fig. 8.11. *Maximum and RMS comparison of MCFB, skyhook and groundhook controllers for random road profile input with speed of 120 km/hr: (a) $z_s - z_u$, (b) z_u, (c) A_s, and (d) A_u.*

The same behavior is observed for vehicle speed of 120 km/hr. This demonstrates that MCFB algorithm works well at both low and high velocities.

In conclusion, unlike skyhook and groundhook controllers, there is no comprise for MCFB approach. Therefore, this semi-active model can enhance both sprung and unsprung responses of the vehicle simultaneously. Moreover, as discussed

earlier the only measurement needed to implement the MCFB algorithm is the sprung mass absolute acceleration which can be easily measured using local sensors and thus is a great benefit for practical applications. It is worthwhile to mention that since skyhook and groundhook control forces are proportional to absolute velocity of sprung and unsprung mass respectively, practical implementation of these controllers is more challenging in a sense that it requires more measurements for accurate estimation and therefore more sensors.

8.4.3 Controller robustness study under ISO road profile

To investigate the robustness of the MCFB, skyhook, and groundhook controllers, their performances are evaluated for changes in the sprung mass m_s, simulating the condition where the occupancy or payload of the vehicle changes. The controller parameters for all three controllers are identical to section 8.4.1 and 8.4.2, i.e., they are not updated to accommodate the change in m_s. Fig. 8.12 and Fig. 8.13 compare the maximum and RMS vehicle responses, respectively, for these three controllers as m_s is varied. Each point represents a simulation with the ISO road profile and vehicle speed of 120 *km/hr*. The vertical dashed lines indicate the original m_s value from Table 8.1. A range of $0.25m_s$ to $2m_s$ is investigated in this study.

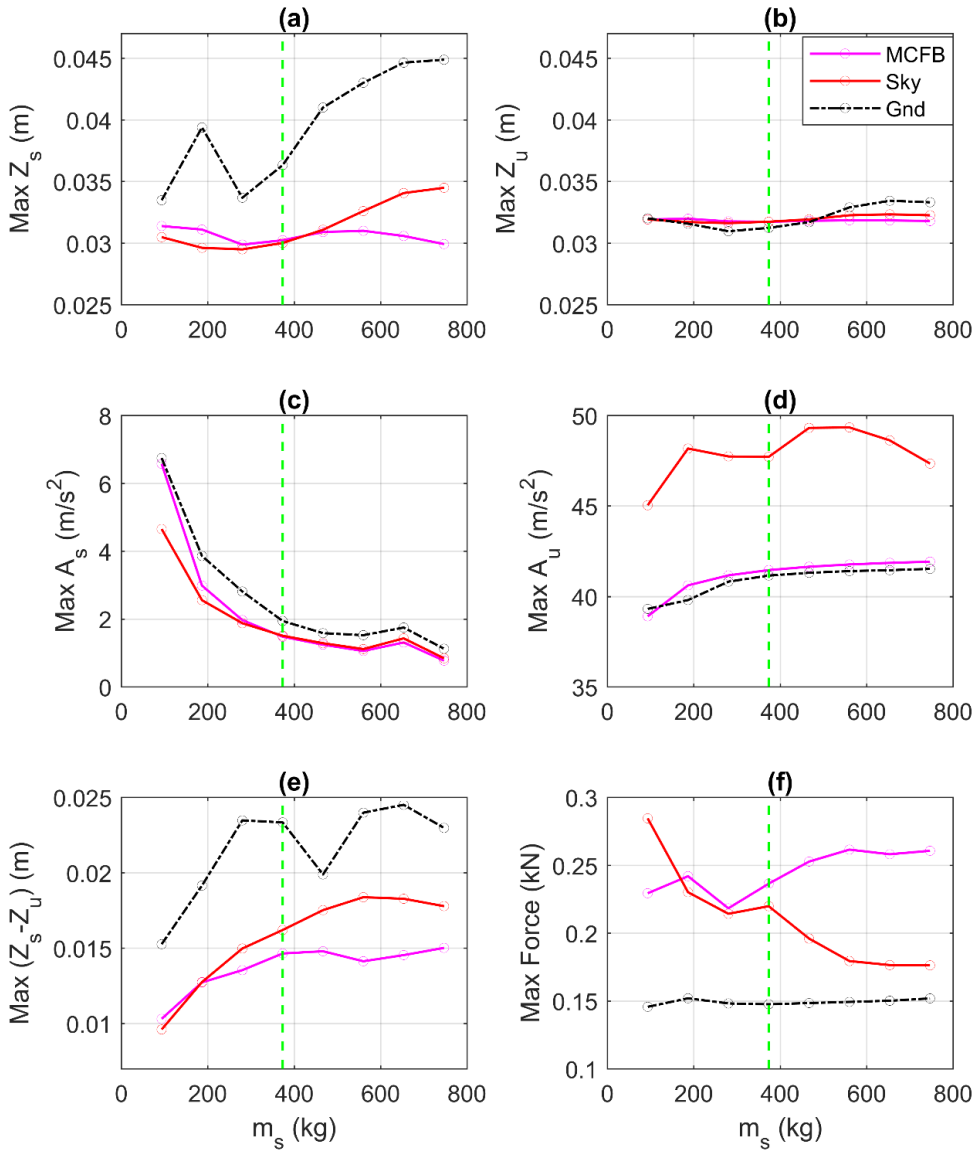

Fig. 8.12. *Peak response comparison of MCFB, skyhook and groundhook controllers for various m_s values with vehicle speed of 120 km/hr: (a) z_s, (b) z_u, (c) A_s, (d) A_u, (e) $z_s - z_u$, and (f) damping force.*

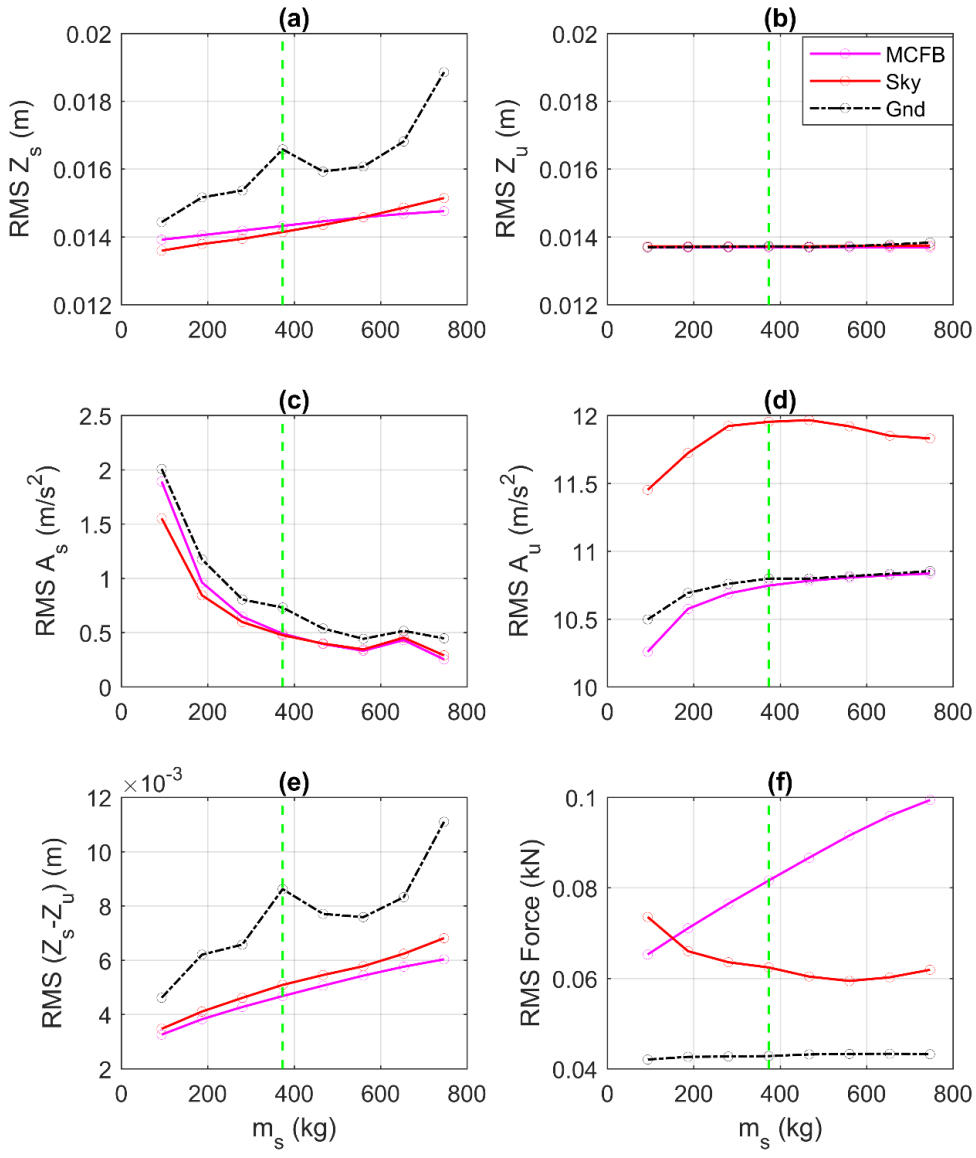

Fig. 8.13. *RMS response comparison of MCFB, skyhook and groundhook controllers for various m_s values with vehicle speed of 120 km/hr: (a) z_s, (b) z_u, (c) A_s, (d) A_u, (e) $z_s - z_u$, and (f) damping force.*

Looking at Fig. 8.12 and Fig. 8.13, the MCFB is the most effective at reducing displacement and acceleration responses of both sprung and unsprung masses, even as the sprung mass m_s varies. For the road profile and speed considered, the MCFB is arguably the most robust of the three controllers. The tradeoffs in

mitigating sprung and unsprung mass responses are clear in the skyhook and groundhook controllers. However, even as m_s varies, the MCFB controller mitigates sprung mass and unsprung mass responses as effectively as skyhook and groundhook controllers, respectively. Suspension deflection is also maintained at its lowest levels through the MCFB controller. The robust performance of the MCFB controller comes at the expense of larger damping forces with increasing m_s. To summarize, as the occupancy or payload of the vehicle changes, the MCFB controller has a clear advantage over both skyhook and groundhook controllers.

Chapter 9: Adaptive Causal Realization of RILD

The proposed CFB approach (as presented in Chapter 5) to approximate ideal RILD is accurate at a prescribed frequency, set as the fundamental natural frequency of the structure. The CFB approach is well-suited as a basis for an adaptive algorithm whereby the filter frequency can be updated in real-time based on the actual structural responses.

In this chapter, two adaptive controllers are proposed to approximate ideal RILD based on the dominant response frequency estimated in real-time and to the CFB model. By estimating the response frequency, the displacement phase advance of $\pi/2$ radians is more accurately applied. The desired damping force is then tracked by a semi-active damper, which is naturally in phase with velocity and has a controllable magnitude.

The adaptive control approaches are demonstrated through RTHS of a 5-story base-isolated structure and a 14-story inter-story isolated building. A magnetorheological (MR) damper is added to the isolation layer of each structure to provide supplemental control mimicking ideal RILD. The MR damper is experimentally represented while the remainder of the structure is numerically simulated in the RTHS loop. The desired damping force is tracked by the semi-active damper. The results compare well to noncausal numerical simulations in both damping forces and structural responses. Results also show clear improved seismic performance of the adaptive algorithms as compared to non-adaptive causal

approximations and passive-on and off damper controllers (e.g., nonlinear hysteretic damping).

9.1 Need for an Adaptive Algorithm

As discussed in Chapters 6 and 7, an all-pass filter can be used to approximate the target filter of Equation (5.12), as a causal approach to mimic ideal RILD. The all-pass filter of CFB controller can take the form of:

$$H_{CFB}(\omega) = \eta k \frac{i\omega - \omega_f}{i\omega + \omega_f} \tag{9.1}$$

where ω_f is the frequency in which $H_{\mathrm{CFB}}(\omega)$ has an exact π/2 radian (90°) phase advance.

The CFB approach requires the selection of a frequency ω_f, which should match the response frequency of the structure under earthquake excitation. The CFB approach is applied in this chapter to both base-isolated and inter-story isolated structures. For a base-isolated structure, the best estimate of the response frequency is the fundamental natural frequency of the structure. As concluded from Chapter 7, for an inter-story isolated structure, there are two obvious choices: the fundamental natural frequency of (1) the substructure and (2) the superstructure including the isolation layer. The former results in better strong-motion responses because the substructure essentially filters the ground motion and provide a narrow band excitation to the superstructure. The latter leads to better free vibration responses once the excitation has passed. Since the strong ground motion part of the earthquake is more important for design, the fundamental natural frequency of the substructure is

chosen for fixed-frequency (non-adaptive) CFB models for inter-story isolated structures.

As mentioned in Section 5.4, if the response of a structure is dominated by a different frequency, e.g., under forced vibration from an earthquake with concentrated frequency content, a better match with ideal RILD can be achieved by selecting the response frequency for ω_f in the CFB model. The response frequency, however, is not known prior to the ground motion event. This uncertainty is the primary motivation to design adaptive controllers that can estimate the dominant response frequency of the system in real time.

9.2 Proposed Adaptive Controllers

In this section, two adaptive control algorithm are proposed to estimate the dominant response frequency of a structure in real time. The estimated frequency is then updated in the all-pass filter (CFB model) to achieve desired causal RILD. By estimating the frequency of vibration, the true phase advance of the noncausal model is more accurately applied. The desired damping force is then tracked by a semi-active damper. The two adaptive controllers are discussed as follows [61].

9.2.1 Adaptive V-D Controller

The first proposed approach to approximate the dominant response frequency is to consider relative displacement and relative velocity measurements of the isolation layer. The dominant frequency of vibration can be approximated by dividing root mean square (RMS) of velocity signal by RMS value of displacement signal. By calculating a moving RMS of the velocity and displacement, the dominant frequency

can be updated in real time. This idea stems from displacement and velocity being out of phase by π/2 radians and with an amplitude ratio of 1:ω for a harmonic excitation of ω. At time t_i, the response frequency $\omega_{f,i}$ can be estimated from a moving RMS of velocity divided by the moving RMS of displacement as shown in Equation (9.2):

$$\omega_{f,i} \approx \frac{\sqrt{1/n(\dot{x}_i^2 + \dot{x}_{i-1}^2 + \ldots + \dot{x}_{i-n+1}^2)}}{\sqrt{1/n(x_i^2 + x_{i-1}^2 + \ldots + x_{i-n+1}^2)}} \tag{9.2}$$

where n is the number of samples for the moving RMS. If the sample length for the moving RMS is taken as the fundamental natural frequency of the structure T_n and data is sampled at Δt, then $n = T_n / \Delta t + 1$. Displacements and velocities can be directly measured by sensors or estimated from other sensors using discrete derivatives, integrals, or a Kalman filter.

9.2.2 Adaptive A-D Controller

The second proposed algorithm to approximate the dominant response frequency is to consider relative displacement and relative acceleration measurements of the isolation layer. A linear-least squares fit of the relative acceleration versus relative displacement represented in Cartesian coordinates will produce both a slope and intercept. The dominant response frequency is approximated as the square root of the negative slope of the linear fit. To avoid producing imaginary numbers, the negative sign is replaced with an absolute value operator. This idea stems from displacement and acceleration being out of phase by π radians and with an amplitude ratio of 1:ω^2 for a harmonic excitation of ω. Equation (9.3) depicts the Adaptive A-D approach, using a linear least-squares calculation for the slope with n sample points. At time t_i, the response frequency $\omega_{f,i}$ can be estimated as:

$$\omega_{f,i} \approx \sqrt{\left| \frac{\sum_{j=i-n+1}^{i} (x_j - \bar{x})(\ddot{x}_j - \bar{\ddot{x}})}{\sum_{j=i-n+1}^{i} (x_j - \bar{x})^2} \right|} \tag{9.3}$$

where n is the number of samples and $\bar{x}$ and $\bar{\ddot{x}}$ are the sample means of displacement and acceleration signals, respectively. Displacements and accelerations can be directly measured by sensors or estimated from other sensors using discrete derivatives, integrals, or a Kalman filter. To better illustrate this approach, a SDOF system with natural period of 4 seconds (typical of a base-isolated structure) is subjected to Kobe ground motion and displacement and relative acceleration responses of the structure is used in Adaptive A-D algorithm to estimate response frequency as shown in Figure 6. In this example, the RILD loss factor is chosen as $\eta = 0.4$. The frequency estimate at 15 seconds is shown, which uses data collected from 11 to 15 seconds. Relative acceleration versus relative displacement is represented in Cartesian coordinates and a linear-least squares fit of the data points are calculated as depicted in Fig. 9.1.

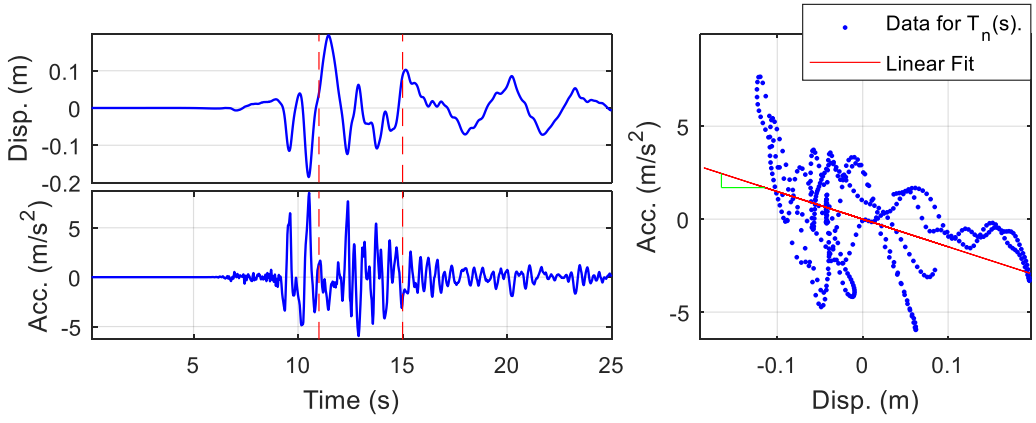

Fig. 9.1. *Estimated response frequency in Adaptive A-D algorithm.*

9.3 Numerical Study of the Adaptive Controllers

To illustrate the robustness of the adaptive algorithm in estimating dominant frequency of vibration, predetermined time history responses from a 5-story base-isolated structure are chosen as inputs for both algorithms. The structure has fundamental natural frequency of 0.25 Hz. Detailed properties of the structure will be presented in the next section (Section 9.4). The 5-story base-isolated building is subjected to the Hachinohe record (The N-S component recorded at Hachinohe Harbor during the Tokachi-oki earthquake of May 16, 1968). Responses are calculated using the Runge-Kutta numerical integration scheme and a sample rate of 2000 Hz.

Fig. 9.2 presents time history of input ground motion and response of the isolation layer. Displacement, velocity, and relative acceleration responses of the isolation layer are chosen as inputs to Adaptive V-D and Adaptive A-D controllers. For this study, there is no supplemental control in the isolation layer, i.e., the adaptive controllers only predict the response frequency but do not act on it. The performance of both adaptive control laws is dependent upon two important factors. First is the sampling range (in seconds) considered in the moving calculation windows. Second is the sampling rate of that data. These two factors are investigated herein.

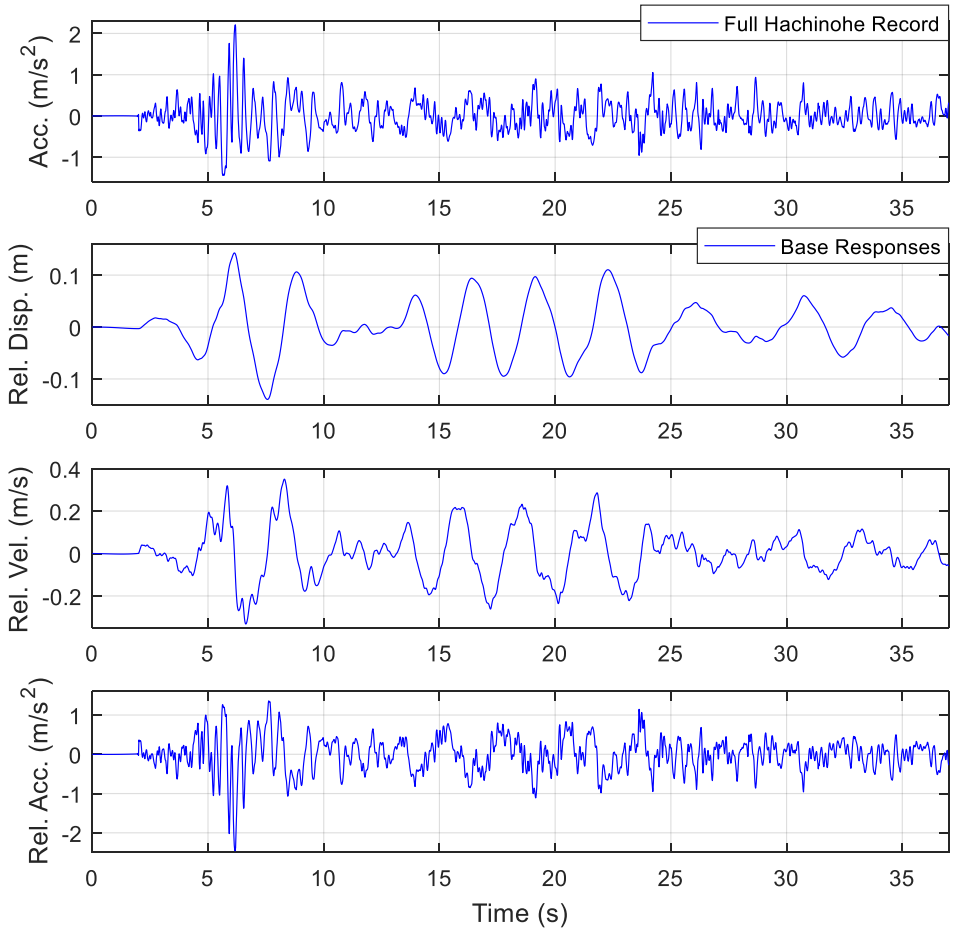

Fig. 9.2. *Hachinohe ground motion and isolation layer responses of an uncontrolled 5-story structure.*

9.3.1 Effects of Sampling Rate

To study the effects of sampling rate, the sampling range is first fixed at T_n seconds where T_n is the fundamental natural period of the structure. For this structure, T_n is 4 seconds. Therefore, both algorithms will consider data from the previous 4 seconds. For this fixed sampling range, the sampling rate is varied from 250 Hz to 1000 Hz. Fig. 9.3 illustrates the estimated frequency in time achieved from Adaptive V-D and Adaptive A-D controllers for 250 Hz and 1000 Hz. Fig. 9.3 also shows continuous wavelet transform plot of the isolation layer response displacement calculated using

MATLAB. In the wavelet transform, the lighter shade indicates a higher concentration of energy at a particular frequency.

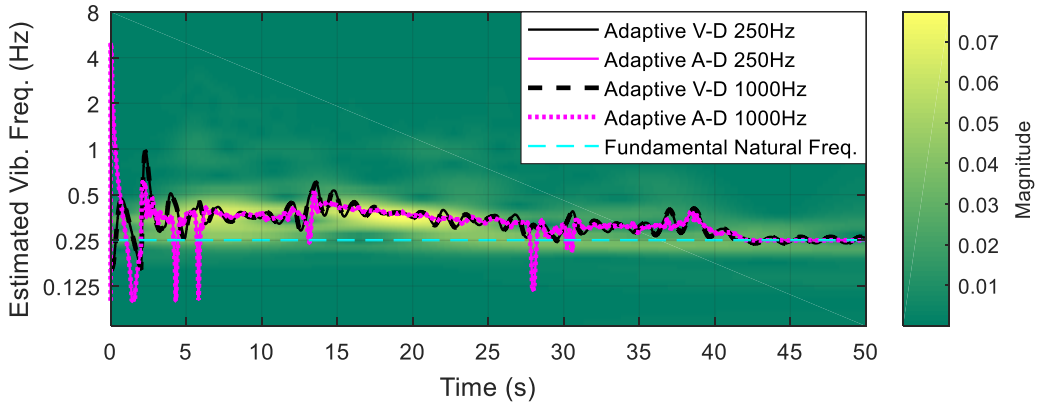

Fig. 9.3. *Estimated response frequency for the sampling rate of 250 Hz and 1000 Hz.*

As shown in Fig. 9.3, Adaptive V-D and Adaptive A-D controllers result in very similar estimated response frequency. Moreover, the sampling rates chosen do not have a noticeable influence on the results. In fact, simulation results show that the estimated frequency is similar for sampling rates of above 30 Hz for the structure chosen. As an additional validation, the estimated response frequency using the continuous wavelet transform analysis overlaps very closely with that of adaptive algorithm. This confirms the accuracy of Adaptive V-D and Adaptive A-D controllers in the real-time estimation of the response frequency of the structure. Choosing the fundamental natural frequency of the structure (also shown in Fig. 9.3) as an estimate of the response frequency is demonstrably less accurate. Fig. 9.4 shows same plot for the sampling rate of 1 Hz and 50 Hz.

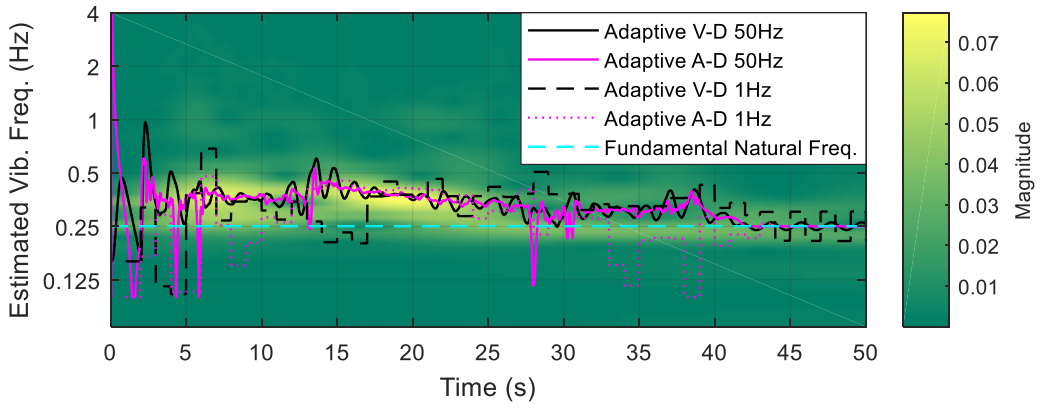

Fig. 9.4. *Estimated response frequency for the sampling rate of 1 Hz and 50 Hz.*

As depicted in Fig. 9.4, sampling data at 1 Hz resulted in poor response frequency estimation as compared to 50 Hz. Additionally, the estimated frequency from Adaptive V-D and Adaptive A-D no longer match each other or the wavelet transform for a 1 Hz sample rate. When designing the adaptive controller, the sampling rate should be small enough so that it is not computationally burdensome while large enough to maintain an accurate estimation of the response frequency.

Note that in this study, the sampling rate of the numerical integration is not altered (fixed at 2000 Hz). The data is down-sampled to the desired rate before being used in the adaptive algorithm.

9.3.2 Effects of Sampling Range

Next, the effects of sampling range on the accuracy of the estimated frequency are studied. The sampling rate is fixed at 250 Hz. Fig. 9.5 shows estimated frequency of both algorithms for sampling ranges of T_n and $T_n/4$.

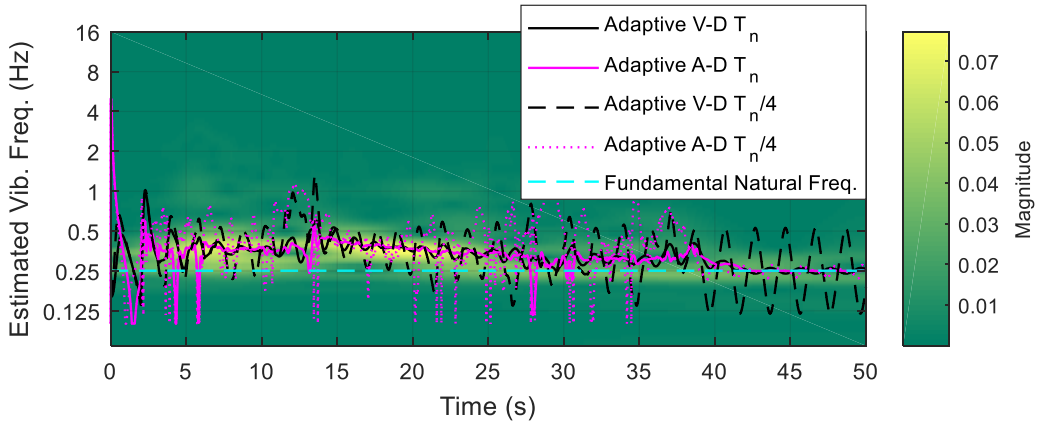

Fig. 9.5. *Estimated response frequency for sampling range of T_n and $T_n/4$.*

Selecting the sampling range as T_n allows approximately one cycle of response to enter into the calculations. A sampling range significantly lower than T_n will bias the algorithms, resulting in poor estimations of RMS for the V-D approach and a limited displacement and acceleration range for calculating the slope in the A-D approach. On the other hand, choosing a very long sampling range will make the algorithms less responsive to short-term changes in the structural response. A sampling range of T_n was found to consistently matches the frequencies predicted by the wavelet transform.

9.3.3 Summary of Adaptive Controller Design Parameters

The data sampling rate and range of the adaptive controllers should be designed in a way that is both accurate and efficient. For the remainder of this study, the sampling rate is selected as at least 250 Hz. This sampling rate is much larger than the Nyquist frequency of the structure and provides sufficient data points for smooth changes in the estimated frequency. The sampling range is selected as the fundamental natural period T_n of the structure. It is worthwhile to mention that although both adaptive algorithms update estimated response frequency after a T_n seconds time delay, they do not affect stability of the system due to inherent stability of semi-active damper.

Additionally, a saturation block is added to restrict the estimated response frequency to a range of 0.1 and 5 Hz. This saturation limit avoids unrealistic drifts in frequency estimations when the responses are low in amplitude and measurements may be dominated by sensor noise (i.e., before and after significant structural responses).

9.4 Structural Models

In this study, two low-frequency structural models are considered. The first structure is a 5-story base-isolated building with a large-scale MR damper (200 kN) that is installed at the isolation layer. The first three natural frequencies are 0.25 Hz, 3.16 Hz, and 5.94 Hz. Without the effects of MR damper, the structure has damping ratios of 4.97%, 3.17%, and 5.07% at the first, second, and third modes of vibration which is typical of a steel frame building with a low-damping isolation system. In RTHS, parts of a structure that are difficult to simulate numerically are represented as a physical substructure, while the rest are modeled numerically in simulation. Hence, for this study, MR damper is physically tested while the rest of the structure are numerically represented in RTHS loop. Table 9.1 shows dynamic properties of the structure.

Table 9.1. Parameters of the 5-story base-isolated structure.

Floor/Story	Floor Mass (kg)	Story Stiffness (kN/m)	Story Damping (kN·s/m)
0	244,800	3287	69.9
1	212,300	404,800	348.1
2	212,300	349,100	301.4
3	212,300	343,400	296.2
4	212,300	299,400	259.8
5	212,300	228,700	197.5

For the second structure, a 14-story high rise building (Iidabashi First Building or IFB) is selected [23] which was also previously used as a reference target building in Chapter 7. This structure has an inter-story isolation layer installed between 9^{th} and 10^{th} story. While in Chapter 7, 10 DOF scaled-down model was used for shake table RTHS testing, in this chapter the full-scale 15 DOF model is used for RTHS experiments. Moreover, in Chapter 7 the stories below the isolation layer were simulated numerically and superstructure was tested physically using the shake table RTHS, whereas; in this chapter 15 DOF model is tested numerically and MR damper is considered as the experimental substructure. Considering the scale of this structure, 20 large-scale (200 kN) MR dampers are assumed in the isolation layer as supplemental dampers. This structure is idealized as a 15-DOF lumped mass model which is shown in Fig. 7.1. Assuming the superstructure is a fixed-base building, the stories above the isolation layer have a fundamental natural frequency of 4.81 Hz and damping values are selected to provide 3% damping in this mode. Including the isolation layer, the superstructure has a fundamental natural frequency of 0.3 Hz and

the viscous damping of the isolation layer is selected to provide 5% damping in this mode. For the substructure (i.e. stories below the isolation layer), the structure has a fundamental natural frequency of 1.02 Hz and damping values are selected to provide 3% damping in this mode. Without considering the effects of supplemental isolation-layer damping, the total IFB building has natural frequencies of 0.29 Hz, 1.05 Hz, 2.93 Hz, 4.95 Hz, 6.92 Hz, and 7.26 Hz in its first six modes corresponding to damping ratios of 5%, 3.9%, 9.64%, 16%, 5.63%, and 22.4%. The fifth mode of vibration has significant motion in the inter-story isolation layer, leading to the notably low damping ratios when not including the supplemental damping device.

As with the 5-story building, the IFB structure is divided into two parts. The MR dampers are experimentally represented while the remainder of the structures is numerically simulated in the RTHS loop. A single MR damper specimen is used to represent all dampers because they will experience the same displacement inputs. Detailed properties of the IFB building can be found in Table 9.2.

Table 9.2. Parameters of the 14-story IFB building.

Floor/Story	Floor Mass ($kg \times 10^3$)	Story Stiffness ($kN/m \times 10^5$)	Story Damping ($kN \cdot s/m \times 10^5$)
1	5435	123.0	915
2	5533	128.1	915
3	5209	109.6	915
4	5189	98.21	915
5	5180	91.24	915
6	5091	85.48	915
7	4915	79.61	915
8	4915	74.60	915
9	12,704	71.67	915
10	4022	0.530	30.4
11	2315	344.3	415
12	2315	228.8	415
13	2305	201.1	415
14	2305	165.9	415
15	1658	94.31	415

9.4.1 MR Damper Specimen

Both structures are assumed to contain supplemental dampers in the isolation layer. To represent the supplemental dampers, a physical MR damper is evaluated in the laboratory through RTHS. This study uses a 200 kN MR damper (Fig. 9.6) developed by the Lord Corporation. The damper is 1.47 m in length, weighs approximately 2.5 kN, and has an available stroke of 584 mm [62].

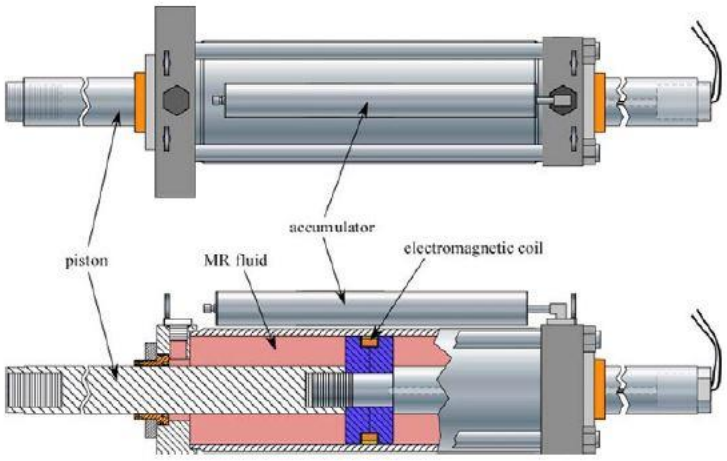

Fig. 9.6. *Large-scale MR damper* [62].

An over-driven back-driven semi-active clipped optimal controller is used for the large-scale MR damper to determine the current for the MR damper required to achieve the desired force [63]. Fig. 9.7 illustrates an experimental RTHS example of the tracking of the desired force by the measured force using this algorithm. The results correspond to the 5-story base-isolated structure. The structure is subject to 30% amplitude scaling of the Kobe record (the N-S component of the Japanese Meteorological Agency station during the Kobe earthquake of January 17, 1995). The desired force is determined using the CFB model in Equation (56) with ω_f equal to 1.57 rad/sec (0.25 Hz) and η of 0.6. The physical tracking of the desired force is very good. The residual force limitation [64] of the damper is about 18 kN; therefore, the damper force cannot generally decrease beyond that limit except under very small velocities.

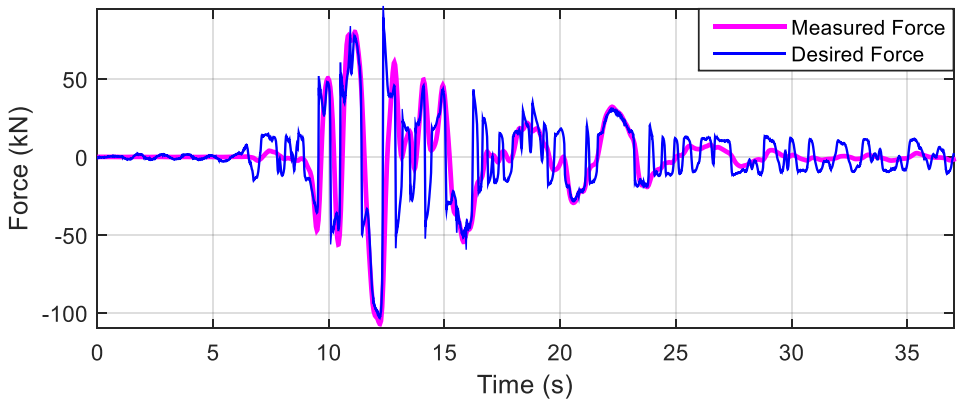

Fig. 9.7. *Desired and measured damping force using the force tracking control algorithm.*

9.5 RTHS Experimental Results and Discussion

A series of RTHS tests were conducted to examine the performance of the proposed adaptive controllers incorporated into base-isolated and inter-story isolated buildings. The test consists of an MTS servo-hydraulic actuator, a 200 kN MR damper, and a dSPACE DS1103 digital signal processing board. A load cell and linear variable displacement transducer (LVDT) were used to capture damper force and displacement, respectively. Fig. 9.8 shows an image of the RTHS test setup.

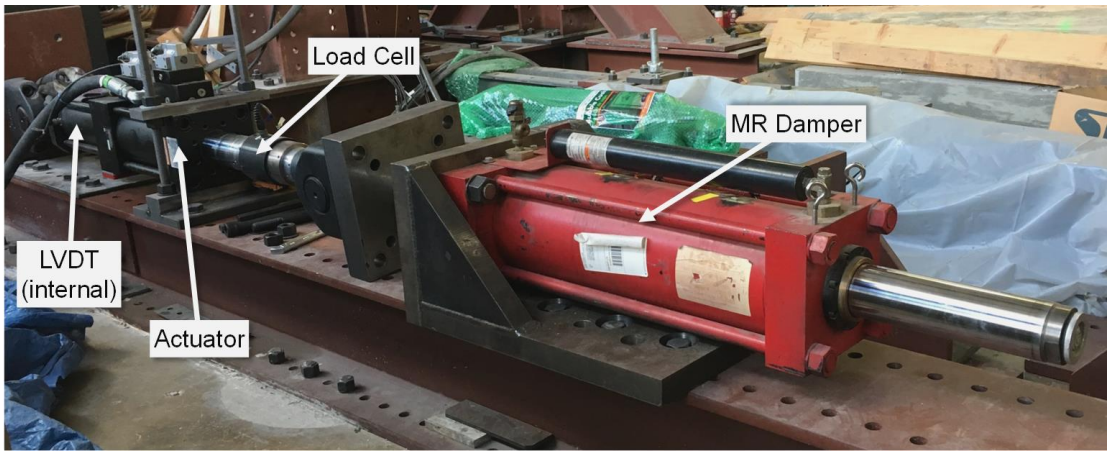

Fig. 9.8. *Experimental test setup for RTHS.*

Numerical integration of the numerical substructure and interface with sensors and actuators was performed by the dSPACE digital signal processing board. In all experiments, the loss factor η is taken as 0.6. First, the performances of the adaptive controllers are compared to fixed-frequency CFB approach and to noncausal simulations. The goal is to improve upon the fixed-frequency CFB approach by better matching non-casual simulations. Second, the seismic performance of all causal approaches are compared to passive on and passive off semi-active control laws.

For this study, the sampling rate of the RTHS loop and numerical integration is set to be 2000 Hz. In RTHS, the earthquake ground motion is applied to the numerical substructure (either of the 5-story structure or IFB). The displacement of the isolation layer is then applied to the MR damper specimen using the servo-hydraulic actuator. A model-based feedforward controller is used to compensate for the actuator dynamics [23]. The restoring force measured from the actuator load cell is returned to the numerical substructure to complete the RTHS loop.

9.5.1 Adaptive versus fixed-frequency CFB models

In this section, the ability of adaptive controllers to mimic ideal RILD in a practical design will be assessed and compared to fixed-frequency CFB model. Ideal RILD is evaluated using a numerical model of the structure with ideal RILD (instead of MR damper) in the isolation layer. This numerical model is noncausal and therefore evaluated in the frequency domain.

9.5.1.1 Base-isolated structure

At first, the 5-story base isolated structure is subjected to 50% amplitude scaling of the Hachinohe record. Adaptive controllers are designed with a sampling

rate of 250 Hz and sampling range 4 seconds. Fig. 9.9 shows RTHS experimental responses of this structure for CFB (fixed-frequency), Adaptive V-D, Adaptive A-D, and noncausal models.

As shown in Fig. 9.9, CFB model has slightly higher displacement and acceleration peaks when compared to both adaptive controllers. Looking at the hysteresis, the CFB approach resulted in a positively skewed hysteresis when compared to noncausal hysteresis. That leads to a slight increase in stiffness which results in acceleration increase for CFB model. On the other hand, Adaptive A-D and Adaptive V-D controllers are more in phase with noncausal RILD.

This behavior can be further studied by comparing estimated response frequency from the adaptive controllers to the fundamental natural frequency of the structure. As it is shown in Fig. 9.10, both Adaptive A-D and Adaptive V-D controllers estimate the response frequency very well when compared to the continuous wavelet transform. Note that the wavelet transform is calculated from the noncausal model's isolation layer drift.

The Hachinohe earthquake causes the structure to respond at a frequency larger than the natural frequency of the structure. Using the fixed-frequency CFB approach, the damping force will have a phase advance of less than 90° with respect to displacement, producing a positively skewed hysteresis. On the other hand, by using adaptive controllers, the true response frequency is being used in the all-pass filter which is estimated and updated in real time. Hence, resulted damping force maintains the $\pi/2$ phase advance with displacement, better approximating the noncausal ideal RILD behavior.

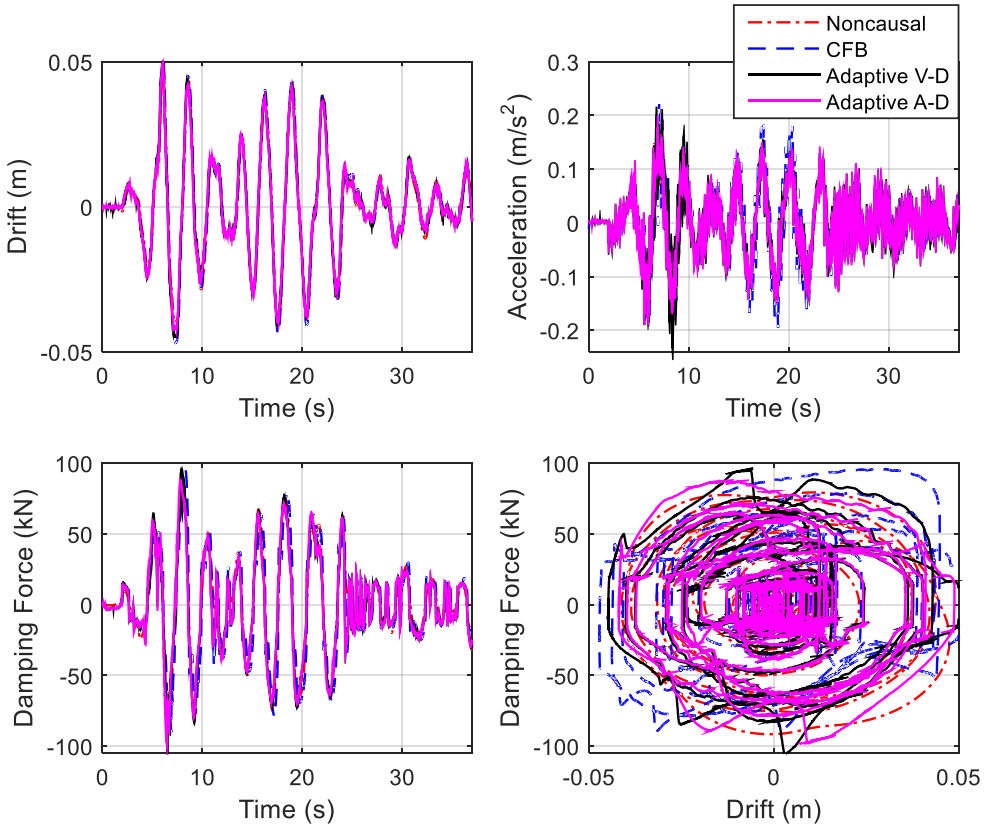

Fig. 9.9. *5-story structure isolation layer responses with applied 50% Hachinohe earthquake.*

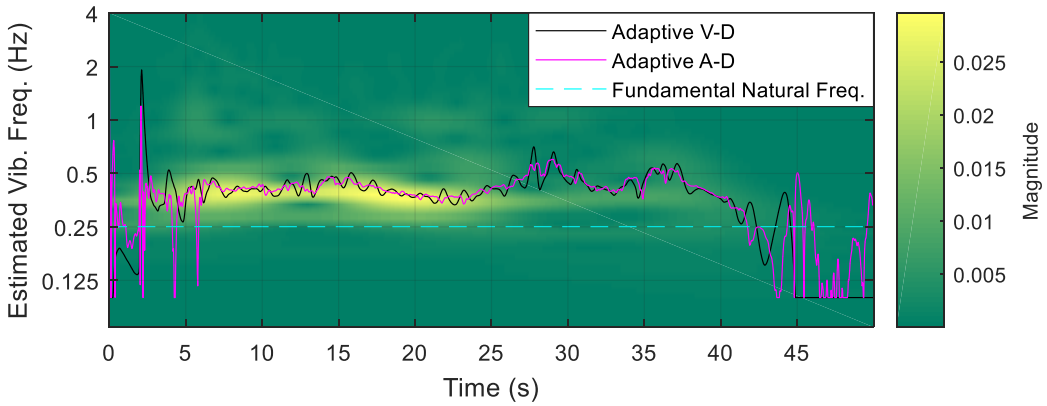

Fig. 9.10. *5-story structure estimated response frequency with applied 50% Hachinohe earthquake.*

The benefits of the adaptive controllers are even clearer when looking at earthquakes that produce response frequencies much further from the fundamental natural frequency of the structure. The base-isolated structure is subjected to 30%

amplitude scaling of the Kobe earthquake. Fig. 9.11 and Fig. 9.12 show structural responses and frequency tracking for this record.

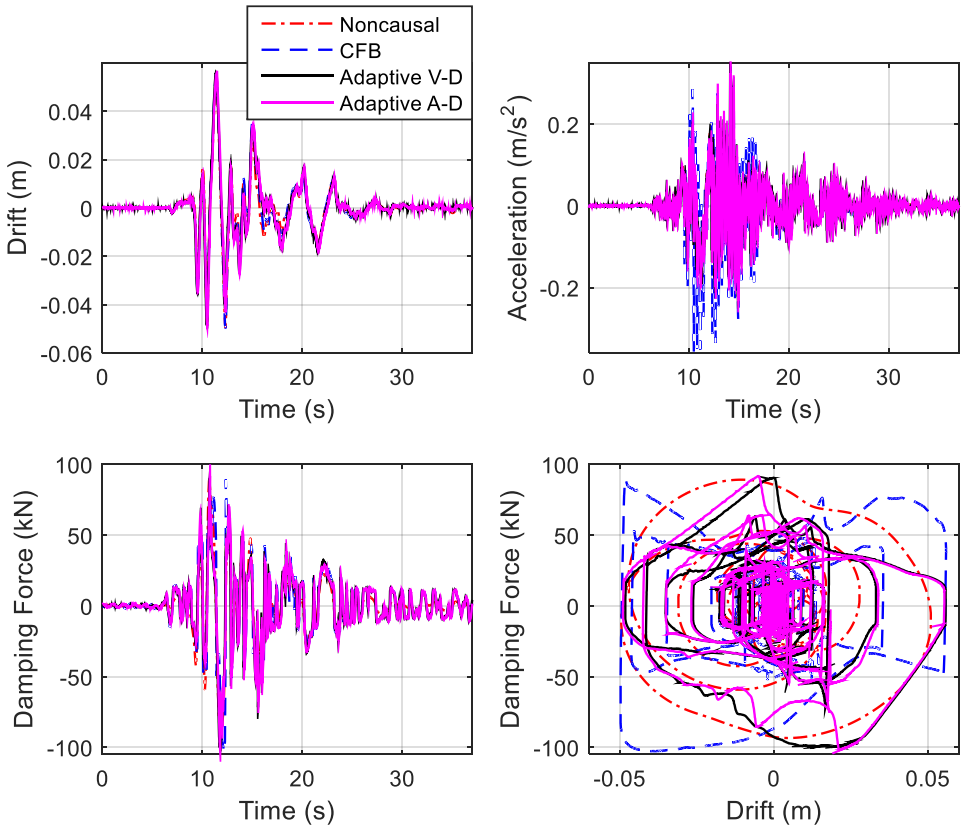

Fig. 9.11. *5-story structure isolation layer responses with applied 30% Kobe earthquake.*

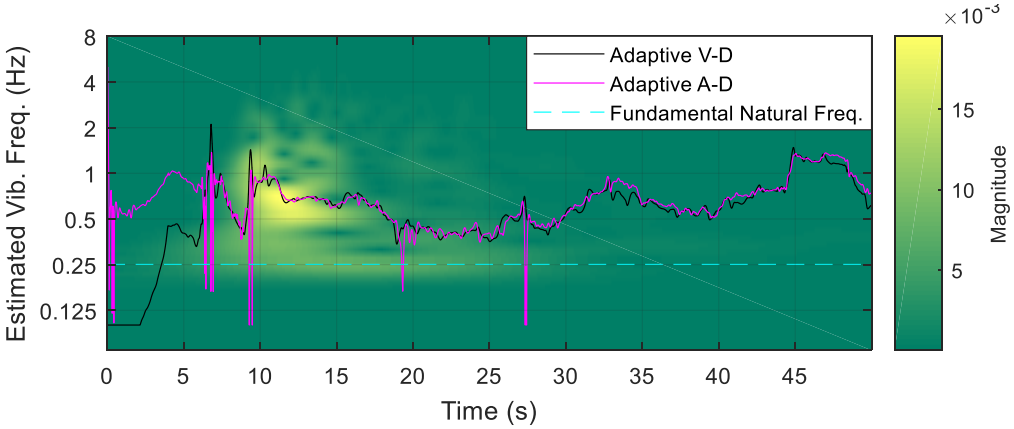

Fig. 9.12. *5-story structure estimated response frequency with applied 30% Kobe earthquake.*

Kobe earthquake has high frequency components, leading to a dominant response frequency higher than Hachinohe record. Therefore, the hysteresis loop for CFB model is even more skewed, leading to high acceleration peaks as shown in Fig. 9.11 when compared to adaptive controllers and noncausal simulation. Moreover, from Fig. 9.12 it is evident that both adaptive algorithms estimated higher response frequencies when compared to Hachinohe record. Fig. 9.12 also depicts the estimated response frequency obtained from wavelet transform analysis of the noncausal model isolation layer drift. Like the Hachinohe record, estimated frequency from adaptive control laws are almost equal to that of obtained from wavelet analysis, in particular during the strong ground motion part of the earthquake. Therefore, this figure also validates the accuracy of adaptive controllers in calculating the response frequency of the structure in real time.

In summary, while the CFB model only uses one frequency (i.e. the fundamental natural frequency of the structure) for all type of excitations, both adaptive control laws estimate the response frequency in real time. As a result, using Adaptive V-D or Adaptive A-D controllers enhances structural performance by better mimicking ideal RILD as compared to a fixed-frequency CFB approach.

9.5.1.2 Inter-story isolated structure

To investigate performance of adaptive algorithm under a different structure, the IFB inter-story isolated structure is subjected to 20% amplitude scaling of the Hachinohe record. As discussed in previous sections, the fundamental natural frequency of the inter-story isolated building's substructure is used in CFB model. This selection results in better forced-vibration responses. For this structure, the

adaptive controllers are designed with a sampling rate of 500 Hz and a sampling range of 3.4 seconds. Fig. 9.13 and Fig. 9.14 show structural responses and estimated response frequency for inter-story isolation layer when IFB structure is subjected to the Hachinohe record.

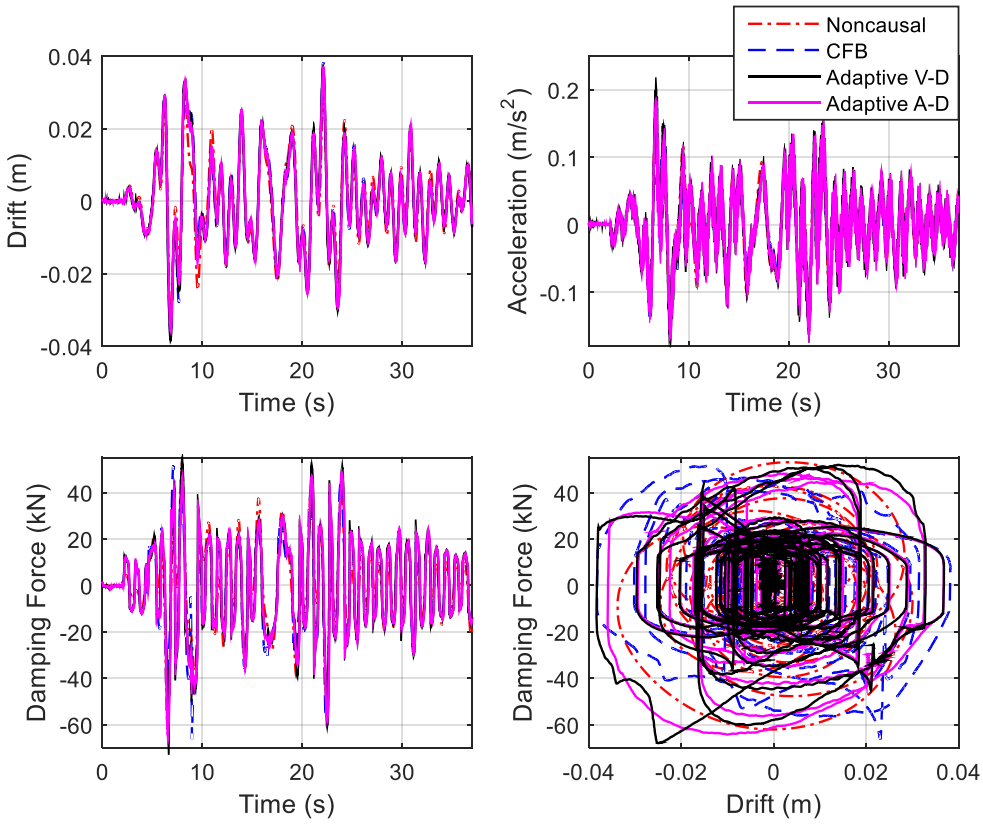

Fig. 9.13. *IFB isolation layer responses with applied 20% Hachinohe earthquake.*

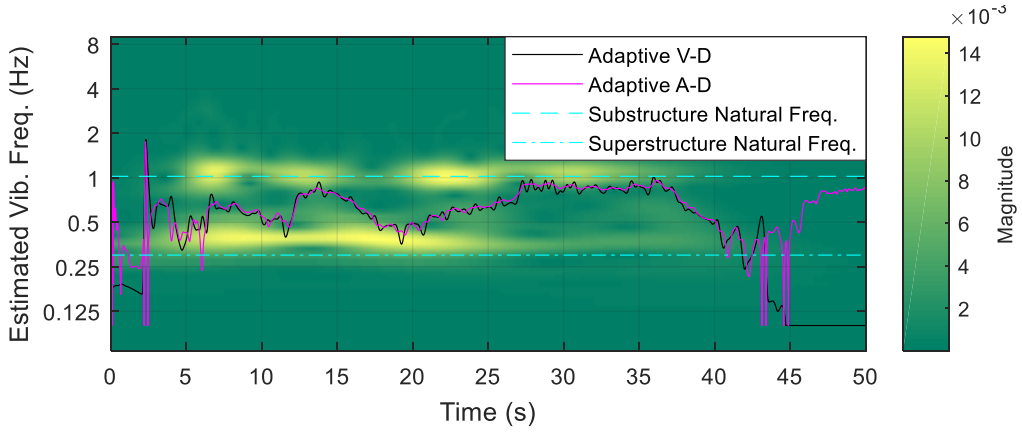

Fig. 9.14. *IFB estimated response frequency with applied 20% Hachinohe earthquake.*

As it is clear from Fig. 9.13, both adaptive and fixed-frequency approaches resulted in similar seismic performance when compared to the noncausal model. Fig. 9.14 shows estimated response frequency in time from wavelet analysis using the noncausal isolation layer displacement. Two major frequency ranges have the highest concentration of energy as indicated by the wavelet analysis. The first one is around the fundamental natural frequency of the structure (around 0.3 Hz) and the second one is at the substructure fundamental natural frequency (around 1 Hz). Both adaptive algorithm predict similar dominant response frequencies over time, matching well with the wavelet transform. For the fixed CFB model, the substructure fundamental natural frequency is used. The isolation layer response contains significant frequency content at this forced frequency, resulting in a good match with adaptive and noncausal controllers. The addition of some frequency content at the fundamental natural frequency of the superstructure leads to a slightly negatively skewed hysteresis as compared to noncausal and adaptive algorithms (see Fig. 9.13).

To further investigate robustness of adaptive algorithm over a broad range of excitations, the IFB inter-story isolated structure was subjected to 75% amplitude

scaling of the Sakishima record. This record is a predominantly low-frequency earthquake. Fig. 9.15 and Fig. 9.16 depict structural responses and estimated response frequency for inter-story isolation layer. Because the entire Sakishima ground motion is a 500 second record, time history responses of Fig. 9.15 are shown between 150 to 300 seconds, the main strong ground motion portion of the earthquake.

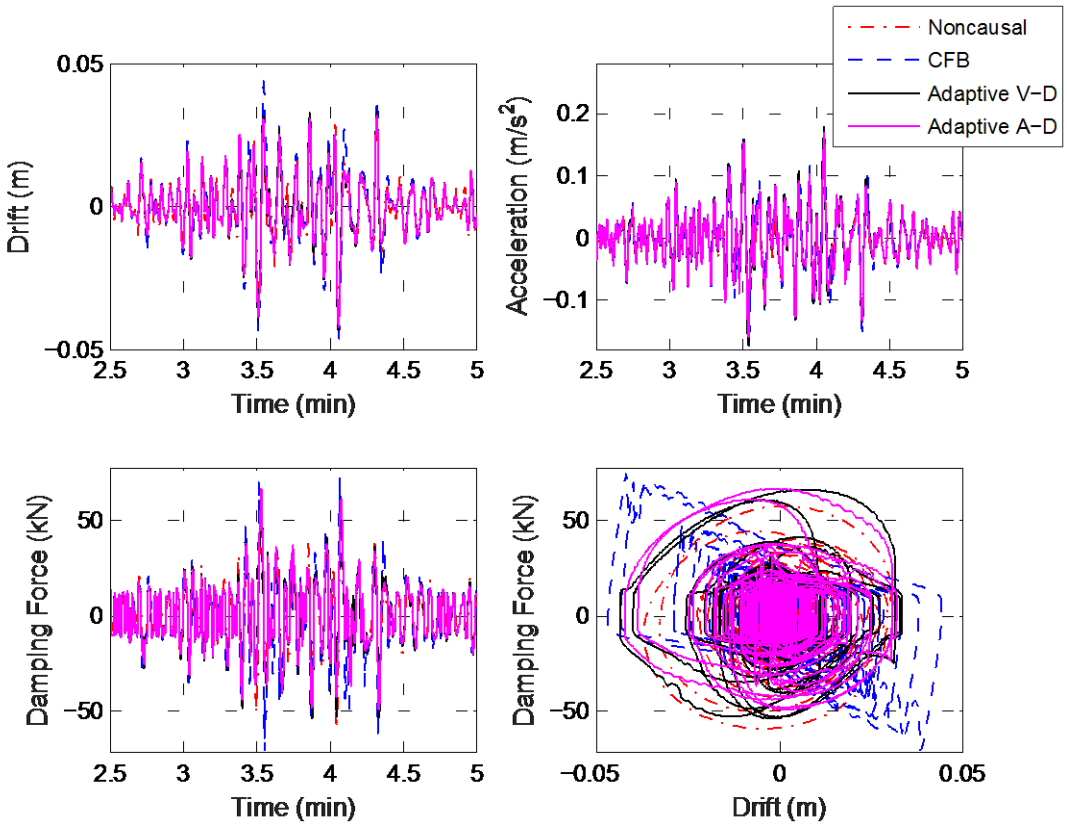

Fig. 9.15. *IFB isolation layer responses with applied 75% Sakishima earthquake.*

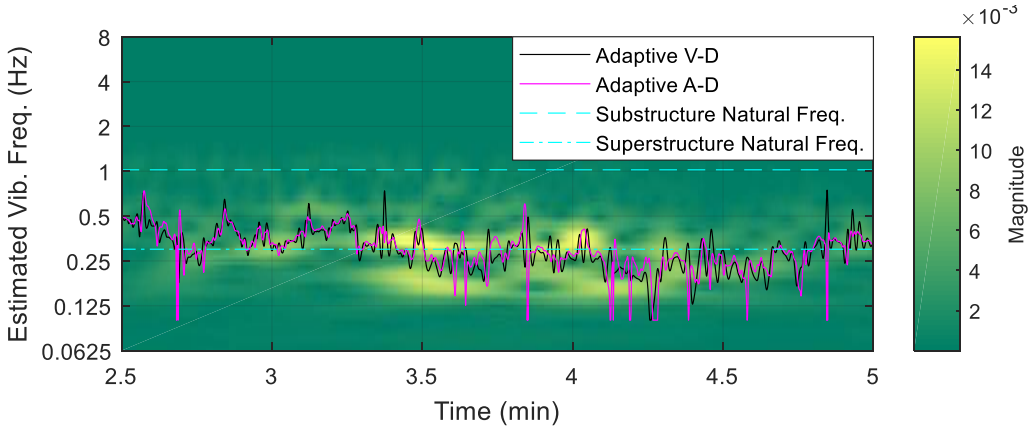

Fig. 9.16. *IFB estimated response frequency with applied 75% Sakishima earthquake.*

In contrast to the Hachinohe or Kobe earthquakes, for the case of the Sakishima earthquake, the CFB model results in slightly higher acceleration peaks and much higher displacement responses as compared to adaptive controllers and noncausal simulation results. The CFB approach produces a negatively skewed hysteresis, leading to decrease in structural stiffness and increase in displacement responses. On the other hand, both adaptive controllers resulted in in-phase hysteresis plots matching ideal RILD and therefore better displacement and acceleration responses. Fig. 9.16 shows estimated response frequency by Adaptive V-D and Adaptive A-D algorithm. As expected for this low-frequency ground motion, the estimated response frequency is below the fundamental natural frequency of the substructure used in CFB controller. Therefore, the CFB model provides a phase advance larger than 90° with respect to displacement (see Fig. 5.1) and that resulted in a negatively skewed hysteresis and increased displacement responses. For this earthquake, better performance would be achieved by selecting the natural frequency of the superstructure for the CFB model. This can also be confirmed by comparing looking at the estimated response frequency obtained from wavelet analysis which

overlaps with both adaptive controllers and is close to fundamental natural frequency of the superstructure. As clearly shown here, this compromise between low and high frequency content earthquakes does not exist for adaptive controllers. Therefore, similar to other records with different frequency content, both adaptive controllers enhance structural performance by better applying the correct phase advance of noncausal model and therefore better mimicking the ideal RILD responses.

9.5.2 Comparison to passive-on and off controllers

In this section, the performances of adaptive and fixed-frequency controllers are compared to traditional passive-on and passive-off semi-active algorithms. For this purpose, the 5-story base isolated building is subjected to 30% amplitude scaling of the Kobe earthquake in RTHS. Passive-on current is set to be 0.7 Amps so that the semi-active controllers and passive-on controller have similar level of damping force for the applied ground motion. Passive-off current is set as 0 Amps. Fig. 9.17 illustrates time history response comparison of these models.

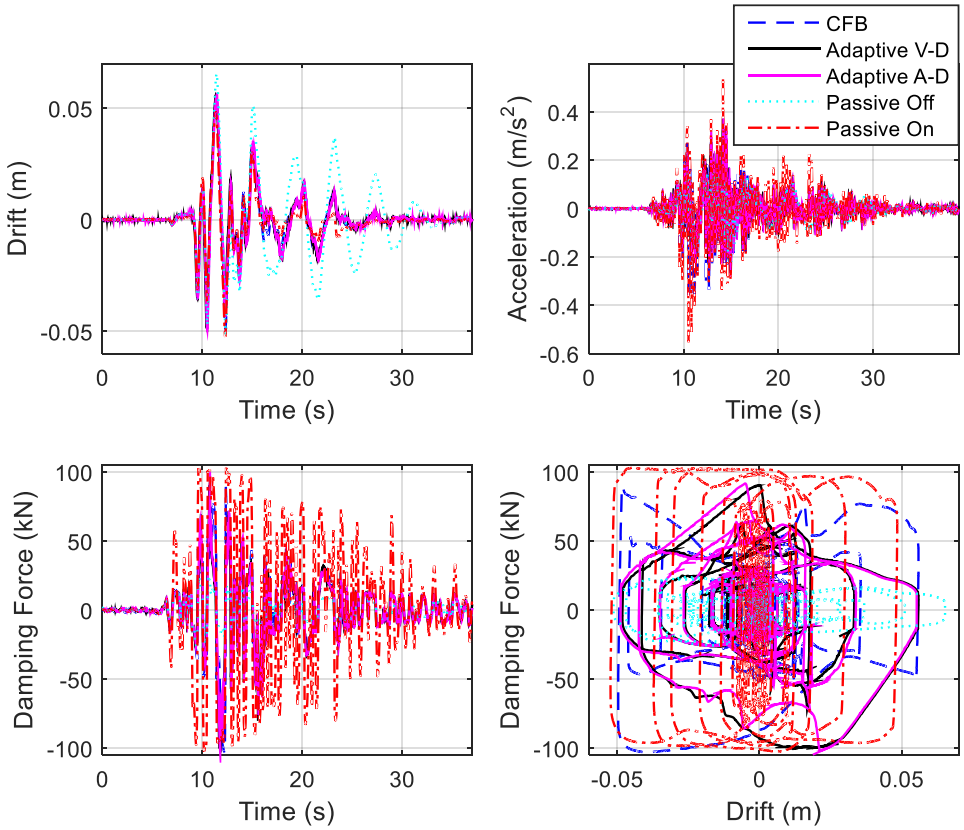

Fig. 9.17. *Semi active control responses vs passive-on and off for isolation layer with applied 10% Kobe earthquake.*

It can be concluded from Fig. 9.17 that both semi-active adaptive controllers suppress the displacement as effectively as passive-on, while generating much lower acceleration responses in comparison to passive-on controller. This demonstrates that using a semi-active adaptive control algorithm to mimic a causal realization of RILD can produce better seismic performance in comparison to both passive-on and passive-off controllers.

Chapter 10: Passive Realization of RILD

Passive control devices are the most practical and common device found in civil engineering applications. They are more accepted by the industry than their semi-active or active counterparts. In this chapter passive implementation of RILD is explored. First equations are derived, and next practical passive implementation is discussed through proposed mechanical devices.

10.1 Methodology

Consider a Maxwell element having a stiffness of k_M and a damping coefficient of c_M as shown in Fig. 10.1, the transfer function from the measured displacement X_m to the control force F_M is as follows:

$$\frac{F_P(i\omega)}{X_{m(i\omega)}} = \frac{i\omega}{i\omega+\frac{k_M}{c_M}} k_M \tag{10.1}$$

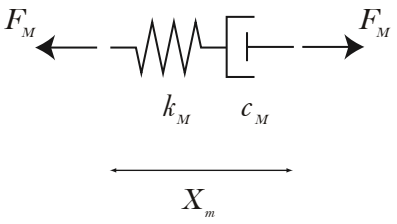

Fig. 10.1. *Maxwell Element.*

Now consider two SDOF structures, one with stiffness of k (model A) and the other one with the stiffness of $\hat{k}$ (model B). Equip model A with a CFB algorithm and

model B with a Maxwell element with stiffness of $k_M = \hat{k}\hat{\eta}$ and a damping coefficient of $c_M = \frac{\hat{k}\hat{\eta}}{\omega_n}$.

The equations of motion of the two models subjected to earthquake ground motion can be written in frequency domain as:

$$(-\omega^2 m + \frac{i\omega - \omega_n}{i\omega + \omega_n} k\eta + k)X(\omega) = -\omega^2 m\ddot{X}_g(\omega) \tag{10.2}$$

$$(-\omega^2 m + \frac{i\omega}{i\omega + \omega_n} \hat{k}\hat{\eta} + \hat{k})X(\omega) = -\omega^2 m\ddot{X}_g(\omega) \tag{10.3}$$

Equation (10.2) represents model A and Equation (10.3) shows model B. Equating the two equations will result in:

$$\hat{k} = k(1 - \eta) \tag{10.4}$$

$$\hat{\eta} = \frac{2\eta}{1-\eta} \tag{10.5}$$

In other words, by increasing the Maxwell element loss factor and decreasing the structural stiffness, the CFB model can be achieved through a passive mechanical system. However, decreasing structural stiffness is not a viable alternative for existing structural systems. Additionally, decreasing stiffness through conventional means (e.g., the structural members), may result in failure under strength limits.

10.2 Proposed Mechanical System

Adding a negative stiffness in parallel with the Maxwell element as shown in Fig. 10.2 shifts the zero to a positive real value to passively implement the first-order all pass filter (i.e. CFB model) as shown in Fig. 10.3(b) and Equation (5.14).

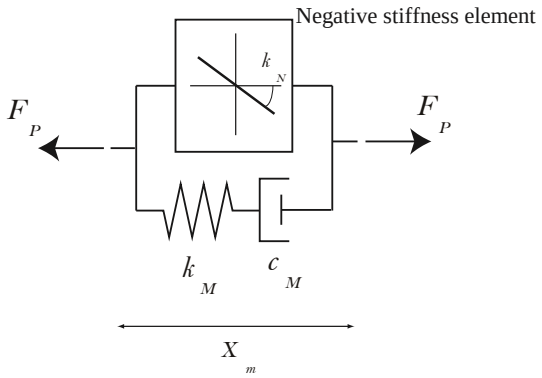

Fig. 10.2. *Mechanical model of the proposed passive system.*

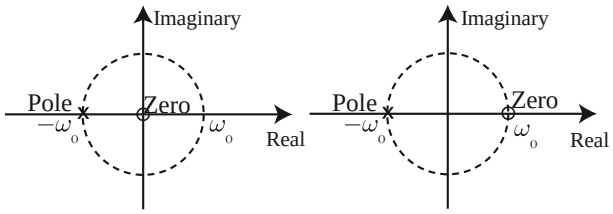

(a) Maxwell element (b) Proposed system

Fig. 10.3. *Pole-zero map.*

where k_N in Fig. 10.2 is the required negative stiffness generated by the negative stiffness element and can be calculated as follows:

$$k_N = \hat{k} - k = -k\eta \tag{10.6}$$

The combination of a Maxwell element and an ideal negative stiffness will be able to physically match the CFB model, providing a passive alternative for RILD. The resultant force of the negative stiffness and Maxwell elements, $F_P(i\omega)$, can be expressed in frequency domain, as represented in Equation (10.7):

$$F_P(i\omega) = (k_N + \frac{i\omega k_M}{i\omega + \frac{k_M}{c_M}})X_m \tag{10.7}$$

By substituting $k_N = -k\eta$, $k_M = \hat{k}\hat{\eta}$ and a damping coefficient of $c_M = \frac{\hat{k}\hat{\eta}}{\omega_n}$ in Equation (10.7), the resultant force of a Maxwell element and negative stiffness device will be as:

$$F_P(i\omega) = \eta k \frac{i\omega - \omega_n}{i\omega + \omega_n} X_m \tag{10.8}$$

From Equation. (10.8), it can easily be found that the control force provided by the proposed model is expressed exactly the same as that in Equation. (5.14), implying that the CFB algorithm can be physically realized by using the proposed passive model.

10.3 Proposed Negative Stiffness Device

A Negative Stiffness Device (NSD) can be used in parallel with Maxwell element where negative stiffness can be achieved through "apparent yielding" [65]. More recently, Sun et al. [66] proposed a NSD device to be used in base-isolated structures which consists of a highly compressed spring, a wheel and a sinusoidal curved template that the wheel can roll on. The proposed NSD device generates nonlinear negative stiffness emulating "apparent yielding" without permeant deformation. Fig. 10.4 shows basic mechanism of the NSD installed in an isolation layer as presented in [66]. As stated in [66], the force generated by NSD as a function of the imposed displacement is given by the equation:

$$F_{NSD} = k\left[\Delta L - \frac{A}{2} + f(x)\right]\frac{f'(x)}{1+(f'(x))^2} + sign(\dot{x})\mu N(cos\ \alpha)^2 \tag{10.9}$$

where $f(x)$ is the curved template function, A is the amplitude of the $f(x)$, ΔL is the pre-compression length of the spring and k is the stiffness of the spring. α is the angle between tangent line at the contact point and x axis. μ is friction coefficient between the roller and the curve template and from Fig. 10.4, $N = k\left[\Delta L - \frac{A}{2} + f(x)\right]$.

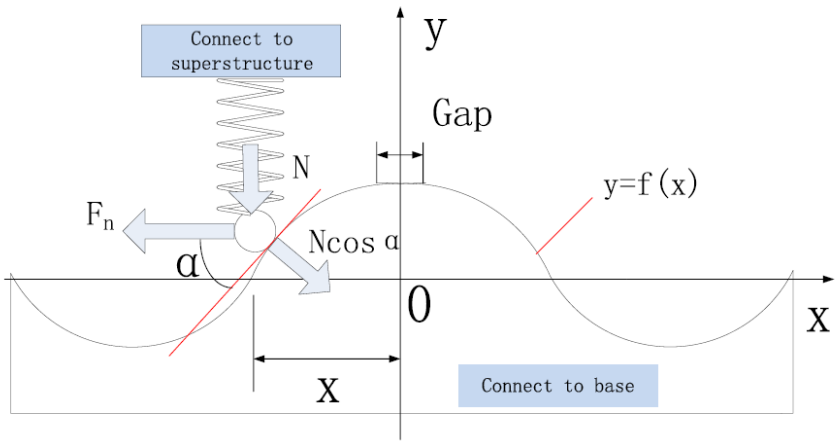

Fig. 10.4. *Basic mechanism of the negative stiffness device* [66].

To achieve passive RILD behavior as proposed herein, a linear negative stiffness device is needed. One possibility to create such a device is to use a template designed such that the slope change of the template is nearly linear. The desired magnitude of linear negative stiffness then can be obtained by adjusting the stiffness of the pre-compressed spring. If successful, the passive device will be able to reproduce the CFB model responses.

Fig. 10.5 shows a schematic plan view of the proposed template for this study which is anticipated to generates linear negative stiffness where it can be installed at the isolation layer of base-isolated structures. The template is a curved cosine or parabolic function with no gap and has to be designed such that it starts at maximum level at the origin and decrease to a level where both the template slope and induced NSD force remain linear. Moreover, it is critical to keep the friction coefficient, μ, as small as possible and close to zero.

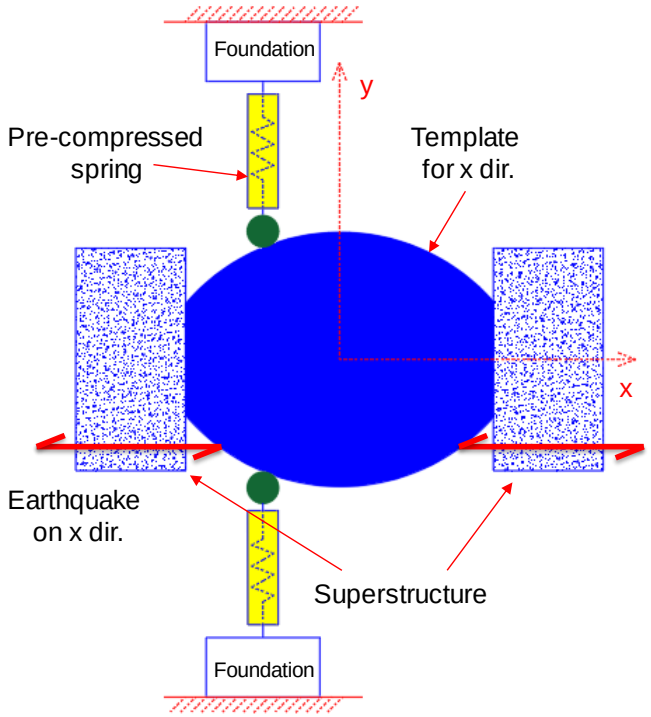

Fig. 10.5. *Schematic plan view of the proposed template for x-directional earthquake.*

In this regard, the use of a mechanical device as developed in Fig. 10.5 may be a suitable mean to implement the negative stiffness. Otherwise, the most straightforward means to create effective negative stiffness is by simply reducing the horizontal stiffness of the isolators.

10.4 Numerical Analysis of Passive Model

To investigate the performance of the passive RILD model proposed in this study, the seismic responses of a base-isolated SDOF structure (as described in Section 4.2) incorporated with the proposed NSD is analyzed by conducting time history analysis. In this study, $\Delta L = 0.6\ (m)$, $A = 0.6$, $k = 8\ (kN/m)$ and template curved function, $f(x)$, is presented in as follows:

$$f(x) = 0.3\cos(^{4\pi}/_{6}) \tag{10.10}$$

Numerical analysis was conducted on the SDOF base isolated structures incorporated with: (1) ideal noncausal RILD where η = 0.4, (2) CFB model where ω_n = 1.57 rad/s or equivalently a Maxwell element where k_M = 9.82 *kN/m* and c_M = 6.27 *kNs/m* in parallel with ideal NSD where $k_N = -4.91$ *kN/m*, and (3) Maxwell element where k_M = 9.82 *kN/m* and c_M = 6.27 *kNs/m* in parallel with proposed NSD given by Equation 10.9 and 10.10. All structures are subjected to full Hachinohe record. Fig. 10.6 shows time history responses and Fig. 10.7 illustrates hysteresis plots of all the models with applied Hachinohe record.

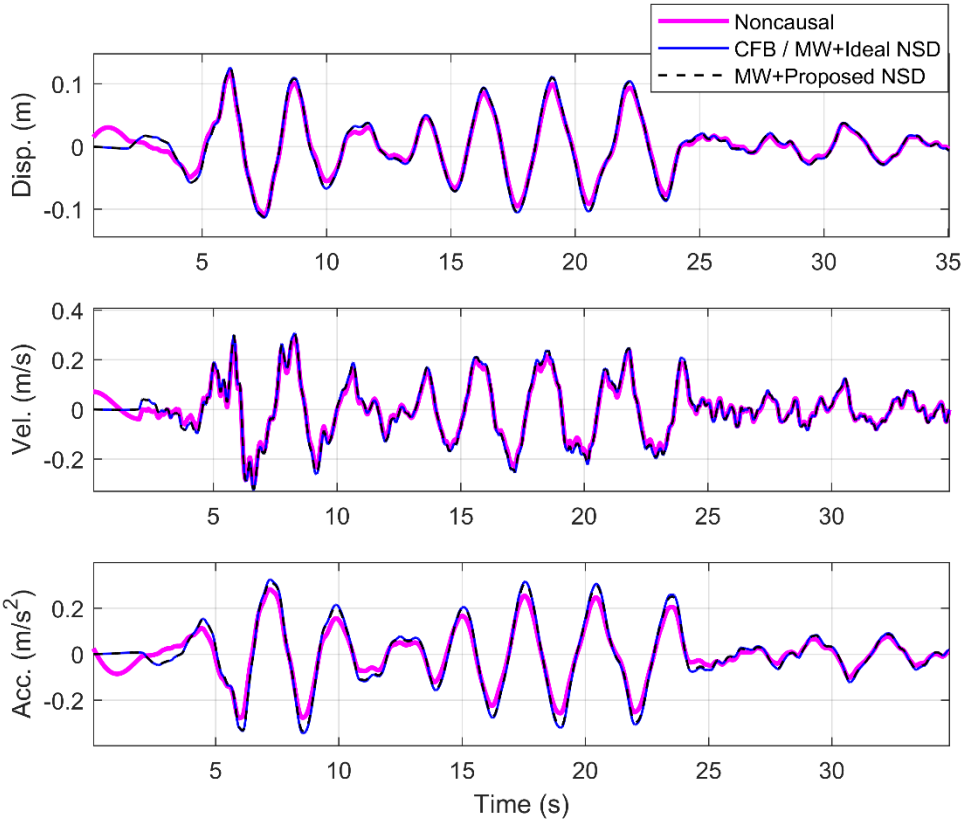

Fig. 10.6. *Structural responses with applied full Hachinohe earthquake.*

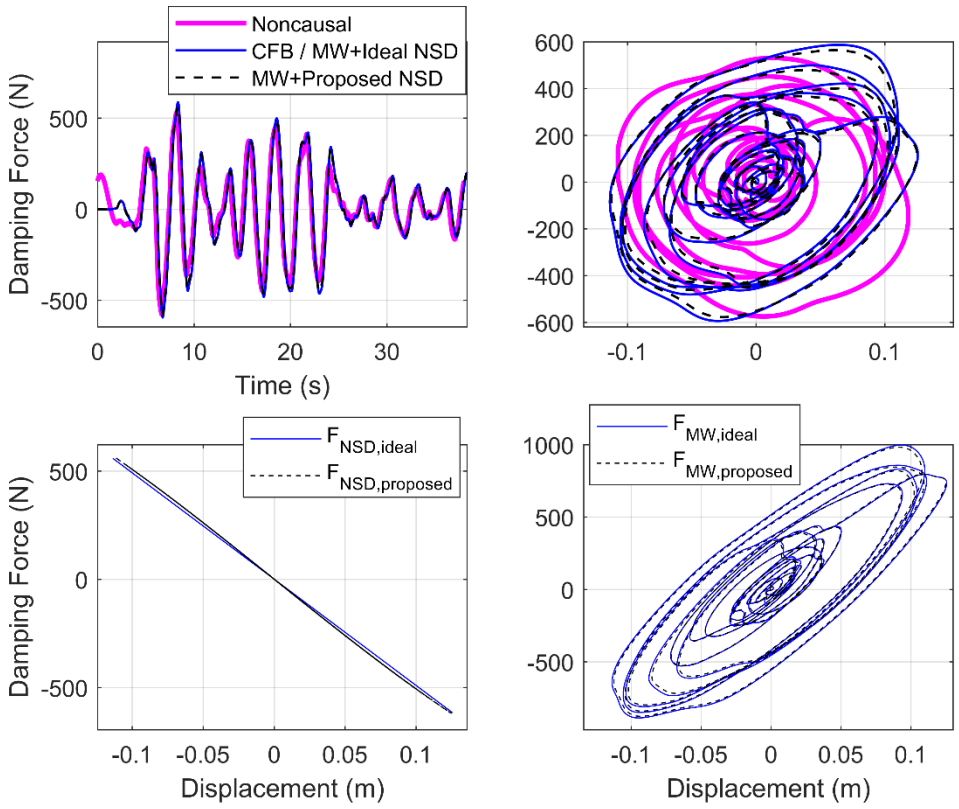

Fig. 10.7. *Hysteresis plots with applied full Hachinohe earthquake.*

As it is represented in Fig. 10.6, both CFB model and Maxwell element in parallel with ideal NSD result in completely identical responses. Moreover, the practical combination of Maxwell element in parallel with a proposed NSD leads to a very close match with that of CFB algorithm, proving to be a suitable mean for passive realization of RILD. Fig. 10.7 compares damping force time history and hysteresis plots of all the models as well as hysteresis plots for individual NSD and Maxwell elements for both ideal and proposed devices. Again, it is observed that Maxwell element in parallel with the proposed passive device closely matches with that of CFB algorithm. Moreover, Fig. 10.7 also shows the ability of the proposed NSD to generate a linear negative stiffness hysteresis which match closely to that of

the ideal NSD element. Same conclusion can be made for comparison of the Maxwell elements hysteresis of the two cases.

To investigate the performance of the proposed passive device under different earthquakes, all base-isolated structures are excited by Kobe and Northridge ground motions. Fig. 10.8 and Fig. 10.9 show damping force time history and hysteresis plots with applied Kobe and Northridge earthquakes, respectively.

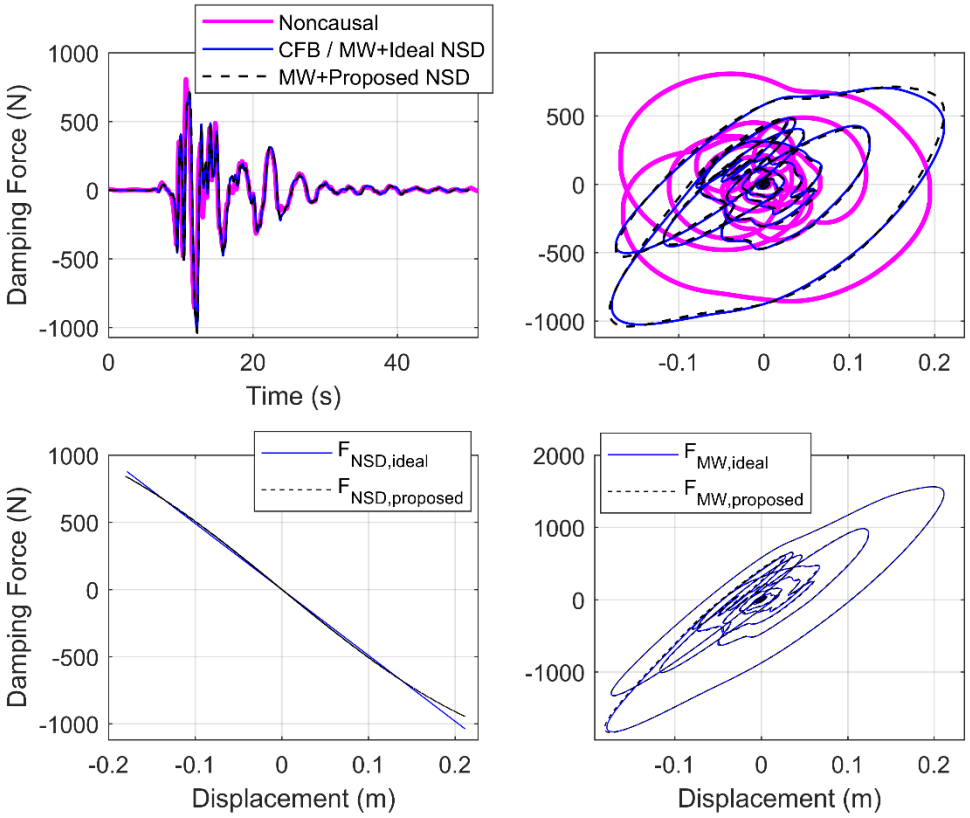

Fig. 10.8. *Hysteresis plots with applied full Kobe earthquake.*

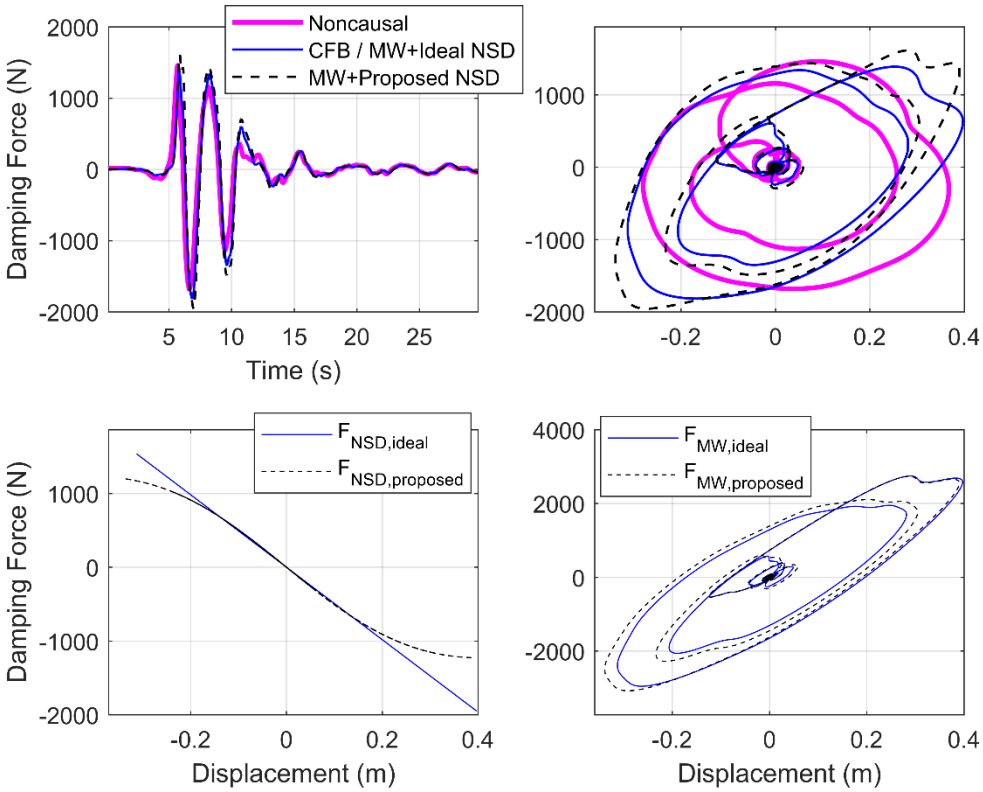

Fig. 10.9. *Hysteresis plots with applied full Northridge earthquake.*

Same conclusions can be made for the case of applied Kobe earthquake as for the Hachinohe record as shown in Fig. 10.8. It can be asserted that for the case of Kobe earthquake, the proposed NSD can also generate a linear negative stiffness hysteresis which closely match with that of ideal NSD element. Therefore, similar time history responses is also obsereved. However, for the case of Northride ground motion, the generated hysteresis by the proposed NSD results in slightly nonlinear behaviour for larger displacement values as shown in Fig. 10.9. This is due to the fact that the recorded Northride earthquake contains a large spike which leads to a larger displacement values for the strong ground motion part of the record. As the roller installed at the proposed NSD goes through large displacements, it generates nonlinear forces due to the nonlinear nature of the template slope function at higher

displacement values. Nevertheless, the combination of the Maxwell element in parallel with the proposed NSD has an acceptable match with that of CFB model when comparing time history responses of the SDOF structures even for the Northridge ground motion.

It is worthwhile to mention that the proposed NSD has to be designed based on the maximum allowable drift of the isolators for each base-isolated structure. The generated force by the NSD can be adjusted to produce linear negative stiffness for that range by adjusting the pre-compression length of the spring, stiffness of the spring and the shape of the curved template surface.

Chapter 11: Conclusions and Future Studies

This dissertation demonstrates the benefit of RILD in low frequency dynamic systems such as base-isolated structures, inter-story isolated buildings, and vehicle suspension system. The benefits are achieved through causal approximations, overcoming the non-causality of RILD.

This study presents a causal model to mimic RILD for the protection of low-frequency structures. In this model, an all-pass filter is designed with constant magnitude and a $\pi/2$ radians phase advance at a prescribed frequency, selected for most applications as the fundamental natural frequency of the dynamic system. The device-level response displacement of the structure is passed through the filter to determine the preceded displacement, approximating the Hilbert transform. Therefore, the only measurement needed is the displacement of the device. For example, in hybrid isolation, the displacement at the isolation level can be used to determine the desired force to be tracked by a semi-active (or active) device. The causal force is calculated using either an analog or digital all-pass filter. This simplicity and need for only local sensors is a great benefit for practical implementation. The followings present main conclusions of this research study as categorized by the subject.

11.1 Base-isolated Structures

Numerical analyses and experimental tests were conducted to demonstrate the performance and robustness of the proposed CFB method across a broad range of

input ground motions. Experimental tests used an MR damper in the isolation layer of a base-isolation system, all evaluated through shake table testing.

The desired causal RILD force was computed at each time step and a feed-forward control algorithm was used to track the desired force with the MR damper. For comparison, the response of the structure with an ideal RILD device in place of the MR damper was calculated in the frequency domain. Experimental results were shown to accurately reproduce noncausal analysis, achieving nominal RILD behavior for multiple input ground motions. The proposed CFB controller can also readily be applied in active control systems due to its robust design and smooth control force.

Overall, the proposed CFB controller is able to achieve damping with direct displacement control, a great benefit for limiting the displacement response of low-frequency structures through low control forces (and thus low accelerations) when compared than with traditional approaches (e.g., viscous and hysteretic damping). RILD can protect a low-frequency structure from low-frequency ground motion without compromising performance under high-frequency ground motions.

11.2 Inter-story Isolated Buildings

This dissertation also explored the benefits of incorporating RILD in inter-story isolated structures. As with a base-isolated structure, the device-level response displacement of the structure is passed through an all-pass filter to determine the preceded displacement, approximating the Hilbert transform at a specified frequency. Therefore, the only measurement needed is the displacement of the device.

An existing building (IFB) in Japan was modeled for the purpose of this study. The structure is divided into two substructures using dynamic substructuring for

evaluation in shake table RTHS. The substructure below the isolation layer was modeled numerically while the superstructure was tested experimentally. The base isolated specimen representing the superstructure has an MR damper in the isolation layer. The desired force was computed at each time step from the measured displacement and a semi-active control algorithm was used to track the desired force with the MR damper. For comparison, a state space frequency domain approach was presented to determine the noncausal response of the structure with ideal RILD in place of the MR damper.

Experimental results were shown to accurately reproduce the noncausal analysis, achieving RILD behavior for multiple input ground motions. The results show that the performance of the causal method is robust to multiple input ground motions because the substructure below the isolation layer filters the input ground motion. The isolation layer displacement response is therefore dominated by a narrow band of frequencies, useful for tuning the causal RILD approximation. Because of the narrow band response, the CFB model can greatly enhance the seismic performance of the inter-story isolation structure.

The CFB approach was compared to passive-on and passive-off controllers, all using the physical MR damper. Results show that the semi-active CFB controller produces same magnitude of displacement but with lower acceleration responses for the superstructure when compared to passive-on algorithm. In addition, results from RTHS tests using the semi-active CFB controller are compared to a numerically simulated prototype structure with discrete viscous damper installed in the isolation layer in place of the MR damper. The viscous damping coefficient is chosen so that

both of the systems have the same maximum 10th story drift. This comparison revealed that causal RILD incorporated into inter-story isolated structure can suppress the displacement response as much as ordinary viscous dampers but with lower damping force generated which also results in lower acceleration response of the superstructure.

Overall, the approach to achieve causal RILD is shown to greatly improve the seismic behavior of inter-story isolated structure by achieving damping with direct displacement control, a great benefit for limiting the displacement response through low control forces (and thus low accelerations) when compared to traditional approaches.

11.3 Vehicle Suspension System

The concept of RILD is then extended to vehicle suspension systems. As with base-isolated and inter-story-isolated structures, vehicles are subject to excitation frequencies higher than their own fundamental natural frequency. The previously proposed CFB approach was modified for application in vehicle suspension systems. A modal causal filter-based (MCFB) model is proposed, where modal coordinates of the quarter car model are computed at each time step. The modal coordinates are passed through corresponding all pass-filters which are tuned for the first and second modal frequencies of the system. The summation of the two modal forces results in the desired causal force which then can be tracked by any semi-active devices such as MR damper.

Numerical simulations were conducted to investigate the robustness of the MCFB algorithm across a wide range of inputs and vehicle speeds. The advantages of

the MCFB algorithm over the CFB algorithm are clearly shown. The effectiveness in mimicking the RILD response is illustrated through numerical simulations.

Finally, vibration performance of the MCFB algorithm is compared to that of skyhook and groundhook control policies. It is concluded that unlike skyhook and groundhook controllers that can mitigate sprung or unsprung mass responses at the expense of other mass results, proposed MCFB algorithm is able to attenuate both sprung and unsprung mass responses simultaneously and nearly as effective as skyhook and groundhook controllers at the same time. It is further shown that MCFB controller works well at both low and high velocities of the vehicle and is robust to changes in the occupancy or payload of the vehicle. Moreover, to implement proposed MCFB algorithm only sprung mass absolute acceleration is needed which can be measured using an accelerometer. Using that measurement, a Kalman filter can then estimate all the necessary states. This simplicity is a great benefit for practical implementations.

Overall the proposed controller is able to enhance the vibrational performance of the vehicle with direct control over displacement. This feature is a great benefit for dynamic systems such as vehicles that are subject to higher frequency vibrations than their own natural frequency.

11.4 Adaptive Causal RILD

To improve the performance of causal approximations of RILD, two adaptive algorithms are proposed to estimate the dominant structural response frequency and thereby accurately apply the displacement phase advance. This adaptation is added to a CFB controller to adaptively approximate ideal RILD.

In the proposed Adaptive V-D controller, the dominant frequency of vibration is calculated by dividing the moving RMS of the relative velocity by the moving RMS of the relative displacement. In the proposed Adaptive A-D controller, the dominant frequency of vibration is calculated using the slope of a linear-least square fit of the relative acceleration versus relative displacement represented in Cartesian coordinates. Two factors impact the performance of these adaptive controllers: the sampling rate and sampling range. The sampling rate should be chosen small enough so that it is not computationally burdensome while large enough to maintain an accurate estimation of the response frequency. By selecting the sampling range as the fundamental period of the structure allows approximately one cycle of response to enter into the calculations, avoiding bias but allowing for sufficiently fast adaptation.

To evaluate the performance of the adaptive algorithm, RTHS is conducted on a 5-story base-isolated building and a 14-story inter-story isolated building. Supplemental isolation-layer semi-active damping is used to track the desired causal RILD force. Experimental results show clear improvement of adaptive algorithm over the fixed-frequency CFB model in mimicking ideal RILD behavior. The hysteresis better matches the ideal noncausal model and displacement and acceleration responses are suppressed more effectively. The accuracy of the estimated response frequencies is confirmed by continuous wavelet transform analysis. In addition, the performances of the adaptive algorithm are compared to passive-on and passive-off semi-active controllers. Both adaptive methods can suppress displacement as effectively as the passive-on controller while keeping acceleration responses lower than the passive-on controller.

Overall, both Adaptive V-D and Adaptive A-D controllers are able to improve seismic performance of low-frequency structures by accurately implementing causal RILD over a broad range of response frequencies when compared to alternative causal methods. The selection of one adaptive method versus the other depends largely on available sensor measurements.

11.5 Passive Realization of RILD

Recognizing the popularity of passive devices in practical civil engineering applications, a passive model may be key to broader implementation of RILD. Passive control does not rely on external power, requires less maintenance in general, and is more readily accepted by the design industry.

It is shown in this dissertation that by increasing the Maxwell element loss factor and decreasing the structural stiffness, the CFB model can be achieved through a passive mechanical system. However, decreasing structural stiffness is not a viable alternative for existing structural systems. Additionally, decreasing stiffness through conventional means (e.g., the structural members), may result in failure under strength limits. Therefore, the combination of a Maxwell element and an ideal negative stiffness is shown to be able to physically match the CFB model, providing a passive alternative for RILD.

Furthermore, a linear negative stiffness device is developed to achieve passive RILD behavior in practical applications. As one possibility to create such a device a template is designed such that the slope change of the template is nearly linear for the maximum allowable drift of the isolators. The desired magnitude of linear negative stiffness then can be obtained by adjusting the stiffness of the pre-compressed spring.

For the SDOF base-isolated structure of this study, the designed template was a curved cosine function with no gap starting at maximum level at the origin and decrease to a level where both the template slope and induced NSD force remain linear.

Numerical analysis was conducted on SDOF base-isolated structures with various applied ground motions. Numerical responses of structures incorporated with noncausal RILD, CFB model, and combination of Maxwell element in parallel with the proposed NSD design are compared. It is shown that the proposed passive devices can closely track CFB algorithm for almost all of the input ground motions and that the proposed NSD can generate almost linear negative stiffness for the designed allowable maximum displacement of the isolators. The generated force by the NSD can be adjusted to produce linear negative stiffness for that range by adjusting the pre-compression length of the spring, stiffness of the spring, and the shape of the curved template surface.

11.6 Future Studies

This dissertation investigates incorporating RILD as an effective vibration mitigation damping strategy for low-frequency dynamic systems. The study proposes causal models appropriate for semi-active control and passive mechanical systems for fully passive control. Numerical simulations, shake table tests, RTHS, and shake table RTHS are conducted to demonstrate the performance of the proposed causal approaches for different dynamic systems. The results compare well to non-causal simulations in both the achieved forces and system responses. RILD is demonstrated

to be an attractive alternative for vibration mitigation of low-frequency structures. The followings represent some exciting future study avenues:

11.6.1 Inerter-based Passive Devices

This dissertation proposed a parallel passive combination of Maxwell element and negative stiffness device to realize RILD specifically for base-isolated structures. As an alternative to the proposed passive system, inerter-based passive devices can be used to mimic RILD behavior. Inerter is a passive device where its generated force is proportional to the relative acceleration of its terminals. A smart combination of inerter, springs, and passive viscous damper is shown to have promising seismic performance trying to approximate ideal RILD for low frequency dynamic system. Further research in this area can lead to a more practical passive system to incorporate RILD.

11.6.2 Nonlinear Analysis of Structures Incorporated with RILD

This dissertation explores the incorporation of RILD in vibration control engineering. The structures studies herein are linear, meaning that the control system is expected to maintain nominally linear performance of the structure. Future studies will focus on nonlinear analysis of the low-frequency dynamic systems equipped with RILD. More specifically, the proposed adaptive semi-active controllers seem to be a promising damping algorithm for nonlinear analysis due to their adaptability to response frequency of the structure. If a structure become damaged under extreme vibrations, as is allowed under performance-based design in earthquake engineering, adaptive damping strategies may be beneficial.

11.6.3 Adaptive RILD for Vehicle Suspension System

This dissertation clearly shows the advantages of incorporating the MCFB controller in vibration mitigation of vehicles suspension system. Future study in this subject will further focus on using the proposed adaptive controllers in vehicle suspension system. The controller can be adapted for different speeds or performance goals. For instance, adaptive controller can be designed/adapted for off road high speed, or stop and go (high traffic) driving.

11.6.4 Application of RILD in Outrigger System of Tall Buildings

Tall buildings are also low frequency dynamic systems which can benefit from RILD. The inter-story displacement is small, therefore RILD would not be effective in a traditional braced lateral system. To maximize the effectiveness of RILD, a damped outrigger system may work to amplify the device-level displacement while targeting the first vibrational mode. One possible future research avenue is to incorporate passive or semi-active RILD in outrigger system to protect the structure against earthquake or wind loading.

References

[1] K. Ikago, N. Inoue, Behavior of rate-independent linear damping incorporated into long-period structures subjected to strong ground motions, in: Proceedings of the 6th World Conference on Structural Control and Monitoring, 2014.

[2] R.E.D. Bishop, The Treatment of Damping Forces in Vibration Theory, The Journal of the Royal Aeronautical Society, 59 (1955) 738-742.

[3] P. Lancaster, Free Vibration and Hysteretic Damping, The Journal of the Royal Aeronautical Society, 64 (1960) 229-229.

[4] T.J. Reid, Free Vibration and Hysteretic Damping, The Journal of the Royal Aeronautical Society, 60 (1956) 283-283.

[5] T. Caughey, A. Vijayaraghavan, Free and forced oscillations of a dynamic system with "linear hysteretic damping"(non-linear theory), International Journal of Non-Linear Mechanics, 5 (1970) 533-555.

[6] M.A. Biot, Linear thermodynamics and the mechanics of solids, in, Cornell Aeronautical Lab., Inc., Buffalo, 1958.

[7] S.H. Crandall, Dynamic response of systems with structural damping, Air space and instruments, McGraw-Hill, New York, 1963.

[8] S. Crandall, The hysteretic damping model in vibration theory, Proceedings of the Institution of Mechanical Engineers, Part C: Mechanical Engineering Science, 205 (1991) 23-28.

[9] N. Makris, Causal Hysteretic Element, Journal of Engineering Mechanics, 123 (1997) 1209-1214.

[10] M. Crosby, D.C. Karnopp, The active damper—a new concept for shock and vibration control, Shock and Vibration Bulletin, 43 (1973) 119-133.

[11] D. Karnopp, M.J. Crosby, R. Harwood, Vibration control using semi-active force generators, Journal of engineering for industry, 96 (1974) 619-626.

[12] S. Dyke, B. Spencer Jr, M. Sain, J. Carlson, An experimental study of MR dampers for seismic protection, Smart materials and structures, 7 (1998) 693.

[13] S. Nagarajaiah, S. Xiaohong, Response of Base-Isolated USC Hospital Building in Northridge Earthquake, Journal of Structural Engineering, 126 (2000) 1177-1186.

[14] T. Fujita, Seismic isolation of civil buildings in Japan, Progress in Structural Engineering and Materials, 1 (1998) 295-300.

[15] J.M. Kelly, The role of damping in seismic isolation, Earthquake engineering & structural dynamics, 28 (1999) 3-20.

[16] C. Alhan, H. Gavin, A parametric study of linear and non-linear passively damped seismic isolation systems for buildings, Engineering structures, 26 (2004) 485-497.

[17] S. Nagarajaiah, S. Sahasrabudhe, Seismic response control of smart sliding isolated buildings using variable stiffness systems: an experimental and numerical study, Earthquake engineering & structural dynamics, 35 (2006) 177-197.

[18] H. Yoshioka, J. Ramallo, B. Spencer Jr, "Smart" base isolation strategies employing magnetorheological dampers, Journal of engineering mechanics, 128 (2002) 540-551.

[19] O.E. Ozbulut, M. Bitaraf, S. Hurlebaus, Adaptive control of base-isolated structures against near-field earthquakes using variable friction dampers, Engineering Structures, 33 (2011) 3143-3154.

[20] M. Hu, H. Si;, K. Li, J. Zhou, J. Huang, M. Uchida, EARTHQUAKE RESPONSE ANALYSIS OF A MID-STORY SEISMIC ISOLATED BUILDING, in: 13th World Conference on Earthquake Engineering, Vancouver, B.C., Canada, 2004.

[21] K. Ogura, M. Takayama, O. Tsujita, Y. Kimura, A. Wada, SEISMIC RESPONSE OF MID-STORY ISOLATED BULIDINGS, Journal of Structural and Construction Engineering (Transactions of AIJ), 64 (1999) 99-104.

[22] X. Huang, F. Zhou, S. Wang, X. Luo, Theoretical and experimental investigation on mid-story seismic isolation structures, in: The 14th World Conference on Earthquake Engineering, 2008.

[23] K. Murakami, H. Kitamura, H. Ozaki, T. Teramoto, Design and analysis of a building with the middle-story isolation structural system, 2000.

[24] T. Sueoka, S. Torii, Y. Tsuneki, The application of response control design using middle-story isolation system to high-rise building, in: 13th World Conference on Earthquake Engineering, 2004.

[25] S. Kawamura, R. Sugisaki, K. Ogura, S. Maezawa, S. Tanaka, A. Yajima, Seismic isolation retrofit in Japan, in: 12th World Conference on Earthquake Engineering, 2000.

[26] F.L. Zhou, Seismic isolation of civil buildings in the People's Republic of China, Progress in Structural Engineering and Materials, 3 (2001) 268-276.

[27] K. Murakami, H. Kitamura, Y. Matsushima, The prediction for seismic responses of the two-mass model with the mid-story isolation system, Journal of Structural and Construction Engineering, (2001) 51-58.

[28] S.J. Wang, K.C. Chang, J.S. Hwang, B.H. Lee, Simplified analysis of mid-story seismically isolated buildings, Earthquake Engineering & Structural Dynamics, 40 (2011) 119-133.

[29] L.X.-z.O. Hai-long, L. Shu, simplified analysis on calculation model of interlayer seismic isolation, Earthquake Engineering and Engineering Vibration, 1 (2002) 021.

[30] M.-H. Chey, J.G. Chase, J.B. Mander, A.J. Carr, Semi-active control of mid-story isolation building system, 2009.

[31] G. Yan, F. Chen, Seismic performance of midstory isolated structures under near-field pulse-like ground motion and limiting deformation of isolation layers, Shock and Vibration, 2015 (2015).

[32] C.H. Loh, J.H. Weng, C.H. Chen, K.C. Lu, System identification of mid-story isolation building using both ambient and earthquake response data, Structural Control and Health Monitoring, 20 (2013) 139-155.

[33] S. Choi, H. Lee, E. Chang, Field test results of a semi-active ER suspension system associated with skyhook controller, Mechatronics, 11 (2001) 345-353.

[34] G. Yao, F. Yap, G. Chen, W. Li, S. Yeo, MR damper and its application for semi-active control of vehicle suspension system, Mechatronics, 12 (2002) 963-973.

[35] D.E. Ivers, L.R. Miller, Semi-active suspension technology. An evolutionary view, ASME, NEW YORK, NY,(USA). 40 (1991) 327-346.

[36] Y. Shen, M. Golnaraghi, G. Heppler, Semi-active vibration control schemes for suspension systems using magnetorheological dampers, Journal of Vibration and Control, 12 (2006) 3-24.

[37] A.M. Khiavi, M. Mirzaei, S. Hajimohammadi, A new optimal control law for the semi-active suspension system considering the nonlinear magneto-rheological damper model, Journal of Vibration and Control, 20 (2014) 2221-2233.

[38] M. Ahmadian, C.A. Pare, A quarter-car experimental analysis of alternative semiactive control methods, Journal of Intelligent Material Systems and Structures, 11 (2000) 604-612.

[39] J.A. Inaudi, J.M. Kelly, Linear hysteretic damping and the Hilbert transform, Journal of Engineering Mechanics, 121 (1995) 626-632.

[40] J.A. Inaudi, N. Makris, Time-domain analysis of linear hysteretic damping, Earthquake Engineering and Structural Dynamics, 25 (1996) 529-546.

[41] P.D. Spanos, S. Tsavachidis, Deterministic and stochastic analyses of a nonlinear system with a Biot visco-elastic element, Earthquake engineering & structural dynamics, 30 (2001) 595-612.

[42] G. Muscolino, A. Palmeri, F. Ricciardelli, Time-domain response of linear hysteretic systems to deterministic and random excitations, Earthquake engineering & structural dynamics, 34 (2005) 1129-1147.

[43] A.D. Nashif, D.I. Jones, J.P. Henderson, Vibration damping, John Wiley & Sons, 1985.

[44] J.E. Carrion, Model-based strategies for real-time hybrid testing, University of Illinois at Urbana-Champaign, 2007.

[45] R. Christenson, Y.Z. Lin, A. Emmons, B. Bass, Large-scale experimental verification of semiactive control through real-time hybrid simulation 1, Journal of Structural Engineering, 134 (2008) 522-534.

[46] M. Zapateiro, H. Karimi, N. Luo, B. Spencer, Real-time hybrid testing of semiactive control strategies for vibration reduction in a structure with MR damper, Structural Control and Health Monitoring, 17 (2010) 427-451.

[47] P.B. Shing, Real-time hybrid testing techniques, in: Modern testing techniques for structural systems, Springer, 2008, pp. 259-292.

[48] R. Zhang, B.M. Phillips, S. Taniguchi, M. Ikenaga, K. Ikago, Shake table real-time hybrid simulation techniques for the performance evaluation of buildings with inter-story isolation, Structural Control and Health Monitoring, (2016).

[49] Y. Ohtori, R. Christenson, B. Spencer Jr, S. Dyke, Benchmark control problems for seismically excited nonlinear buildings, Journal of Engineering Mechanics, 130 (2004) 366-385.

[50] ISO8608, Mechanical vibration, road surface profiles. Reporting of Measured Data, 1995.

[51] M. Agostinacchio, D. Ciampa, S. Olita, The vibrations induced by surface irregularities in road pavements–a Matlab® approach, European Transport Research Review, 6 (2014) 267-275.

[52] J.A. Inaudi, MODULATED HOMOGENEOUS FRICTION: A SEMI-ACTIVE DAMPING STRATEGY, Earthquake engineering & structural dynamics, 26 (1997) 361-376.

[53] A. Keivan, B.M. Phillips, M. Ikenaga, K. Ikago, Causal Realization of Rate-Independent Linear Damping for the Protection of Low-Frequency Structures, Journal of Engineering Mechanics, (2017) 04017058.

[54] N. Makris, Rigidity-plasticity-viscosity: can electrorheological dampers protect base-isolated structures from near-source ground motions?, Earthquake Engineering and Structural Dynamics, 26 (1997) 571-592.

[55] N. Makris, S.-P. Chang, Effect of viscous, viscoplastic and friction damping on the response of seismic isolated structures, Earthquake Engineering & Structural Dynamics, 29 (2000) 85-107.

[56] J.D. Carlson, M.R. Jolly, MR fluid, foam and elastomer devices, mechatronics, 10 (2000) 555-569.

[57] G. Koch, T. Kloiber, B. Lohmann, Nonlinear and filter based estimation for vehicle suspension control, in: Decision and Control (CDC), 2010 49th IEEE Conference on, IEEE, 2010, pp. 5592-5597.

[58] O. Lindgärde, Kalman filtering in semi-active suspension control, IFAC Proceedings Volumes, 35 (2002) 439-444.

[59] A. Keivan, B.M. Phillips, Rate-independent linear damping in vehicle suspension systems, Journal of Sound and Vibration, 431 (2018) 405-421.

[60] M.-S. Seong, S.-B. Choi, K.-G. Sung, " Control Strategies for Vehicle Suspension System Featuring Magneto Rheological (MR) Damper, Vibration Analysis and Control, New trend and Developments, Dr. Francisco Beltran-carbajal (Ed.) ISBN, (2011) 978-953.

[61] A. Keivan, B.M. Phillips, K. Ikago, Adaptive causal realization of rate-independent linear damping, Engineering Structures, 167 (2018) 256-271.

[62] A. Friedman, S. Dyke, B. Phillips, Over-driven control for large-scale MR dampers, Smart Materials and Structures, 22 (2013) 045001.

[63] B. Phillips, Z. Jiang, J.M. Ricles, S.J. Dyke, Y. Chae, B. Spencer, R.E. Christenson, A. Agrawal, Real-time hybrid simulation benchmark study with a large-scale MR damper, Proc. of the 5th WCSCM, (2010) 12-14.

[64] F. Weber, Robust force tracking control scheme for MR dampers, Structural Control and Health Monitoring, 22 (2015) 1373-1395.

[65] A.A. Sarlis, D.T.R. Pasala, M. Constantinou, A. Reinhorn, S. Nagarajaiah, D. Taylor, Negative stiffness device for seismic protection of structures, Journal of Structural Engineering, 139 (2012) 1124-1133.

[66] T. Sun, Z. Lai, S. Nagarajaiah, H.N. Li, Negative stiffness device for seismic protection of smart base isolated benchmark building, Structural Control and Health Monitoring, 24 (2017).